PRODUCTION OF COLD BARIUM MONOHALIDE IONS

A Thesis
Presented to
The Academic Faculty

by

Michael V. DePalatis

In Partial Fulfillment
of the Requirements for the Degree
Doctor of Philosophy in the
School of Physics

Georgia Institute of Technology
December 2013

For great justice.

ACKNOWLEDGEMENTS

Science is never done in a vacuum. Well, actually, it is quite often done in a literal vacuum. But doing good science requires more than just the hard work of one individual. To reach the point where one can design, build, and implement an experiment involves years of training, education, and practice which requires the input of many others. For that, I am grateful for the contributions of a great many people, some of whom may even read this!

First and foremost, I must thank my advisor, Professor Mike Chapman. When I was considering which grad schools to apply to, Mike's group was the one at Georgia Tech that particularly piqued my interest. When I arrived on campus, Mike was happy to add me to an already large group. During my time here, he has always provided me with great advice on running experiments, how to interpret and process data, and how best to present results to others. Mike is always very encouraging and has done much to enable a very friendly atmosphere in the lab. During many group lunches, when discussing such disparate topics as college football and current events, Mike would often find an interesting Fermi problem which the group would then work to find a solution to. This was often a fun diversion, and a good hallmark of a talented physicist.

I am also very much indebted to Professor Alex Kuzmich. At the onset of the thorium project, Alex was kind (and I daresay patient) enough to add me to the team working to trap and laser cool Th^{3+} in his lab before I even had much hands-on experience in experimental atomic physics. Alex's work ethic and physical insight has a tendency to carry over to the others working in his lab, and I was able to learn a great deal quickly in this environment. It was also in Alex's lab that I was fortunate enough to work with Corey Campbell. Corey is an incredible scientist, both in his experimental prowess and in his ability to work through theoretical problems that might make a lesser experimentalist mumble something about

not being a theorist. I learned everything from basic optics techniques to more subtle skills required to run a good experiment from Corey. Along the way, we had plenty of interesting conversations completely unrelated to physics. Alex, Corey, and I were also fortunate to work alongside the very talented undergraduate Dave Naylor. Nearly every Friday, Corey, Dave, and I were also joined by the other members of the Kuzmich lab, Ran Zhao, Alex Radnaev, and Yaroslav Dudin for "B and B."

Meanwhile, back in the Chapman lab, the two comrades I am most indebted to are Adam Steele and Layne Churchill. Adam was the senior ion trapper of the group and helped lay much of the ground work for the experiments to come. Without his tireless efforts, it's hard to imagine what the lab might have been like upon my arrival. Along with Corey, I learned a great deal while working with Layne. Layne's attention to detail is nothing short of amazing, and this trait was crucial for much of our experimental efforts. Layne was always a fun person to work with given his sarcastic wit and deadpan delivery of song lyrics before the singer had a chance to sing them more melodiously. Near the end of my time in the lab, I also got a lot of support from Brian Rose, a nuclear engineering undergraduate who could always break a twenty. Ben Land was another extremely talented undergrad whose knowledge of computers and programming seemingly knows no bound.

Although I didn't work directly with most of the other members of the Chapman group, each one of them has contributed to my growth as a scientist. Having entered grad school at the same time, Chung-Yu Shih and I spent many a long night working on homework problems during our first year. Later he was always willing to help me think about any problem I might be having trying to interpret results of my experiments. Early on, I received excellent advice and instruction from two postdocs, Paul Griffin and Peyman Ahmadi. Chris Hamley is by now something of a fixture in the Chapman lab. It's really rather difficult to imagine a time when he wasn't around in some capacity. It's become somewhat of a lab trope to acknowledge Chris as having an answer to every question, even the one you didn't ask. Chris is truly a great asset to the lab, and I have enjoyed the many conversations we

have had about physics and other topics. Michael Gibbons, perhaps better known as Mikey G, would often join in on these discussions. Apart from Mike, for a long time, the only other person in the lab I could talk about college football with was Soo Kim. Soo is wise beyond her years and often gave great advice on nearly any topic. Eva Bookjans always brought a European perspective to the lab and I greatly enjoyed our conversations and playing soccer with her. If hard workers had a labor union, Thai Hoang would undoubtedly be their leader. There was hardly ever a time I would come into the lab to *not* find that Thai had already been there for hours. Thai is also one of the most enthusiastic people I have ever met. Whenever I'd wander into the main lab looking for something, he'd immediately drop whatever he was doing and start looking. This is in direct contrast with Corey Gerving, who was usually the person responsible for our needing to search for things in the first place. Maybe it wasn't really his fault, but Corey did help establish the rule that you can only blame people who aren't present, and for that, he is a great American. Martin Anquez cannot claim this title, but he has been a good addition to the lab. Martin excels at running BEC experiments, annoying Chris, and mispronouncing "epitome." Bryce Robbins and Xiaoyun Yang are relatively recent recruits, and so I lack amusing anecdotes, but each has helped me out from time to time. I expect both of them to contribute a great deal to the group in the coming years.

Finally, I acknowledge my parents, Lou and Rita. Without their support and encouragement, I would not be the person I am today.

Contents

DEDICATION . . . . . **ii**

ACKNOWLEDGEMENTS . . . . . **iii**

LIST OF TABLES . . . . . **ix**

LIST OF FIGURES . . . . . **x**

LIST OF SYMBOLS OR ABBREVIATIONS . . . . . **xiii**

LIST OF LISTINGS . . . . . **xiv**

SUMMARY . . . . . **xv**

I INTRODUCTION **1**

1.1 Thorium ion trapping 1

1.2 Cold molecular ions 7

1.3 Organization of thesis 9

II ION TRAPPING **10**

2.1 Dynamics of trapped ions 10

2.1.1 Formulation 10

2.1.2 Stability of solutions 12

2.1.3 The pseudopotential approximation 18

2.2 Ion interactions with light 22

2.2.1 Three level atoms 22

2.2.2 Doppler cooling 27

2.3 Coulomb crystals and sympathetic cooling 33

2.3.1 Coulomb crystals 33

2.3.2 Sympathetic cooling 34

2.4 Summary 36

III MOLECULAR DYNAMICS SIMULATIONS **37**

3.1 Theoretical overview 38

3.1.1 Trapping potential . . . 38
3.1.2 Laser force . . . 38
3.1.3 Coulomb interaction . . . 41
3.1.4 Heating effects . . . 41
3.2 Implementation . . . 42
3.2.1 Leapfrog integration . . . 43
3.2.2 Initial conditions . . . 44
3.3 Results . . . 46
3.4 Summary and future work . . . 50

IV EXPERIMENTAL SETUP . . . 51

4.1 Lifetime trap . . . 51
4.2 Optical setup . . . 61
4.2.1 Laser setup . . . 61
4.2.2 Locking cavities . . . 61
4.2.3 Thorium locking cavity . . . 63
4.2.4 Barium locking cavities . . . 65

V TH IV LIFETIME MEASUREMENTS . . . 70

5.1 $6^2D_{5/2}$ lifetime measurement . . . 71
5.2 Discussion . . . 76
5.3 Conclusion . . . 82

VI CHEMICAL REACTIONS WITH TRAPPED BARIUM IONS . . . 83

6.1 Introduction . . . 83
6.2 Classical rate models . . . 84
6.3 Product mass determination . . . 86
6.3.1 Nondestructive mass determination . . . 87
6.3.2 Coulomb crystal mass spectrometry . . . 92
6.4 Reaction rate measurements . . . 95
6.4.1 Reactions with sulfur hexafluoride . . . 99

6.4.2 Reactions with methyl chloride . . . 102
6.4.3 Reactions with bromine and iodine . . . 103
6.5 Conclusion . . . 108

VII CONCLUSION AND FUTURE DIRECTIONS . . . 110
7.1 Future directions . . . 111
7.1.1 Thorium . . . 111
7.1.2 Molecular ions . . . 113

Appendix A — REACTION ENTHALPIES . . . 115
Appendix B — PROGRAM LISTINGS . . . 117
Appendix C — DATA TABLES . . . 124
Appendix D — STANFORD SR560 REPLACEMENT CIRCUIT . . . 127
Appendix E — BARIUM LASERS . . . 130
Appendix F — APD QUANTUM EFFICIENCY . . . 137
REFERENCES . . . 139
VITA . . . 156

List of Tables

2.1 Polynomial fit coefficients for approximating the first stability region 17
4.1 Component listing for the micromotion compensation circuit 60
4.2 Calculated cavity parameters 64
5.1 Th^{3+} lifetime measurement experimental conditions 77
5.2 Summary of theoretical and measured Th^{3+} lifetimes 77
6.1 Reaction rate constants between Ba^{+} and neutral reactants 109
A.1 Estimated reaction enthalpies 116
C.1 Naturally occurring isotopes of barium and their properties 124
C.2 Isotope shifts of $^{13x}Ba^{+}$ relative to $^{138}Ba^{+}$ 125
C.3 Thorium isotope data 125
C.4 Approximate mass to charge ratios 125
C.5 Dissociation energies 126
C.6 Ionization energies 126
D.1 Part list for the preamp circuit 129

List of Figures

1.1 Ion periodic table of the elements . . . 2
1.2 ^{229}Th nuclear excitation scheme . . . 6
2.1 RF electrode configuration . . . 11
2.2 Quadrupole potential . . . 13
2.3 Numerically computed solutions to the Mathieu equation . . . 13
2.4 Isolines of the stability parameter β . . . 15
2.5 Regions of stability for x and y equations of motion . . . 16
2.6 First stability region . . . 17
2.7 Mass resolution example . . . 18
2.8 Ion trajectories computed by SIMION . . . 21
2.9 Various three level systems . . . 23
2.10 Numerical integration of the three level system near saturation . . . 27
2.11 Three level system for rate equation model . . . 28
2.12 Comparison of three level system models . . . 28
2.13 Simple ion cooling model . . . 30
2.14 Temperature measurement . . . 32
2.15 Comparison of ions in the crystal and cloud phases . . . 33
2.16 Coulomb crystals . . . 35
3.1 Experimental and simulated isotope sorting of Ba^+ ions . . . 39
3.2 Simulated ion trajectories . . . 47
3.3 3-D rendering of a simulated ion crystal . . . 47
3.4 Simulated and experimental Ba^+ ion chains . . . 47
3.5 Simulated CCD images of increasing numbers of Ba^+ ions . . . 48
3.6 Simulated CCD images of Ba^+ and molecular ions . . . 49
3.7 Simulated sympathetic cooling of thorium ions . . . 49
4.1 Overview of the experimental setup . . . 52

4.2 Sketches of the machined end caps . . . 53
4.3 Photographs of the lifetime trap. . . . 54
4.4 Axial potential of Mickey Mouse end caps . . . 55
4.5 Image of a large thermal cloud of Th^{3+} . . . 57
4.6 Comparison of lifetime trap stability regions for several ions . . . 57
4.7 Ba^{+} ions loaded and cooled without buffer gas . . . 58
4.8 Measured loss rate of Th^{3+} in buffer gas . . . 59
4.9 Micromotion compensation circuit schematic . . . 60
4.10 Simplified level structure diagrams of Ba^{+} and Th^{3+} . . . 62
4.11 Thorium laser locking cavity layout . . . 66
4.12 Cavity locking signals . . . 66
4.13 Barium laser stabilization scheme . . . 68
4.14 Cavity transmission signals of 780 nm and 986 nm light . . . 69
5.1 Simulated measurement of the $6^2D_{5/2}$ state lifetime measurement . . . 72
5.2 Photodiode signal of the 984 nm laser shuttering . . . 74
5.3 Timing diagram for measuring the $6^2D_{5/2}$ excited state lifetime . . . 74
5.4 Th^{3+} lifetime measurement experimental setup . . . 75
5.5 Typical $6^2D_{5/2}$ lifetime measurement . . . 76
5.6 Compilation of $6^2D_{5/2}$ lifetime measurements . . . 78
5.7 Measured $6^2D_{5/2}$ state lifetime versus helium pressure . . . 79
5.8 $6^2D_{5/2}$ state lifetime measurement as a function of RF voltage . . . 81
6.1 Comparison of AC frequency sweeps with and without molecular ions . . . 88
6.2 Comparison of simulated and measured axial secular frequencies . . . 89
6.3 AC frequency sweep of a Ba^{+} + BaO^{+} ion crystal . . . 91
6.4 AC frequency sweep comparison . . . 92
6.5 Coulomb crystal mass spectrometry of Ba^{+} + BaO^{+} ion crystals . . . 94
6.6 Large Coulomb crystal reacting with SF_6 . . . 97
6.7 Measurements of $^{138}Ba^{+}$ fluorescence versus detuning at different stages of a reaction . . . 98

6.8 Ba^+ loss rate measurement due to SF_6 100
6.9 Reaction rate constant measurement between Ba^+ and SF_6 101
6.10 Coulomb crystal mass spectrometry of Ba^+ + BaF^+ ion crystals 102
6.11 Ba^+ loss rate measurement between Ba^+ and CH_3Cl 104
6.12 Reaction rate constant measurement between Ba^+ and CH_3Cl 105
6.13 MD simulation of sympathetically cooled BaI^+ Coulomb crystals 106
6.14 Coulomb crystal mass spectrometry of Ba^+ + $BaBr^+$ ion crystals 108
C.1 Ba^+ level structure and wavelengths 124
D.1 SRS SR560 replacement circuit schematic 128
E.1 Cold laser housing layout 132
E.2 SHG 100 doubling cavity 133

LIST OF SYMBOLS OR ABBREVIATIONS

ADO average dipole orientation.

AOM acousto-optic modulator.

APD avalanche photodiode.

BEC back end cap.

CCMS Coulomb crystal mass spectrometry.

CEM channel electron multiplier.

CF Conflat flange.

EMCCD electron-multiplying charged coupled device.

EOM electro-optic modulator.

FEC front end cap.

FSR free spectral range.

MD molecular dynamics.

Nd:YAG neodymium-doped yttrium aluminum garnet; Nd:$Y_3Al_5O_{12}$.

PTFE polytetrafluoroethylene; technical name for the DuPont polymer branded as Teflon®.

PVDF polyvinylidene difluoride; a highly chemical resistant polymer.

QED quantum electrodynamics.

RF radio frequency.

SPCM single photon counting module.

TEC thermoelectric cooler.

TOFMS time of flight mass spectrometry.

VUV vacuum ultraviolet.

LIST OF LISTINGS

Stability determination 117
Stability boundary calculations 118
Three level system 119
Simple ion cooling model 121

SUMMARY

Ion traps are an incredibly versatile tool which have many applications throughout the physical sciences, including such diverse topics as mass spectrometry, precision frequency metrology, tests of fundamental physics, and quantum computing. In this thesis, experiments are presented which involve trapping and measuring properties of Th^{3+}. Th^{3+} ions are of unique interest in part because they are a promising platform for studying an unusually low-lying nuclear transition in the ^{229}Th nucleus which could eventually be used as an exceptional optical clock. Here, experiments to measure electronic lifetimes of Th^{3+} are described. A second experimental topic explores the production of sympathetically cooled molecular ions. The study of cold molecular ions has a number of applications, some of which include spectroscopy to aid the study of astrophysical objects, precision tests of quantum electrodynamics predictions, and the study of chemical reactions in the quantum regime. The experiments presented here involve the production of barium monohalide ions, BaX^+ (X = F, Cl, Br). This type of molecular ion proves to be particularly promising for cooling to the rovibrational ground state. The method used for producing BaX^+ ions involves reactions between cold, trapped Ba^+ ions and neutral gas phase reactants at room temperature. The Ba^+ ion reaction experiments presented in this thesis characterize these reactions for producing Coulomb crystals composed of laser cooled Ba^+ ions and sympathetically cooled BaX^+ ions.

Chapter I

INTRODUCTION

Of all the techniques of atomic, molecular, and optical physics developed in the decades following the advent of quantum theory, ion trapping has been among those with perhaps the most sustained success and level of innovation. Ion traps are capable of confining anything with a net charge from macroscopic objects [1, 2] to complex biomolecules [3, 4], single atoms [5, 6], and fundamental particles such as electrons and positrons [7]. Applications of ion traps include mass spectrometry [8], high-precision atomic clocks [9, 10], tests of fundamental physics [11, 12], quantum computing and simulation [13–16], and studies of chemical reactions both in the classical and quantum regimes [17–20]. A number of atomic ions have been used for many of these applications and are surveyed in Figure 1.1. Although any charged particle can be easily confined in three dimensions, those highlighted are of particular interest due to their relatively simple electronic level structures which are convenient for laser cooling and fluorescence detection. This thesis adds to the large body of existing work by studying properties of Th^{3+} ions and reactions involving Ba^{+} ions. The subsequent two sections of this chapter provide motivation for performing experiments with these two ions.

1.1 Thorium ion trapping

Thorium is a naturally occurring, radioactive element found in rather high abundance in the Earth's crust (it is estimated to be nearly as abundant as both lead and molybdenum and up to four times as common as uranium [24]). Thorium was once used in gas lantern mantles [25] in addition to ceramics and strong metal alloys, and even high quality photographic lenses [24]. Most of these uses have since been phased out over the past several decades due to concerns about the radioactivity of thorium, though thoriated tungsten filaments are

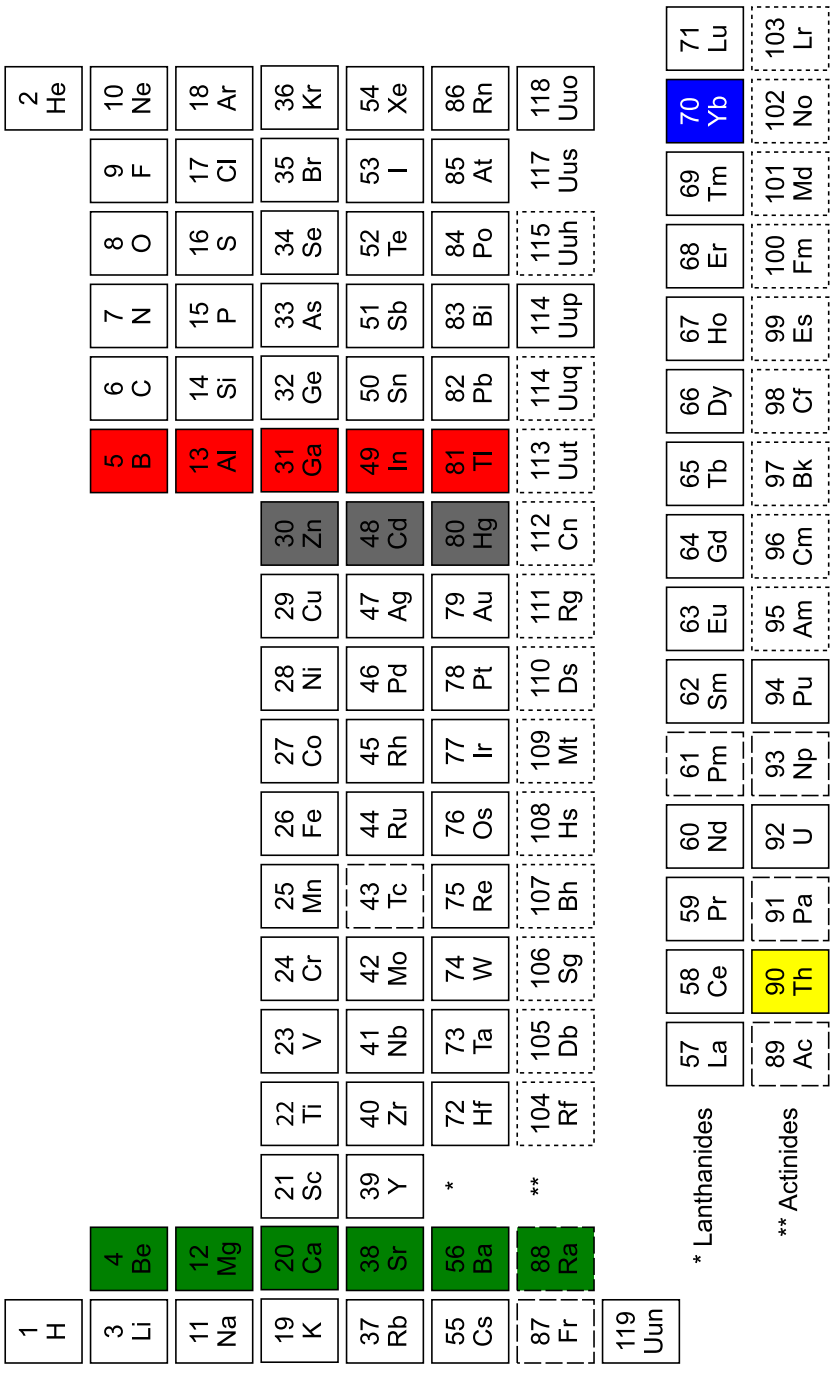

Figure 1.1: The periodic table of the elements with atomic ions used in various research efforts around the world. (Green) Alkaline earth metal ions are the most commonly used due to having a single valence electron and a convenient level structure. (Red) Two-electron ions. These are somewhat more challenging to work with but have some important applications [10, 21, 22]. (Blue) Despite a more complicated level structure, Yb^+ has proven useful for many experiments. (Gray) These ions have quantum information and frequency metrology applications. (Yellow) Th^{3+} is a good platform for studying low-lying nuclear transitions. This figure was adapted from Ref. [23].

still common as a source of electrons through thermionic emission [26]. More recently, there has been increased interest in the thorium fuel cycle as an alternative nuclear power source which may be more resistant to nuclear weapons proliferation than the uranium fuel cycle [27], although some debate on this possibility remains [28].

All this aside, primary interest from a fundamental physics perspective stems from the existence of a low-lying nuclear transition in the radioisotope ^{229}Th which is low enough in energy to be accessible to table-top, near-optical laser sources. Coupled with the inherent isolation of the nucleus from the environment due to electron shielding, the extraordinarily long several hour lifetime of this nuclear isomer state could make ^{229}Th a superb frequency standard that is orders of magnitude better than the current state of the art atomic clocks [29,30]. There is also speculation that the nuclear isomer transition could display enhanced sensitivity to temporal variations in the fine structure constant [31,32], though this is by no means certain [33–35].

Kroger and Reich [36] first concluded from observations of alpha decay of ^{233}U nuclei that the separation between the $I^{\pi} = 5/2^{+}$ ground state (commonly denoted ^{229g}Th) and $I^{\pi} = 3/2^{+}$ metastable isomer state (^{229m}Th) of the ^{229}Th nucleus must be less than 100 eV, considerably lower than the normal keV–MeV energies separating nuclear states. Subsequent experimental studies indirectly supported this idea and eventually an expected energy splitting of around 3.5 eV was reported [37, 38] which would fall comfortably in the optical regime. In part, this new estimate resulted in a number of unsuccessful attempts to observe the ^{229g}Th $\leftrightarrow$ ^{229m}Th transition [39]. Later, an improved experiment conducted by Beck *et al.* indirectly established by measuring gamma ray energies following the alpha decay of ^{233}U nuclei that the energy of the ^{229}Th nuclear isomer transition has a somewhat higher value of 7.6 ± 0.5 eV [40], helping to explain past observational failures. Recently, the deexcitation of the ^{229m}Th state may have been directly observed for the first time and its half-life established to be 6 ± 1 hours [41], though some questions remain about this measurement [42].

Several efforts presently exist in order to measure and excite the ^{229g}Th $\leftrightarrow$ ^{229m}Th transition. One approach involves trapped Th^+ ions [43, 44]. While Th^+ has a very dense electronic level structure, it is possible to quench some states with buffer gas, partially simplifying the laser requirements. Other proposals take a solid state approach with ^{229}Th nuclei embedded in a host crystal such as CaF_2 which is transparent to the UV light required to drive the ^{229g}Th $\leftrightarrow$ ^{229m}Th transition [45–48]. This approach has some advantages, such as signal enhancement thanks to being able to excite a large number of ^{229}Th nuclei simultaneously and the intriguing possibility of ultimately developing a solid state optical clock. The drawbacks include the need to account for frequency shifts due to embedding the ^{229}Th nuclei in a crystal rather than probing it in free space and requiring direct excitation of the nuclei with vacuum ultraviolet (VUV) light. As will be discussed below, this is as opposed to the Th^+ and Th^{3+} excitation schemes which can exploit the electron bridge process in order to use a much more accessible wavelength.

Peik and Tamm [29] first proposed the use of Th^{3+} in an ion trap as a platform to study the ^{229g}Th $\leftrightarrow$ ^{229m}Th transition since its single valence electron yields a convenient level structure for laser cooling. This in turn would allow for high resolution spectroscopy on an isolated $^{229}Th^{3+}$ ion. As a first step towards this goal, in a joint effort between the Chapman and Kuzmich labs at Georgia Tech, $^{232}Th^{3+}$ became the first multiply charged ion to be directly laser cooled [49]. To date, no other element has been directly laser cooled beyond its first charge state. This is not particularly surprising in part because higher charge states tend to have transition wavelengths well into the UV where coherent optical sources are lacking, making Th^{3+} exceptional since three of its low-lying transitions are in the visible or near infrared. Because of special challenges in producing and storing Th^{3+} ions, it took nearly two years after the initial laser cooling of $^{232}Th^{3+}$ to successfully trap and laser cool $^{229}Th^{3+}$ [50]. While theoretical progress has been steady [30], as yet the ^{229g}Th $\leftrightarrow$ ^{229m}Th transition has not been excited using Th^{3+} ions, nor in any other system.

There are two primary schemes for exciting the ^{229g}Th $\leftrightarrow$ ^{229m}Th using $^{229}Th^{3+}$. The

most straightforward method from a theoretical standpoint is to directly excite the ^{229}Th nucleus using a laser tuned to the $M1$ isomer transition. This is technically challenging, however, since the uncertainty in the transition energy corresponds to a wavelength of about 160 ± 11 nm. As this reported uncertainty only represents a single standard deviation, a full search could in practice need to cover a much wider range. On the low end, this wavelength range extends into the VUV regime, which makes laser setups extremely challenging. Furthermore, the large wavelength uncertainty coupled with the extremely narrow isomer transition results in an incredibly long required search time for finding the isomer transition.

A second, more promising scheme involves exploiting the coupling between electronic and nuclear states by what is known as the electron bridge [43, 51]. In this process, the ground and isomer nuclear manifolds are mixed through the hyperfine interaction which allows for electric dipole-allowed transitions between the ground and metastable nuclear states. The strongest such mixing is expected to occur for the S electronic states, the lowest of which are the $7^2S_{1/2}$ and $8^2S_{1/2}$ states. The resulting wavelengths required to cover the full range of possible electron bridge transition wavelengths are between 250 nm and 800 nm. Although this range is much larger than the uncertainty involved in exciting the nucleus directly, the wavelengths involved are much easier to achieve with high power, tabletop sources and therefore the electron bridge is a more promising scheme for excitation of the isomer. The general search protocol then involves first exciting the valence electron of a $^{229}Th^{3+}$ ion to a suitable level from which a high power source with a tunable range of 250–800 nm can then drive the electron bridge transition into the nuclear isomer state (see Figure 1.2). Although this wavelength range is large, it is wholly accessible with a Ti:sapphire laser along with second and third harmonic generation.

In addition to studies of the nuclear transition, trapped Th^{3+} ions are also worthwhile of study due to the unusual transitions from the ground electronic state. In most ions and neutral atoms used in atomic physics, the main cycling transition is an $S \leftrightarrow P$ transition.

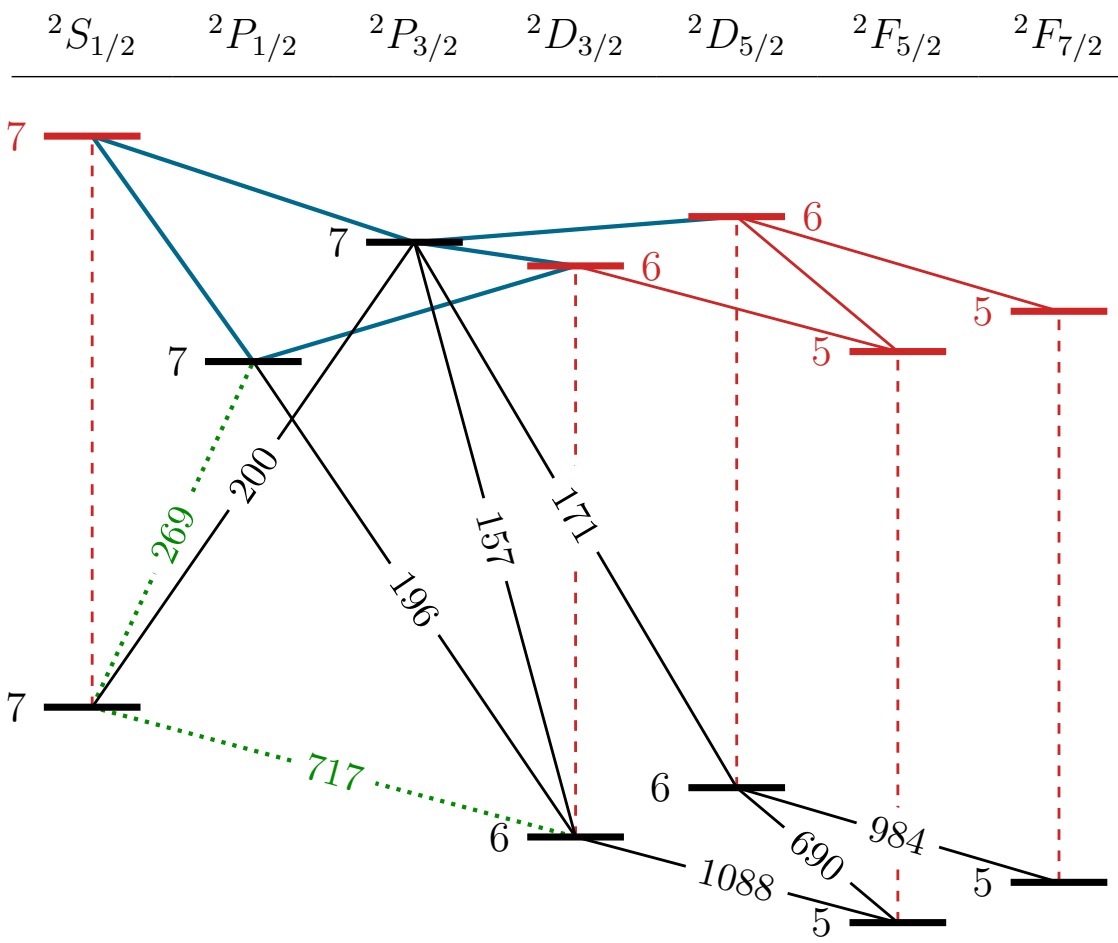

Figure 1.2: Partial Grotrian diagram of $^{229}Th^{3+}$ levels in both the ground nuclear state (black levels) and nuclear isomer state (red levels). Dashed red lines indicate direct nuclear excitation via $M1$ transitions. Dotted green lines indicate the electronic transitions needed to access the nuclear isomer via the electron bridge process (ideal cases shown as blue lines). Other electronic transitions in the nuclear ground state (black lines) and nuclear isomer state (red lines) are also shown with listed wavelengths in nm [49, 52]. This figure is adapted from Ref. [51].

Th^{3+}, in contrast, exhibits $F \leftrightarrow D$ transitions, unlike the otherwise isoelectronic Fr and Ra^+, each of which has a $7S$ ground state [53]. This complicates *ab initio* electronic structure calculations, and therefore experimental measurements are vital for testing and improving these computational techniques.

1.2 Cold molecular ions

Of the myriad of ions used in atomic physics experiments (Figure 1.1), the alkaline earth metal ions have perhaps the most storied history due to their single valence electron. Mg^+ and Ba^+ were independently the first trapped atomic systems to be laser cooled [54–56]. Shortly thereafter, a barium ion became the first single atom to be directly imaged [5, 6]. Soon, Be^+ [57], Sr^+ [58], and Ca^+ [59] were also laser cooled. More recently, short-lived isotopes of Ra^+ have been studied in the context of parity violation experiments [12,60,61], thus completing the alkaline earth metal column of the periodic table.

Each alkaline earth metal ion has its own set of advantages. While several of the alkaline earth metals have a cooling transition in the UV, Ba^+ has the bluest transition at 493 nm. This is advantageous in ion cavity quantum electrodynamics (QED) experiments since the quality of optics and optical coatings in the visible wavelengths allows for a very high finesse cavity. Although blue light is more lossy through optical fibers than light at telecommunications wavelengths, 493 nm is much more suitable for fiber optics than other alkaline earth metal ion wavelengths [62]. Ba^+ is also potentially useful in a number of cold molecular ion experiments since it is the heaviest of the stable alkaline earth metal nuclei, making sympathetic cooling of heavy molecular ions more efficient [63].

Extending the techniques of laser cooling and precision spectroscopy to molecules has until recently been considered a particularly difficult challenge. Unlike neutral alkali metals or alkaline earth metal ions, even the simplest of molecules have a much more complicated level structure due to the presence of rotational and vibrational energy levels in addition to their electronic states, which often renders the number of lasers needed for quantum state

preparation and laser cooling prohibitively large. Nevertheless, there do exist a handful of molecules, both neutral and ionized, with level structures which are amenable to laser cooling with a manageable number of lasers. Among the neutrals, beams of SrF molecules have been laser cooled in the transverse direction [64] as well as slowed in the longitudinal dimension [65], and the related species YO has been confined in a 2-D magneto-optical trap (MOT). In each case, the combined electronic and rovibronic level structure requires only a small number of lasers. Some promising candidates for direct laser cooling of molecular ions include AlH^+ [66] BH^+ [66], and SiO^+ [67], although work with these species is still in the early stages. Additionally, there has been progress in precision rovibronic spectroscopy and optical state preparation with sympathetically cooled HD^+ molecules [68–70] as well as MgH^+ [71] and N_2^+ [72, 73].

Molecular ions are intriguing systems for several reasons besides simply extending the methods of laser cooling to new quantum systems. Certain ions, specifically those with a low-lying $^3\Delta$ state such as HfF^+ [11] and ThF^+ [74], may show enhanced sensitivity to an electron electric dipole moment. Studies of molecular ions are also of great interest in astrophysics as much of the molecular matter in the universe is in a plasma state, yet earth-bound spectroscopic data is severely limited [75–78]. Finally, the formation of molecular ions by reacting cold, trapped atomic ions with neutral atoms and molecules is rich with possibility both as a convenient way to produce molecular ions for use in further experiments as well as an ideal way to study reaction dynamics in the quantum regime, testing classical chemical models, and even examining isotopic effects in reactions [79]. Reactions in ion traps between ions and neutrals have been studied extensively for a number of ions [79–85]. Although many of these experiments involve a room temperature thermal distribution of neutral gas phase reactants, recent developments have allowed for detailed studies of low temperature reactions by velocity-selecting neutral reactants [18, 19, 86]. Hybrid quantum systems consisting of ions overlapped with neutral atoms confined in a MOT [87–89] or optical dipole force trap [90, 91] can also enhance our understanding of

quantum chemical processes.

In this thesis, Ba^+ ions are studied in the context of chemical reactions with several neutral halogen-containing molecules in order to produce BaX^+ (X = F, Cl, Br) molecular ions. These ions are of particular interest because of their closed shell electronic structure [92], making them especially suitable for reaching ultracold temperatures via sympathetic cooling by ultracold neutral atoms [93, 94]. Additionally, barium monohalide ions have rather large dipole moments, making them potentially useful in cavity QED experiments [95].

1.3 Organization of thesis

The remainder of this thesis is organized as follows. Chapter 2 provides a brief review of the principles behind ion trapping and laser cooling. Chapter 3 outlines a molecular dynamics simulation framework that was developed in order to model Coulomb crystals consisting of both laser cooled and sympathetically cooled ions for qualitative comparisons with experimental results. Chapter 4 discusses the various apparatus constructed for the experiments presented in this thesis, including the ion trap, RF electronics, and optics. Chapter 5 explains in detail the experimental setup for measuring electronic lifetimes of Th^{3+} and the results thereof. Chapter 6 describes experiments characterizing chemical reactions between cold, trapped Ba^+ ions and several different reactants in order to produce barium monohalide ions. Finally, Chapter 7 offers concluding remarks and some prospects for future directions with both Th^{3+} and molecular ion experiments.

Chapter II

ION TRAPPING

The confinement of charged particles has a long history, beginning in the 1950s with the invention of the Paul [96] and Penning [97] traps. In addition to these types of traps, there are also two others: electron beam ion traps (EBITs) [98] and Kingdon traps [99, 100]. The latter two are rarely used in experiments involving laser cooled ions, with the EBIT being used primarily in studies of highly charged ions [101] and the Kingdon trap frequently used for measurements of metastable ion lifetimes [102]. In contrast both the Paul and Penning traps are used extensively throughout atomic physics. The Paul configuration, named after its inventor and Nobel laureate Wolfgang Paul, confines ions using a combination of RF and DC electric fields whereas the Penning trap, invented by co-Nobel laureate Hans Dehmelt and named after Frans Penning, operates using static magnetic and DC electric fields. Of these two types of traps, the Paul trap generally offers much greater flexibility in design as well as better optical access. For these reasons, it is predominant in many experiments which require single ion resolution. This chapter presents a brief overview of the operating principles of a specific subclass of Paul traps, the so-called linear Paul trap, as well as some basic principles underlying laser cooling and properties of cold ion ensembles. For a more detailed approach, see Refs. [103, 104].

2.1 Dynamics of trapped ions

2.1.1 Formulation

The ideal linear Paul trap consists of a set of four infinitely long, parallel electrodes with hyperbolic cross section which share a common focus. The shortest distance from this focus and each electrode is denoted by r_0 (see Figure 2.1). In order to satisfy Laplace's equation, the potential at every point (x, y) contained within a cylinder of radius r_0 is given

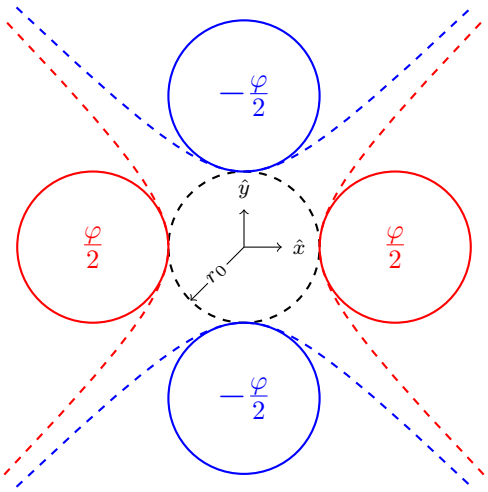

Figure 2.1: RF electrode configuration for the derivation of ion equations of motion. The red and blue dashed lines indicate ideal hyperbolic electrodes with applied potentials $\pm\varphi/2$, respectively. Ion guides and linear ion traps are usually constructed using circular cylinders rather than hyperbolic cylinders (solid circles). The nearest distance from the center to any electrode is denoted by r_0.

by[1]

$$\phi(x, y, t) = \varphi(t)\frac{x^2 - y^2}{2r_0^2}. \tag{2.1}$$

This saddle potential is illustrated in Figure 2.2. For a sinusoidally varying potential with angular frequency Ω,

$$\varphi(t) = U - V\cos(\Omega t), \tag{2.2}$$

the two dimensional equations of motion for an ion of mass m and charge Ze are then

$$\ddot{x} + \frac{Ze}{mr_0^2}[U - V\cos(\Omega t)]x = 0 \tag{2.3}$$

$$\ddot{y} - \frac{Ze}{mr_0^2}[U - V\cos(\Omega t)]y = 0. \tag{2.4}$$

[1]For hyperbolic electrodes, this potential is purely quadrupolar. For the more common circular cross section electrodes, higher order multipoles are introduced, but these are generally small enough to be ignored when the primary objective is not high resolution mass spectrometry.

These equations can be rewritten in the dimensionless canonical form of the Mathieu equation[2],

$$\frac{d^2u}{d\zeta^2} + [a - 2q\cos(2\zeta)]u = 0, \tag{2.5}$$

by making the substitutions

$$q = \frac{2ZeV}{mr_0^2\Omega^2} \tag{2.6}$$

$$a = \frac{4ZeU}{mr_0^2\Omega^2} \tag{2.7}$$

$$\zeta = \frac{\Omega}{2}t. \tag{2.8}$$

Equations (2.3) and (2.4) then become

$$\frac{d^2x}{d\zeta^2} + [a_x - 2q_x\cos(2\zeta)]x = 0 \tag{2.9}$$

$$\frac{d^2y}{d\zeta^2} + [a_y - 2q_y\cos(2\zeta)]y = 0, \tag{2.10}$$

with $q_x = -q_y = q$ and $a_x = -a_y = a$.

2.1.2 Stability of solutions

There are several ways to describe solutions to Equation (2.5). These include the so-called basic solutions and Floquet solutions [107, 108]. The basic solutions consist of two linearly independent solutions u_1 and u_2, one of which is even (u_1) whilst the other is odd (u_2). An example of such numerically computed (stable) solutions is presented in Figure 2.3. From this example, it can be seen that these solutions exhibit two types of motion: a slowly varying *secular motion* (sometimes called *macromotion*) and a rapidly varying *micromotion*. As will be shown later, the amplitude of the micromotion grows larger as the displacement of the ion from the trap center increases. For this reason, micromotion can be problematic and lead to excess heating if stray voltages push ions from the RF null at the trap center. This shall be discussed in more detail in Section 2.1.3.

[2]The Mathieu equation comes up in a number of interesting problems aside from ion trapping, including vibrations in elliptical drumheads and the quantum pendulum [105]. Similar differential equations, and thus stability criteria, even show up in recent spin-nematic squeezing work done with Bose-Einstein condensates elsewhere in the Chapman lab [106].

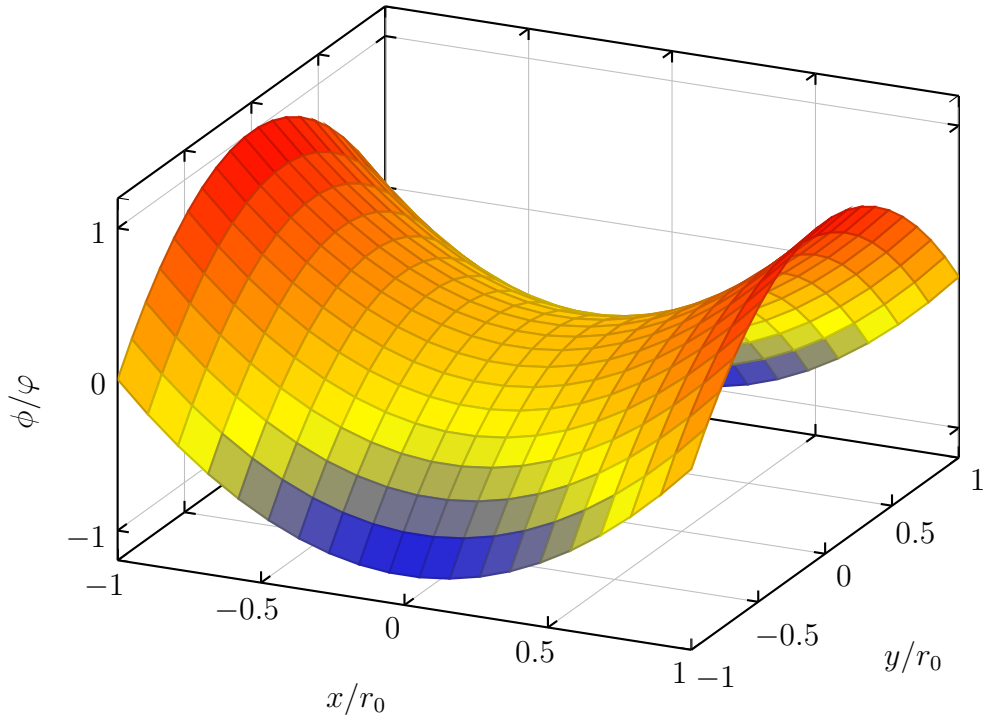

Figure 2.2: The quadrupole potential produced by Equation (2.1) at $t = 0$.

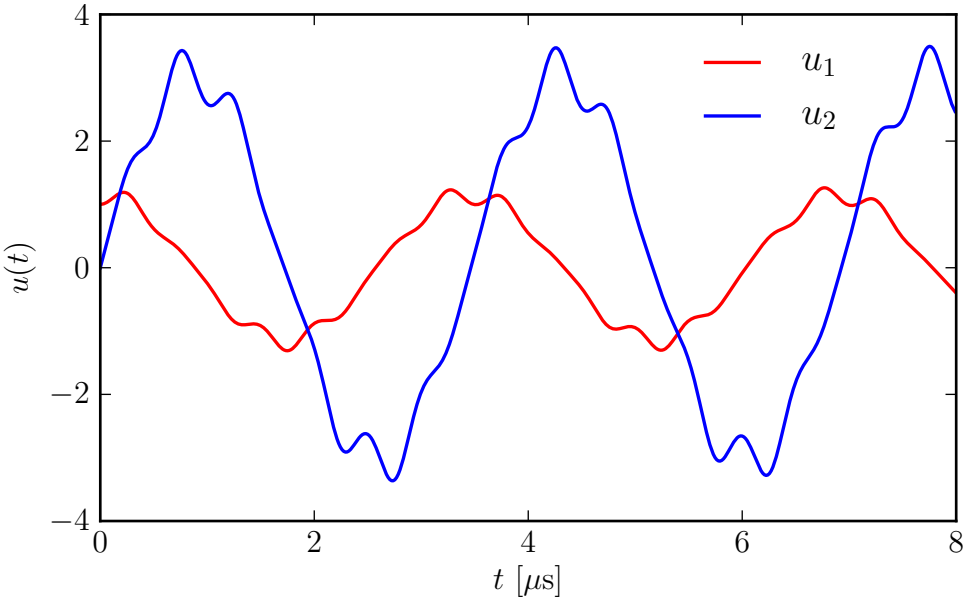

Figure 2.3: Numerically computed even (u_1) and odd (u_2) solutions to the Mathieu equations describing ion radial motion. In this example, $q = 0.25$ and $a = 0.05$ for an ion with $m/Z \approx 77.3$ amu (corresponding to Th^{3+}) in a trap of radius $r_0 = 3$ mm and RF frequency $\Omega = 2\pi \times 2$ MHz.

Solutions to Equation (2.5) are in general quite complicated and thus numerical computation is often the easiest approach. Solutions come in two flavors: stable, in which motion is oscillatory but bounded, and unstable, in which the motional amplitude diverges rapidly. Whether or not a particular solution is stable or unstable is determined by the values of q and a, and hence these are labeled the *stability parameters*.

Using the Floquet theorem, general solutions to Equation (2.5) can be expressed as [104, 107, 108]

$$u(\zeta) = A \sum_{n=-\infty}^{+\infty} C_{2n} e^{i(2n+\beta)\zeta} + B \sum_{n=-\infty}^{+\infty} C_{2n} e^{-i(2n+\beta)\zeta}, \tag{2.11}$$

where β is a real *characteristic exponent*, C_{2n} are coefficients that depend only on the stability parameters and are independent of initial conditions, and A and B are constants chosen to satisfy the initial conditions. By substituting (2.11) into (2.5), the following recursion relation for C_{2n} is obtained:

$$C_{2n+2} - D_{2n} C_{2n} + C_{2n-2} = 0, \tag{2.12}$$

where

$$D_{2n} = \frac{a - (2n+\beta)^2}{q}. \tag{2.13}$$

Note that β, a, and q are now all related through D_{2n}. With a little algebra, β can be expressed as a continued fraction [104]:

$$\beta^2 = a - q \left(\frac{1}{D_0 - \dfrac{1}{D_2 - \dfrac{1}{\cdots}}} + \frac{1}{D_0 - \dfrac{1}{D_{-2} - \dfrac{1}{\cdots}}} \right). \tag{2.14}$$

It can be shown that for integer β, the solutions of the form (2.11) are unstable, while non-integer β results in stable solutions [103]. Because of this, along with its incorporation of the stability parameters q and a, β is often referred to as *the* stability parameter. Diagrams showing regions of stability for solutions of (2.9) and (2.10) can be drawn using isolines of β as shown in Figure 2.4.

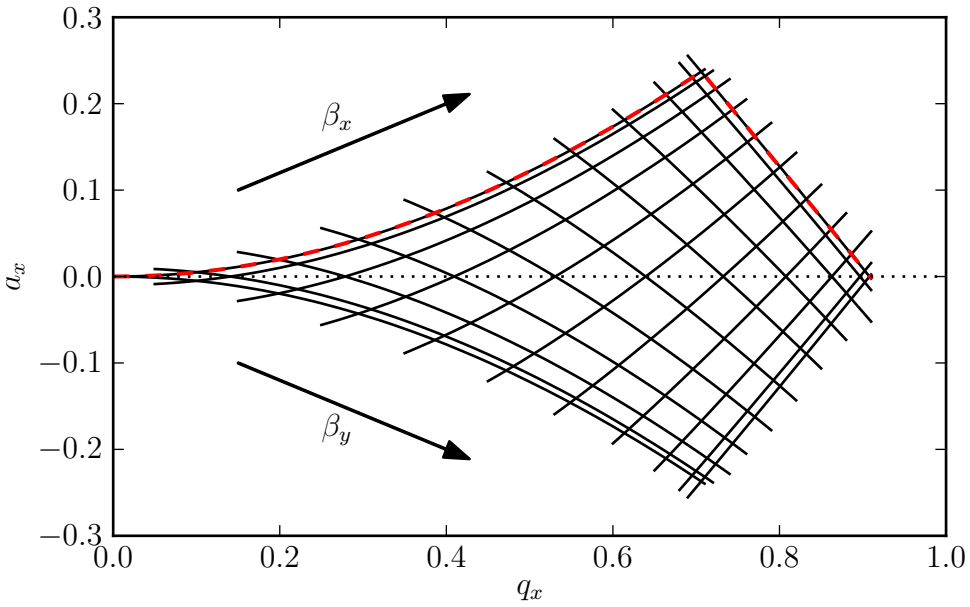

Figure 2.4: Isolines of the stability parameters β_x and β_y. The dashed line overlapping iso-β lines of values $\beta = 0$ and $\beta = 1$ is the same as the stability boundary as pictured in Figure 2.6.

As the equations of motion in x and y are independent, solutions in one dimension may be stable while solutions to the other are unstable. Stable solutions of Equation (2.9) [(2.10)] are said to be x-stable [y-stable]. For confinement of ions, solutions must be simultaneously x- and y-stable. Stability regions in each dimension can be computed[3] and overlaid in order to find regions which are simultaneously stable. This is shown in Figure 2.5 in which several regions of simultaneous stability are illustrated. Most ion traps operate at the first region of overlapping stability since this corresponds to the lowest required voltages, and henceforth discussion will be restricted to this first region which is shown in greater detail in Figure 2.6. By comparing Figures 2.4 and 2.6, it can be seen that the first stability region can also be defined in terms of β, as it is bounded in $q - a$ space by $\beta = 0$ and $\beta = 1$ [103].

[3]There are several methods available for computing regions of stability which are beyond the scope of the present discussion. One particularly simple matrix method is given in Ref. [109] and implemented in the Python code given in Appendix B.1.

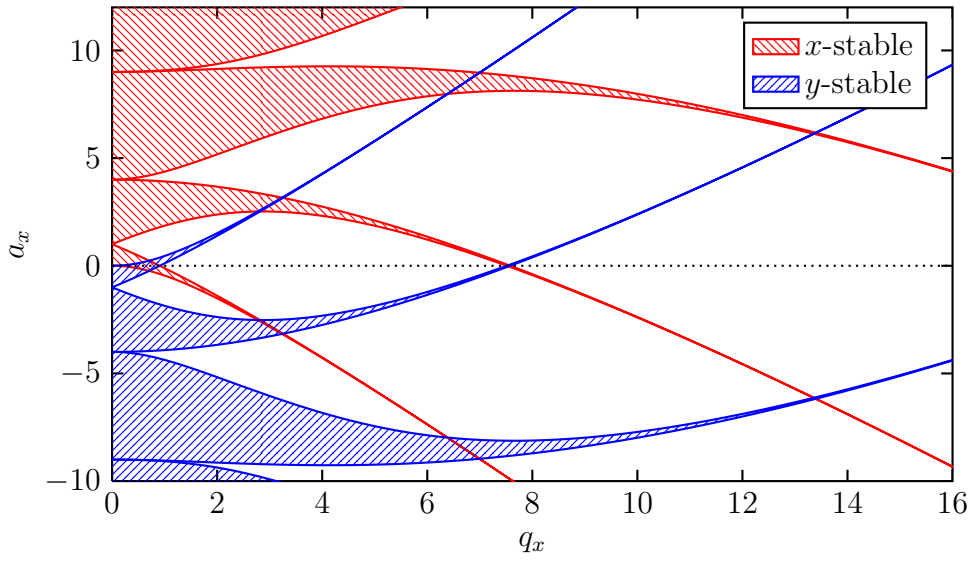

Figure 2.5: Regions of stability for the x (red) and y (blue) ion equations of motion. Overlapping regions of stability indicate where an ion is simultaneously x- and y-stable, and therefore trapped in two dimensions.

In order to compare stability parameters for different ion species, it is useful to approximate the boundary of the stability region with a piecewise polynomial fit. Specifically, a third order polynomial gives a good approximation of the stability boundary for $0 \leq q \leq 0.706$ while a linear fit gives a good reproduction for $0.706 < q < 0.915$:

$$a(q) = \begin{cases} \sum_{j=0}^{3} A_j q^j, & 0 \leq q \leq 0.706 \\ B_0 + B_1 q, & 0.706 < q \leq 0.915 \end{cases} \tag{2.15}$$

Values of the coefficients are given in Table 2.1. A Python class for quickly computing these values and converting between voltages and stability parameters for different ion species is given in Appendix B.2.

The dependence on the mass to charge ratio in both q and a makes a Paul trap highly mass selective. Rewriting Equations (2.6) and (2.7) in terms of the applied voltages V and U gives

$$V = \frac{m r_0^2 \Omega^2 q}{2Ze}, \qquad U = \frac{m r_0^2 \Omega^2 a}{4Ze}. \tag{2.16}$$

Stability curves for various ion species can then be plotted on the U-V plane. By ramping voltages along the line $U = (a/2q)V$, and utilizing some method of detecting charged

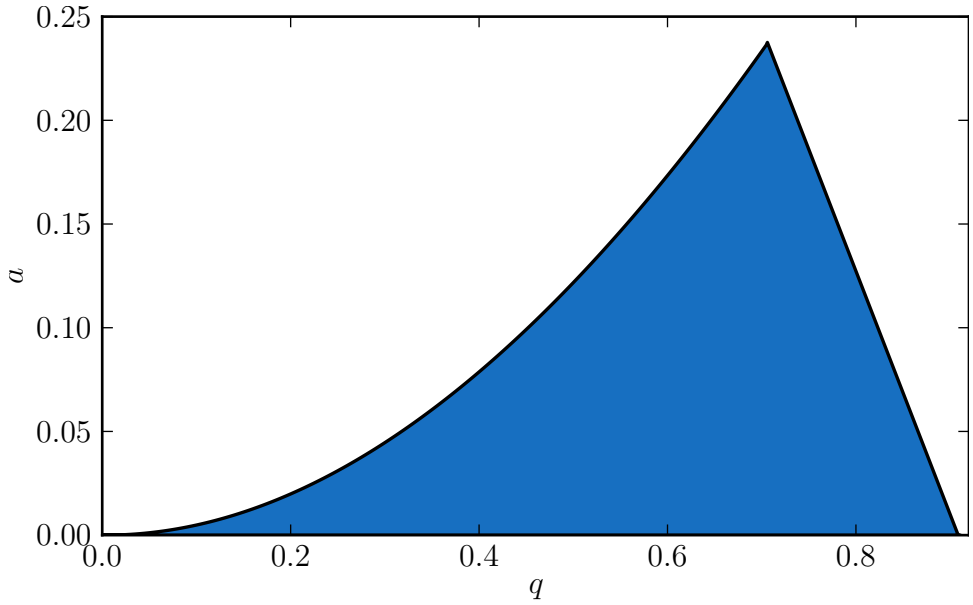

Figure 2.6: The first region of stability for ions in a linear Paul trap. Ions whose stability parameters lie in the shaded region have stable solutions to both Equations (2.9) and (2.10) and are therefore trapped in two dimensions. Paul traps typically operate only in this first region of overlapping stability since the required voltages are lowest.

Table 2.1: Piecewise polynomial fit coefficients for approximating the first stability region. The coefficients are defined by Equation (2.15) and prior text. See also Ref. [110].

Coefficient	Value
A_0	0
A_1	-3.23×10^{-3}
A_2	0.5256
A_3	-6.43×10^{-2}
B_0	1.0657
B_1	-1.173

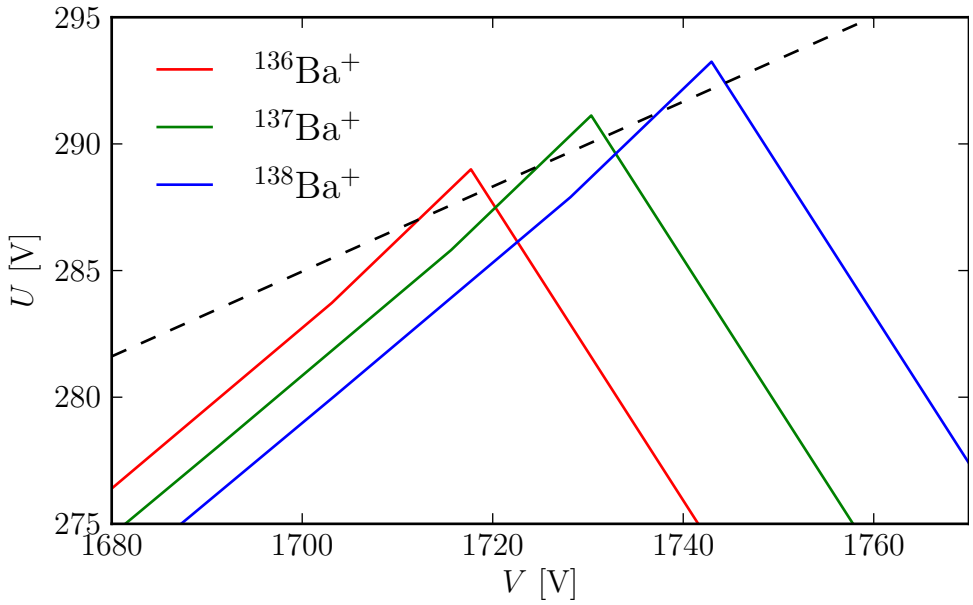

Figure 2.7: An example of mass selectivity by ramping the RF and DC voltages. Here, the stability diagrams for the three most common isotopes of Ba in a trap of radius $r_0 = 3.18$ mm and RF frequency $\Omega = 2\pi \times 2.93$ MHz are plotted in the U-V plane. The dashed line indicates a mass scan with slope $a/2q$ ($q = 0.695$, $a = 0.233$) sufficient to achieve the 1 amu mass resolution required to distinguish between the three Ba isotopes.

particles, m/Z ratios[4] can be readily distinguished [111]. An example using the three most abundant isotopes of barium is plotted in Figure 2.7. To achieve high mass resolution, a mass scan such as this must be performed near the apex of the stability diagram. This technique is commonly employed by mass spectrometers such as the Stanford Research Systems RGA series residual gas analyzer. It is worth noting that this is but one of many ways to use an ion trap as a mass spectrometer. Several more are described in Chapter 9 of Ref. [103], and two methods used experimentally are presented in Section 6.3.

2.1.3 The pseudopotential approximation

As discussed in Section 2.1.2 and illustrated in Figure 2.3, ion motion can be described by large amplitude, slowly varying secular motion and (hopefully) small amplitude, rapidly varying micromotion. From Equation (2.11), it is clear that solutions to Mathieu's equation

[4] Oftentimes when referring to the stability of different ion species in a Paul trap, the terms "heavier" and "lighter" are used to mean "larger m/Z" and "smaller m/Z," respectively since $Z = 1$ is most common.

exhibit oscillatory motion with frequencies $\omega_n = (2n + \beta)\zeta$. Using the definition of ζ from Equation (2.8), these frequencies can be rewritten in terms of the RF frequency Ω as [112]

$$\omega_n = \frac{2n + \beta}{2}\Omega. \tag{2.17}$$

The lowest order term,

$$\omega_0 = \frac{\beta}{2}\Omega, \tag{2.18}$$

is called the *secular frequency* and is the frequency associated with the larger amplitude motion seen in Figure 2.3. For $q \ll 1$, the lowest order expansion of Equation (2.14) gives [104, 112] $\beta \approx \sqrt{a + q^2/2}$ so that the secular frequency is usually expressed as[5]

$$\omega_0 = \left(a + \frac{q^2}{2}\right)^{1/2} \frac{\Omega}{2}. \tag{2.19}$$

In order to determine the frequency of the micromotion, we consider a composite solution ξ to Equation (2.5),

$$\xi = \xi' + \xi'', \tag{2.20}$$

where ξ' is the secular component and ξ'' is the micromotion component. Assuming the secular amplitude is much larger than that of the micromotion and that the secular frequency is much slower than the micromotion frequency, substituting Equation (2.20) into Equation (2.5) yields

$$\frac{d^2\xi''}{d\zeta^2} = -\left[a - 2q\cos(2\zeta)\right]\xi'. \tag{2.21}$$

Then for $|a| \ll |q|$[6],

$$\xi'' = \frac{q\xi'}{2}\cos(2\zeta). \tag{2.22}$$

Hence the micromotion oscillates at the applied RF frequency Ω (and is often subsequently explicitly labeled the *RF micromotion*) and has an amplitude proportional to the instantaneous secular motion amplitude (*i.e.*, the micromotion amplitude is larger as ions become

[5] Recall that a_x and a_y differ by a sign, and so in general there is a different secular frequency for the x and y dimensions. As such, the following discussion strictly speaking deals only with the x dimension, but can be generalized by explicitly adding the proper subscripts to both q and a.

[6] Although this is not always the case, ions are often trapped with $a = 0$ except when applying brief a pulses for ejecting unwanted ions of a particular mass to charge ratio.

displaced from the center of the trap).

Meanwhile, using this result in Equation (2.5) and averaging over one RF cycle yields the following differential equation for the secular motion [112]:

$$\frac{d^2\xi'}{dt^2} = -\left(a + \frac{q^2}{2}\right)\frac{\Omega^2}{4}\xi'. \tag{2.23}$$

Thus, near the trap center where micromotion is minimized, the ion can be treated as a harmonic oscillator with frequency ω_0 as given by Equation (2.19). The confining potential can therefore be expressed as the ponderomotive pseudopotential (for $a = 0$)

$$\psi_0(x, y) = \frac{1}{2}m\omega_0^2\left(x^2 + y^2\right). \tag{2.24}$$

In the absence of applied DC fields, the *trap depth* is expressed by evaluating Equation (2.24) at $x = y = r_0$ [103]:

$$\psi_D \equiv \psi_0(x = r_0, y = r_0) = \frac{1}{16}mq^2r_0^2\Omega^2. \tag{2.25}$$

A typical linear Paul trap has radius of order 1 mm and frequencies of a few MHz, allowing for trap depths of tens or even hundreds of eV. Compared to most neutral atom traps, this trap depth is enormous [113]. Having such a large trap depth is important when using laser ablation for trap loading as ions produced in this way have energies comparable to these trap depths [114].

Thus far, discussion of ion motion has been limited to radial motion in an infinitely long ion guide. To extend the treatment to a true ion trap, axial confinement must be considered. Ions are confined in the axial dimension by using DC *end cap* electrodes held at voltage U_{EC}. Near the trap center, the axial contribution to the potential can also be treated as harmonic:

$$\psi_z(z) = \frac{1}{2}\omega_z^2 z^2, \tag{2.26}$$

where the axial secular frequency ω_z is given by [115]

$$\omega_z = \sqrt{\frac{2Ze\kappa U_{EC}}{mz_0^2}}. \tag{2.27}$$

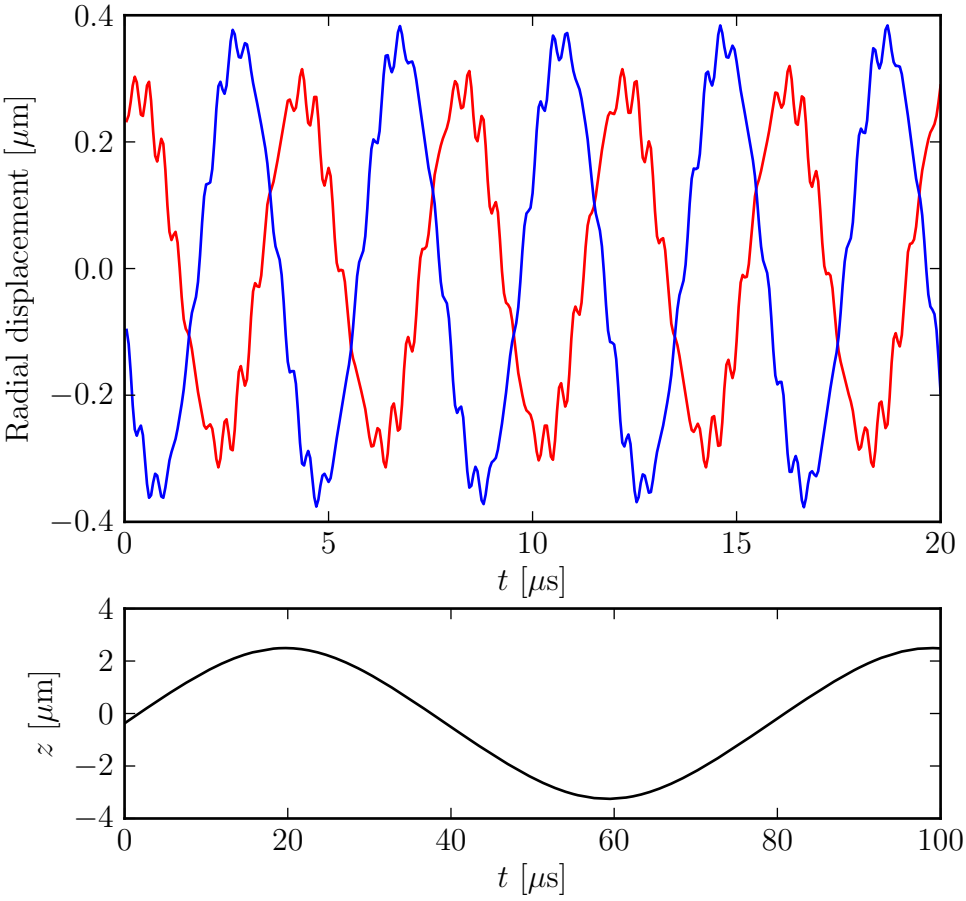

Figure 2.8: Ion trajectories in a simulated trap of radius $r_0 = 3.18$ mm, length $z_0 = 12.7$ mm, RF frequency $\Omega = 2\pi \times 2.93$ MHz, $q = 0.2$, $m/Z = 77.3$, and end cap voltage $U_{\mathrm{EC}} = 50$ V as computed by SIMION [116]. (Top) Radial trajectories in the x (red) and y (blue) directions. (Bottom) Axial trajectory. Note the difference in time scale between the top and bottom plots as well as the absence of micromotion in the z direction. Fitting the z component to a sinusoidal curve over several different values of q results in an axial secular frequency of $\omega_z \approx 2\pi \times 12.7$ kHz, making $\kappa \approx 0.008$.

Here, κ is a dimensionless parameter that takes into account the particular end cap geometry chosen and z_0 is half the distance between the two end caps. The κ parameter is not generally easily calculated from first principles, and so instead is most often determined by measuring the axial secular frequency either in simulations (see Figure 2.8) or experimentally (see Section 6.3.1).

With the addition of end cap electrodes, fringing fields near the ends of the trap modify the radial confinement, the details of which are given in Ref. [103]. The resulting radial

frequency becomes

$$\omega_r = \sqrt{\left(\omega_0^2 - \frac{1}{2}\omega_z^2\right)}. \tag{2.28}$$

Combining this modified radial frequency with the axial frequency of Equation (2.27) gives the full, three-dimensional pseudopotential

$$\psi(x, y, z) = \frac{ZeV^2}{m\Omega^2 r_0^4}\left(x^2 + y^2\right) + \frac{\kappa U_{EC}}{2z_0^2}\left(2z^2 - x^2 - y^2\right). \tag{2.29}$$

This pseudopotential can be used to simulate ion Coulomb crystals consisting of various ion species (as in Chapter 3). For the purposes of the ions studied in this thesis, Equation (2.29) is usually an excellent approximation for the trapping potential seen by a single ion and is adequate for simulating CCD images of large ion crystals composed of hundreds of ions of differing species.

2.2 *Ion interactions with light*

Laser cooling was first proposed independently by Hänsch and Shawlow in neutral atoms [117] and by Wineland and Dehmelt in atomic ions [118]. These techniques have since been improved upon and are now applied to a large number of neutral atoms, ions, and even a few molecules. When an ion does not possess a level structure conducive to laser cooling, it can still be cooled using sympathetic cooling (Section 2.3.2), buffer gas cooling, and a few other methods [103]. In this section, we consider the interactions between trapped atomic ions and light involved in laser cooling.

2.2.1 Three level atoms

Most atomic ions used in ion trapping experiments can be well approximated as a three level system (see Figure 2.9). In particular, we will confine ourselves to discussion of the so-called Λ system as it is of the most relevance to both Ba^+ and Th^{3+} ions as studied in this thesis. The Hamiltonian for any atomic system can be expressed as

$$\mathcal{H} = \mathcal{H}_A + \mathcal{H}_I, \tag{2.30}$$

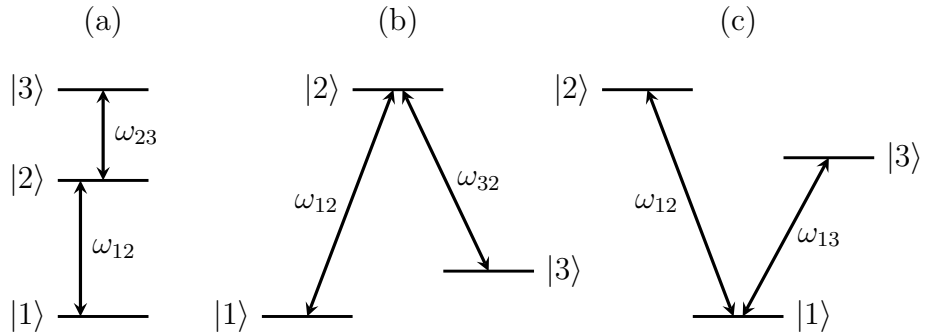

Figure 2.9: Various three level systems. (a) Ladder (or cascade). (b) Λ. (c) V. Of these, Λ three level systems are common to both Ba^+ and Th^{3+}. In each case, ω_{mn} denotes the transition frequencies between states $|m\rangle$ and $|n\rangle$.

where $\mathcal{H}_A = \sum_i \hbar\omega_i |i\rangle$ gives the energy of the system in the absence of external fields and the interaction Hamiltonian $\mathcal{H}_I$ describes the coupling between the atom and optical fields. In this formulation, we treat the system semiclassically such that the monochromatic laser fields are not quantized and we consider an atom with dipole operator $\mathbf{d} = Ze\mathbf{r}$. Defining the ground state $|1\rangle$ to be at zero energy, the atomic Hamiltonian reads

$$\mathcal{H}_A = \hbar\omega_{12} |2\rangle\langle 2| + \hbar(\omega_{12} - \omega_{32}) |3\rangle\langle 3| . \tag{2.31}$$

By judiciously multiplying by the identity, the dipole operator can be expanded:

$$\begin{aligned} \mathbf{d} &= \sum_{m,n} |m\rangle\langle m| \mathbf{d} |n\rangle\langle n| \\ &= |1\rangle\langle 1| \mathbf{d} |2\rangle\langle 2| + |1\rangle\langle 1| \mathbf{d} |3\rangle\langle 3| + |2\rangle\langle 2| \mathbf{d} |3\rangle\langle 3| + \text{h.c.} \end{aligned} \tag{2.32}$$

Here, we have already made use of the fact that the expectation value of the dipole operator with respect to an energy eigenstate must vanish when there is no permanent dipole moment as with atoms [119]. Furthermore, for a real atom in the Λ configuration, the $|3\rangle \leftrightarrow |1\rangle$ transition is not dipole-allowed, and therefore $\langle 1| \mathbf{d} |3\rangle = \langle 3| \mathbf{d} |1\rangle = 0$. Therefore, the interaction Hamiltonian is expressed as

$$\begin{aligned} \mathcal{H}_I(t) &= -\mathbf{d} \cdot [\mathbf{E}_{12}(t) + \mathbf{E}_{32}(t)] \\ &= \frac{\hbar}{2} \left[\Omega_{12} \left(e^{i\omega_{cl}t} + e^{-i\omega_{cl}t} \right) |2\rangle\langle 1| + \Omega_{32} \left(e^{i\omega_{rp}} + e^{-i\omega_{rp}} \right) |3\rangle\langle 2| + \text{h.c.} \right], \end{aligned} \tag{2.33}$$

where we have defined the Rabi frequencies

$$\hbar\Omega_{mn} = -\mathbf{d}\cdot\mathbf{E}_{mn} = -ZeE_{mn}\langle m|\,\mathbf{r}\,|n\rangle \tag{2.34}$$

and the electric fields as

$$\mathbf{E}_{12}(t) = \mathbf{E}_{12}\cos(\omega_{cl}t) \qquad\qquad \mathbf{E}_{32}(t) = \mathbf{E}_{32}\cos(\omega_{rp}t). \tag{2.35}$$

The frequencies ω_{cl} and ω_{rp} (the subscripts respectively standing for "cooling laser" and "repumper" for reasons which will be explained shortly) take into account the associated detunings Δ_{mn} of each laser from the atomic resonances:

$$\omega_{cl} = \omega_{12} + \Delta_{12} \tag{2.36}$$

$$\omega_{rp} = \omega_{32} + \Delta_{32}. \tag{2.37}$$

We now examine the population dynamics of the Λ system by considering the density matrix formalism. A general quantum state can be described by the density operator

$$\rho = \sum_i p_i\,|\psi_i\rangle\langle\psi_i|\,, \tag{2.38}$$

where $|\psi_i\rangle = c_1\,|1\rangle + c_2\,|2\rangle + c_3\,|3\rangle$ for a three level atom. The Liouville (or von Neumann) equation describes the evolution of a quantum state in the density matrix formalism and is analogous to the Schrödinger equation of wave mechanics [120]:

$$i\hbar\dot{\rho} = [\mathcal{H},\rho]. \tag{2.39}$$

This, however, neglects spontaneous emission. A common method for including this and other effects which couple the system to the environment is to define the Lindblad operator [121]

$$\mathcal{L} = \sum_n \frac{1}{2}\left(2C_n\rho C_n^\dagger - \rho C_n^\dagger C_n - C_n^\dagger C_n\rho\right), \tag{2.40}$$

where the sum is over all connected states, $C_n = \sqrt{\Gamma_n}A_n$ are collapse operators, A_n are operators which couple the system and the environment, and Γ_n are the associated rates. Combining this with Equation (2.39) yields the Lindblad master equation [122, 123]

$$\dot{\rho} = -\frac{i}{\hbar}[\mathcal{H}(t),\rho] + \mathcal{L}. \tag{2.41}$$

This equation is often useful when numerically simulating quantum systems since it allows for a relatively simple description of interaction terms in a Hermitian Hamiltonian while separating out decay terms which can be more easily described as stochastic processes. For the three level system, the relevant collapse operators are[7]

$$C_1 = \sqrt{b_{23}\Gamma_2}\,|3\rangle\langle 2| \qquad C_2 = \sqrt{b_{21}\Gamma_2}\,|1\rangle\langle 2| \tag{2.42}$$

$$C_3 = \sqrt{\Gamma_{cl}}\,|1\rangle\langle 1| \qquad C_4 = \sqrt{\Gamma_{rp}}\,|3\rangle\langle 3|\,. \tag{2.43}$$

Here, b_{mn} represents the branching ratio for decay from state $|m\rangle$ to state $|n\rangle$, $\Gamma_2 = \tau_2^{-1}$ is the inverse of the radiative lifetime of state $|2\rangle$, and Γ_{cl} (Γ_{rp}) is the linewidth of the cooling laser (repumper). Typically, $b_{21} > b_{23}$, and hence the laser at frequency ω_{cl} plays a larger role in cooling the ion whereas the laser at ω_{rp} pumps the ion out of the otherwise dark state $|3\rangle$ and is hence termed the repumper. Equations (2.42) represent spontaneous emission and Equations (2.43) represent the finite linewidths of the lasers [19]. To lowest order, the latter terms can be neglected given the assumption of monochromatic light.

In order to more easily integrate Equation (2.41), we first must transform into a different reference frame[8]. To do this, we transform $\mathcal{H}_I(t)$ with a unitary operator $U(t)$ in the following manner [124, 125]:

$$\tilde{\mathcal{H}}(t) = U^\dagger \mathcal{H} U - iU^\dagger \frac{\partial U}{\partial t}. \tag{2.44}$$

In the matrix formalism, the unitary operator for this transformation is [124]

$$U(t) = \begin{pmatrix} 1 & 0 & 0 \\ 0 & e^{-i\omega_{cl}t} & 0 \\ 0 & 0 & e^{-i(\omega_{cl}-\omega_{rp})t} \end{pmatrix} \tag{2.45}$$

[7] A fifth collapse operator could also be included to take into account the dipole-forbidden decay $|3\rangle \rightarrow |1\rangle$ while maintaining the dipole-only treatment of the interaction Hamiltonian (2.33).

[8] In the case of a two level system, the following transformation can be clearly interpreted as transforming into a rotating frame.

The Hamiltonian in the transformed frame is therefore

$$\tilde{\mathcal{H}}_I(t) = \hbar \begin{pmatrix} 0 & \frac{\Omega_{12}}{2}\left(1 + e^{-2i\omega_{cl}}\right) & 0 \\ \frac{\Omega_{12}^*}{2}\left(1 + e^{2i\omega_{cl}}\right) & -\Delta_{12} & \frac{\Omega_{32}^*}{2}\left(1 + e^{2i\omega_{rp}t}\right) \\ 0 & \frac{\Omega_{32}}{2}\left(1 + e^{-2i\omega_{rp}t}\right) & \Delta_{32} - \Delta_{12} \end{pmatrix}, \tag{2.46}$$

where rows and columns are written in the same numerical order as the states are defined.

Here we note that near the atomic resonances, $\omega_{rp} \gg \Delta_{32}$ and $\omega_{cl} \gg \Delta_{12}$, meaning that the the exponential terms of (2.46) vary rapidly and can therefore be neglected. This is known as the rotating wave approximation [120, 125]. By dropping these terms, the Hamiltonian loses its time dependence and becomes

$$\tilde{\mathcal{H}}_I^{\text{RWA}} = \hbar \begin{pmatrix} 0 & \frac{\Omega_{12}}{2} & 0 \\ \frac{\Omega_{12}^*}{2} & -\Delta_{12} & \frac{\Omega_{32}^*}{2} \\ 0 & \frac{\Omega_{32}}{2} & \Delta_{32} - \Delta_{12} \end{pmatrix}. \tag{2.47}$$

With this approximation, Equation (2.41) can finally be integrated. Combining everything, we obtain the following equations to describe the populations of the three states over time:

$$\begin{aligned} \dot{\rho}_{11} &= b_{21}\Gamma_2\rho_{22} + \frac{i}{2}\left(\Omega_{12}^*\rho_{12} - \Omega_{12}\rho_{21}\right) \\ \dot{\rho}_{22} &= \frac{i}{2}\left(\Omega_{12}\rho_{21} + \Omega_{32}\rho_{23} - \Omega_{12}^*\rho_{12} - \Omega_{32}^*\rho_{32}\right) \\ \dot{\rho}_{33} &= b_{23}\Gamma_2\rho_{22} + \frac{i}{2}\left(\Omega_{32}^*\rho_{32} - \Omega_{32}\rho_{23}\right) \end{aligned} \tag{2.48}$$

Equations (2.48), along with the equations for the off-diagonal coherences not discussed here, are known as the optical Bloch equations. Note that these equations can be reduced to the familiar results for a two level system by setting $b_{21} = 1$ and $b_{23} = \Omega_{32} = 0$. The results of a numerical integration of Equation (2.41) near saturation is shown in Figure 2.10.

For comparison, it is also worthwhile to consider a simpler rate equation model. Using the excitation and decay rates as defined in Figure 2.11, for populations N_1, N_2, and N_3 of

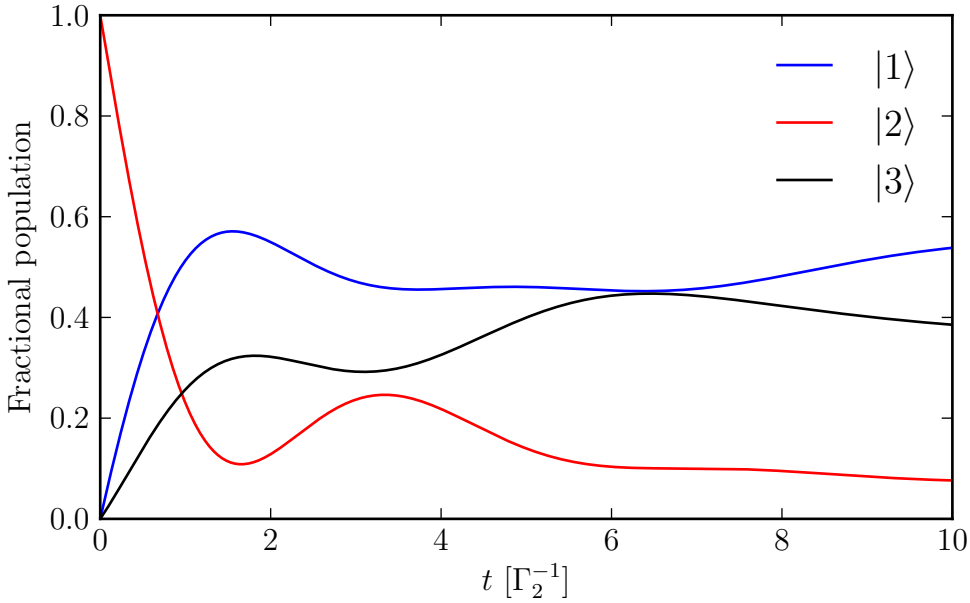

Figure 2.10: Results of numerical integration of the three level system near saturation. Here, the branching ratio favors the ground state over the metastable state 3:1 (as with Ba^+) and cooling and repumper lasers are detuned $-2\Gamma_2$ and $-\Gamma_2$, respectively. The numerical integration code for producing this plot is given in Appendix B.3.

the ground, excited, and metastable states, the system evolves according to

$$\begin{aligned}
\dot{N}_1 &= -N_1\Omega_{12} + N_2\Gamma_{21} \\
\dot{N}_2 &= N_1\Omega_{12} - N_2(\Gamma_{21} + \Gamma_{23}) + N_3\Omega_{32} \\
\dot{N}_3 &= -N_3\Omega_{32} + N_2\Gamma_{23}.
\end{aligned} \tag{2.49}$$

In the case of low intensity lasers, the rate equation model is in very good agreement with the semiclassical model (see Figure 2.12). A more thorough comparison of the optical Bloch equations and the rate equations is given in Ref. [126].

2.2.2 Doppler cooling

A simple model of the Doppler cooling of ions can be constructed by considering the optical Bloch equations described above. In the case where we are not concerned with the precise internal state of the ion, it is sufficient to consider the further simplification of a two level system. The rate at which ions scatter photons is simply the linewidth multiplied by the

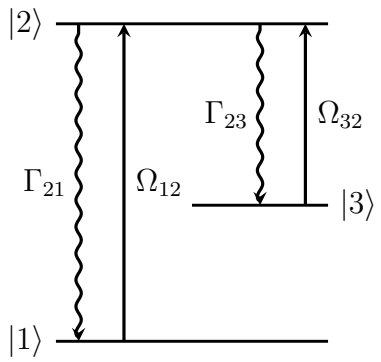

Figure 2.11: Definition of terms for the rate equation model of the three level Λ system.

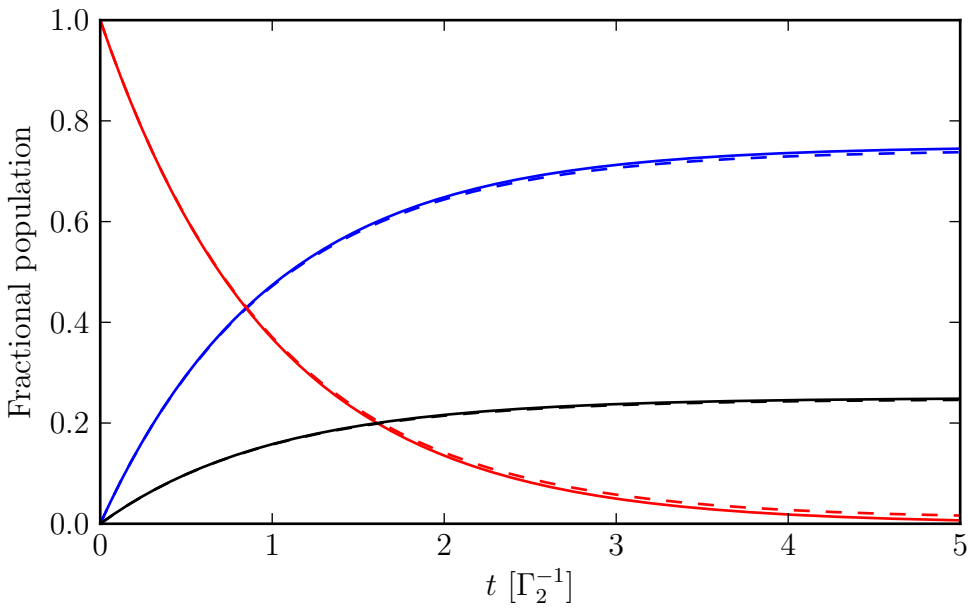

Figure 2.12: Comparison of three level system models with low intensity laser fields for Ba^+ ions. The solid lines are the result of numerically integrating Equation (2.41) with the Hamiltonian (2.47) while the dashed lines give the populations using the rate equations (2.49). The ground, excited, and metastable states are colored blue, red, and black, respectively. The numerical integration code for producing this plot is given in Appendix B.3.

population in the excited state [120]:

$$\gamma_p = \Gamma\rho_{22} = \frac{s_0\Gamma/2}{1 + s_0 + (2\Delta/\Gamma)^2}, \tag{2.50}$$

where $s_0 = I/I_s$ is the on-resonance saturation parameter. For an ion at rest, the average force due to absorption followed by spontaneous emission in the presence of a laser with wavevector $\mathbf{k}$ is then simply

$$\mathbf{F} = \hbar\mathbf{k}\gamma_p = \frac{\hbar\mathbf{k}s_0\Gamma/2}{1 + s_0 + (2\Delta/\Gamma)^2}, \tag{2.51}$$

Using this expression alone, it is possible to simulate the cooling of an ion confined by the pseudopotential (2.29) by taking into account the Doppler shift due to the velocity of the ion (*i.e.*, $\Delta \rightarrow \Delta + \mathbf{k}\cdot\mathbf{v}$)[9]. It is thus a viscous model of laser cooling which neglects photon recoil effects. An example of using this simple model to simulate cooling of an ion from room temperature is shown in Figure 2.13. A more realistic model would include photon recoil and other effects, but it turns out to be sufficient for reproducing images of Coulomb crystals when incorporated in the more sophisticated molecular dynamics simulations presented in Chapter 3.

The minimum achievable temperature with Doppler cooling can be determined by considering the maximum possible scattering rate. From Equation (2.50), it is clear that γ_p saturates to a maximum value of $\Gamma/2$ at zero detuning. Therefore, the Doppler limit is defined by

$$k_B T_D = \frac{\hbar\Gamma}{2}. \tag{2.52}$$

A typical ion or neutral atom commonly used with laser cooling often has a natural linewidth of a few MHz and therefore a Doppler limit of a few hundred μK. For instance, The Ba^+ $S_{1/2} \leftrightarrow P_{1/2}$ cycling transition has a natural linewidth of $\Gamma \approx 2\pi \times 15$ MHz, and so its

[9]Note that this force is the same as one-dimensional optical molasses with a single laser and therefore a three-dimensional simulation using this expression alone would only result in cooling along the direction of $\mathbf{k}$. In reality, the fringing fields provide enough coupling of the axial and radial motion to allow for laser cooling in all three dimensions using only axial beams.

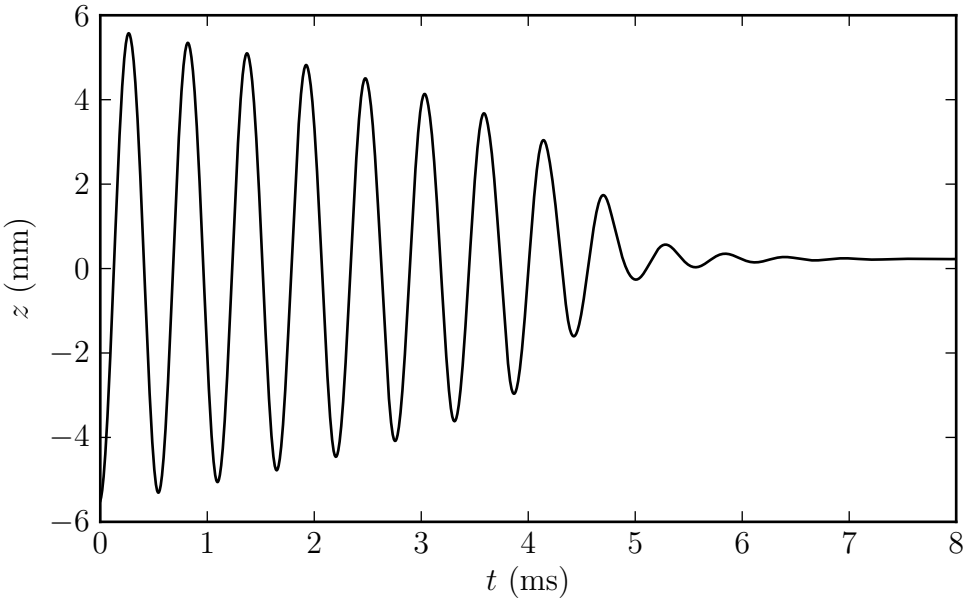

Figure 2.13: An example of using the force of Equation (2.51) and the pseudopotential (2.29) to create a crude model of Doppler cooling of an ion in a linear Paul trap. Here, a $^{138}Ba^{+}$ ion is being cooled by a laser introduced along the z axis. The laser has detuning $\Delta = -2\Gamma$ and saturation parameter $s_0 = 2$. The code for producing this simulation can be found in Section B.4.

Doppler limit is about 360 μK. In practice, various heating effects lead to a higher temperature, typically up to several tens or even hundreds of mK. To achieve lower temperatures, other techniques such as optical sideband cooling are necessary [127].

In order to measure the temperature of trapped ions when only Doppler cooling, the Doppler broadened linewidth can be measured by observing the amount of fluorescence at different detunings. Since Doppler broadening gives rise to a Gaussian profile but power broadening and the natural lineshape are Lorentzian, the measured linewidth will be of a Voigt lineshape. The full width at half maximum for the Gaussian component of this convolution is related to the ions' temperature by [126]

$$\text{FWHM} = 2\omega\sqrt{\frac{2k_B T \ln(2)}{mc^2}}, \tag{2.53}$$

where $\omega = 2\pi c/\lambda$ is the transition frequency. For cold, crystallized ions, scanning a laser frequency results in a very sharp, nearly Lorentzian enhancement in fluorescence followed by a rapid drop off as the laser becomes blue detuned from resonance. For ions in the gas

phase, thermal effects dominate and the lineshape is much more Gaussian. Examples of such measurements are given in Figure 2.14. For laser cooled ions, to extract a temperature estimate, one must estimate the expected power broadening and obtain a Gaussian width by using the Voigt deconvolution formula

$$\Delta\nu_G = \sqrt{\Delta\nu_L(\Delta\nu_L - \Delta\nu_{PB})}, \tag{2.54}$$

where $\Delta\nu_G$ is the deconvolved Gaussian FWHM, $\Delta\nu_L$ is the measured Lorentzian linewidth, and $\Delta\nu_{PB}$ is a lower bound estimate on power broadening [128]. Because for light red detuned far from resonance the ions are at a higher temperature than they are for light closer to resonance, the measured lineshape will be broadened, and thus this form of temperature measurement will only ever give an upper bound limit. A better temperature measurement method which would work on a chain of ions rather than a large crystal would be to laser cool only a few of the ions with a fixed frequency cooling beam and measure the lineshape of a sympathetically cooled ion with a weak, secondary probe beam [129]. By doing so, the probed ion is kept cold by the laser cooled ions and the measured lineshape is a full Voigt profile.

Several sources of heating exist which compete with Doppler cooling. These include collisions with background gases, blackbody radiation, RF heating, and so-called anomalous heating [130]. Heating from collisions is straightforward to solve by improving the quality of the vacuum. Although it is not necessary for the experiments presented here, a cryogenic environment can greatly benefit quantum information experiments dependent on ions being in the motional ground state [131, 132] as well as studies that are sensitive to blackbody radiation, such as those of molecular ions near the rovibrational ground state [69, 71, 130, 133]. Of the remaining heating mechanisms, the most important to the work presented here is due to RF heating. A discussion on how to minimize this effect is given in Section 4.1.

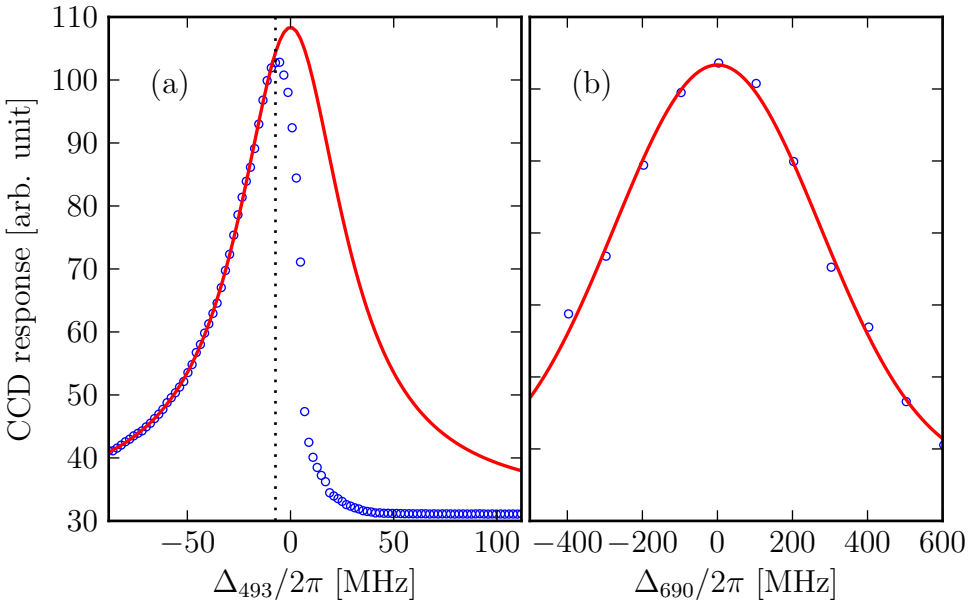

Figure 2.14: Temperature measurement of trapped ions. (a) Frequency sweep of the 493 nm cooling laser on a large number of cold Ba^+ ions. The rapid drop off in fluorescence on the right is due to the ions being heated instead of cooled for blue detuned light. The portion of the data to the left of and up to the dotted line is fit to a Lorentzian and has a linewidth of 30.9(5) MHz. Power broadening is the dominant source of broadening here and assuming a saturation parameter of $s_0 = 3$, an upper bound on the temperature is 32 mK. (b) Fluorescence of a cloud of Th^{3+} ions in He buffer gas as a function of detuning of the 690 nm laser. The data is fit to a Gaussian profile and has a FWHM of 646(33) MHz which corresponds to a temperature of $\approx$ 1000 K.

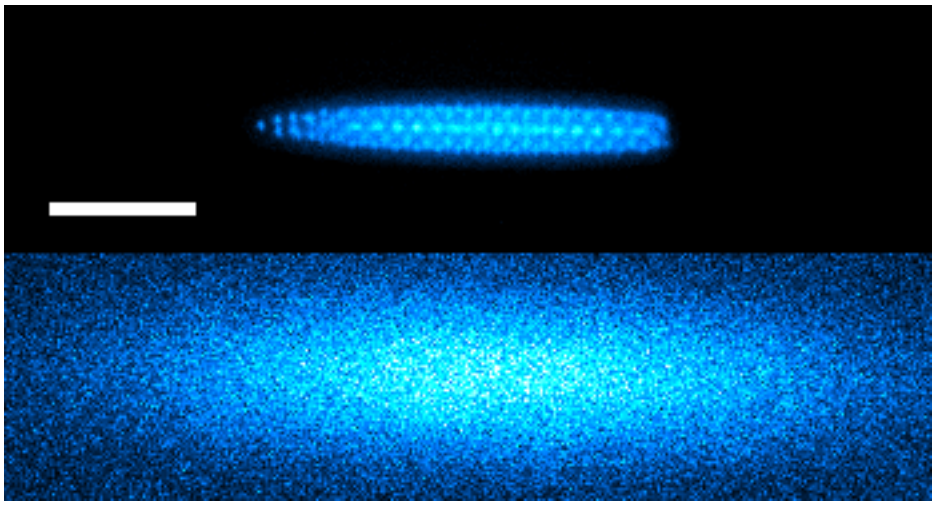

Figure 2.15: A comparison of Ba^+ ions in (top) crystal and (bottom) cloud phases. Each image contains the same ions with the phase change induced by altering the detuning of the 493 nm cooling laser. The scale bar measures 200 μm.

2.3 Coulomb crystals and sympathetic cooling

Ions stored in an ion trap at high temperatures are in a gas-like plasma phase. With Doppler cooling, ions will undergo phase transitions first into a liquid-like state and ultimately into an ordered, crystalline-like state commonly referred to as a Coulomb crystal (see Figure 2.15). Such structures have been observed in so-called dusty plasmas [134], charged liquids [1], and laser cooled atomic ions. Applications of laser cooled atomic ion crystals include studying reaction dynamics as in this work, quantum computing [13], cavity QED [135], and sympathetic cooling of other ionic species [136].

2.3.1 Coulomb crystals

The thermodynamic properties of a one component plasma can be described entirely by the dimensionless plasma coupling parameter [137–139]:

$$\Gamma = \frac{(Ze)^2}{4\pi\epsilon_0 k_B T a_{WS}}, \tag{2.55}$$

where a_{WS} is the Wigner-Seitz radius (the radius of the largest sphere containing a single ion) [140]

$$a_{WS} = \left(\frac{3}{4\pi n}\right)^{1/3}, \tag{2.56}$$

and n is the zero-temperature particle number density. The plasma coupling parameter can be thought of as the ratio of the Coulomb potential energy between ions and the average kinetic energy per ion. Thus, a larger value of Γ corresponds to a stronger coupling of the plasma. For $\Gamma \approx 2$, the plasma enters a liquid-like phase, and for $\Gamma \gtrsim 170$, the plasma becomes a highly ordered Coulomb crystal. As an example, typical inter-ion spacing in a crystal of Ba^+ ions is of order 10 μm. This leads to a Wigner-Seitz radius $a_{WS} \approx 6\,\mu$m. At a temperature of 10 mK, the plasma coupling parameter is $\Gamma \approx 280$. This is a fairly common value for many experiments using Coulomb crystals, with $\Gamma < 1000$ being the norm.

For multi-component crystals, the structure of the crystal is dependent on the masses of the constituent ions. Considering the expression for the trap depth [Equation (2.25)] and the q parameter [Equation (2.6)], lighter ions are more tightly confined than heavier ions at a given RF voltage. As a consequence, less massive ions will form a core at the center of a multi-component Coulomb crystal while more massive ions will form shells surrounding the lighter ions. Examples of multi-component Coulomb crystals are given in Figure 2.16 (see also simulated CCD images in Chapter 3).

2.3.2 Sympathetic cooling

Although direct laser cooling of ions is an incredibly useful technique, it suffers from generality in that only a select number of ions can be cooled in this way. Furthermore, the presence of a laser field necessarily perturbs the ion electronic level population, an undesirable result for some precision spectroscopic measurements. Both of these problems can be circumvented, however, by exploiting the strong Coulomb interaction between trapped ions. With at least one laser cooled ion present, another ion which is not illuminated by the cooling light (or far from resonance from it) will exchange energy with the laser cooled ion and thus be cooled. This effect is known as sympathetic cooling and was first demonstrated by Larson *et al.* for performing spectroscopy on Hg^+ ions that were sympathetically cooled by laser cooled Be^+ ions [141]. Similar spectroscopic techniques have been further refined

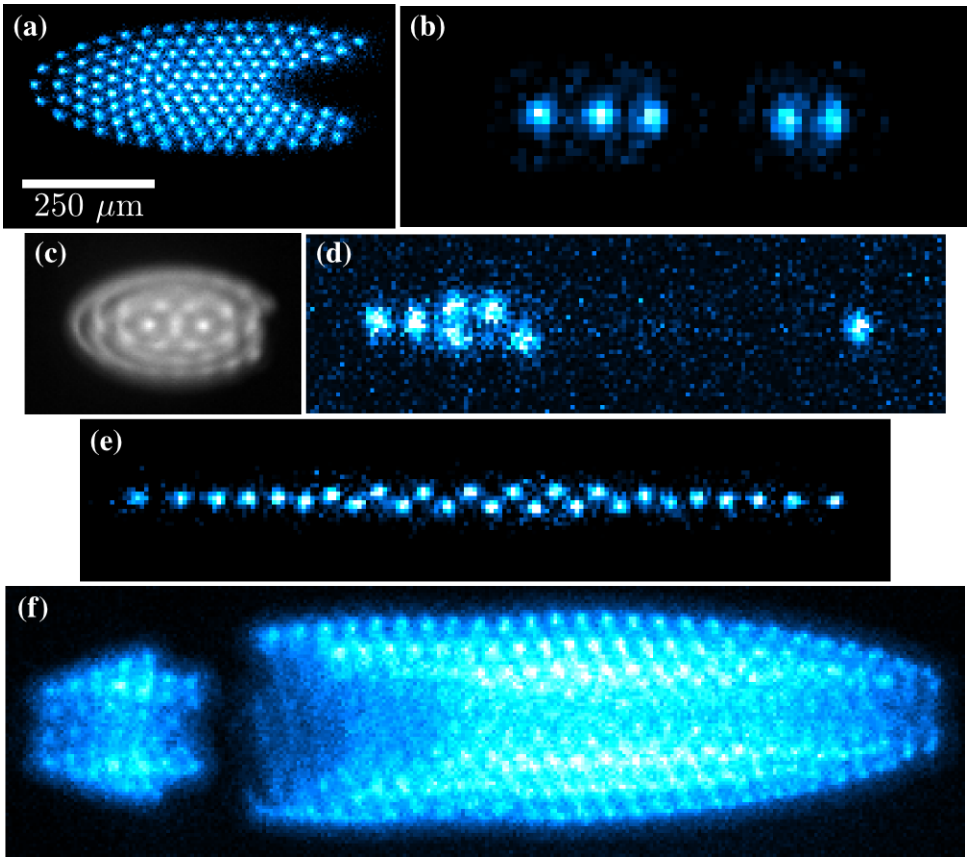

Figure 2.16: A collection of images of Coulomb crystals. (a) A crystal of $^{138}Ba^{+}$ and other isotopes with DC offsets applied to the RF electrodes. (b) Five $^{138}Ba^{+}$ ions and several non-fluorescing Ba^{+} ions of other isotopes in a linear chain. (c) Ba^{+} ions happy to be confined in a Paul trap. (d) A 2-D crystal consisting of mostly non-fluorescing Ba^{+} isotopes. (e) A 2-D "zig-zag" configuration. (f) A multi-component Coulomb crystal consisting of several Ba^{+} isotopes, Th^{+}, and Th^{2+} ions. Ions that are effectively lighter than Ba^{+} (*e.g.*, Th^{2+}) form a central core which can be seen here as a dim region along the central axis. A "dent" on the outer portion of the crystal indicates the presence of ions heavier than Ba^{+} (*e.g.*, Th^{+}).

over the years with the advent of quantum logic spectroscopy, in which a single laser cooled ion is used for quantum state preparation and detection of a single sympathetically cooled ion [142–144]. Such techniques have allowed for unprecedented precision in frequency measurements [9, 10].

More relevant to the work presented here is the ability for laser cooled atomic ions to sympathetically cool the translational motion of molecular ions. Combined with several techniques for cooling the internal rovibrational degrees of freedom [69, 71, 94], sympathetic cooling of molecular ions allows for highly precise spectroscopic measurements similar to those long possible with cold atomic ions. Additionally, as will be seen in Chapter 6, sympathetic cooling of molecular ions is also useful for characterizing reactions between stored ions and neutral molecules.

2.4 Summary

In this chapter, the basic concepts of ion confinement in a linear Paul trap and the resulting ion dynamics have been discussed. Additionally, general concepts and properties of Coulomb crystals and sympathetic cooling have been presented. This formulation is important for the molecular dynamics simulations presented in Chapter 3 as well as in understanding and interpreting results from experiments measuring Th^{3+} electronic lifetimes (Chapter 5) and characterizing reactions between trapped Ba^{+} ions and neutral gas phase reactants (Chapter 6).

Chapter III

MOLECULAR DYNAMICS SIMULATIONS

When conducting experiments involving sympathetically cooled ions which cannot be fluoresced, molecular dynamics (MD) simulations provide a powerful way of analyzing and visualizing the entire system. Originally motivated by the desire to be able to reproduce mass spectra of the motional resonance coupling method (Section 6.3.1), IonMD, an open source MD simulation of multi-component Coulomb crystals, was developed closely following the work of Refs. [145, 146]. Although it was ultimately not used for this purpose, these MD simulations still proved useful by providing a qualitative way of visualizing sympathetically cooled ions which normally would not fluoresce.

Molecular dynamics is a method of simulating the dynamics of systems of particles by evaluating Newton's equations of motion for every particle at each discrete time step. In that sense, it is largely a classical, brute force approach to studying complex dynamics, but can be very useful for understanding and modeling emergent phenomena [147], many-body dynamics [148], and more [149–151]. MD methods were first developed by Alder and Wainwright in the late 1950s [152, 153], but it was not until the 1970s that computers were advanced enough for simulations of more realistic systems [154]. Today, personal computers often have sufficient computing power to perform a wide variety of MD simulations in a reasonable amount of time. This chapter provides an overview of MD simulations performed for simulating multi-component Coulomb crystals and presents some of their results.

3.1 Theoretical overview

For N ions in a linear Paul trap, the force on the ith ion is given by

$$\mathbf{F}_i(\mathbf{r}_i, \mathbf{v}_i, t) = \mathbf{F}_{T,i}(\mathbf{r}_i, t) + \mathbf{F}_{C,i}(\mathbf{r}_1, \mathbf{r}_2, \ldots, \mathbf{r}_i, \ldots, \mathbf{r}_N) + \mathbf{F}_{L,i}(\mathbf{v}_i) + \mathbf{F}_{S,i}(t), \tag{3.1}$$

where $\mathbf{F}_{T,i}$ is the force due to the trapping potential, $\mathbf{F}_{C,i}$ is the Coulomb interaction between ions, $\mathbf{F}_{L,i}$ is the laser force which only acts on laser cooled ions, and $\mathbf{F}_{S,i}$ represents stochastic processes such as collisions with background gases. The force $\mathbf{F}_i$ is applied to every ion at every time step Δt. In this way, MD simulations are fully classical descriptions which can only take into account quantum effects by incorporating them in semiclassical force models (as in $\mathbf{F}_{L,i}$) or stochastic effects.

3.1.1 Trapping potential

The trapping potential is most easily dealt with by using the pseudopotential (2.29) described in Section 2.1.3. To include RF micromotion, the potential near the center of the trap could instead be expressed as [103]

$$\psi_\mu(x, y, z, t) = \frac{2V}{r_0^2}(x^2 - y^2)\cos(\Omega t) + \kappa\frac{U_{EC}}{2z_0^2}(2z^2 - x^2 - y^2). \tag{3.2}$$

Due to the $\cos(\Omega t)$ term, when including RF micromotion effects, the time step Δt must be around 100 times smaller than $2\pi/\Omega$ in order to smoothly approximate the micromotion. In practice, this greatly extends the computing time. Since experiments with Coulomb crystals are often conducted at low values of q where micromotion is small compared to the secular motion, it is more practical to neglect the micromotion so that time steps instead need only smoothly reproduce the secular motion. A stronger justification for considering only the pseudopotential (2.29) is given in Ref. [145].

3.1.2 Laser force

For simulating laser cooling, a two level ion is considered. The laser force can most simply be modeled as a viscous damping force plus a constant radiation pressure force in the

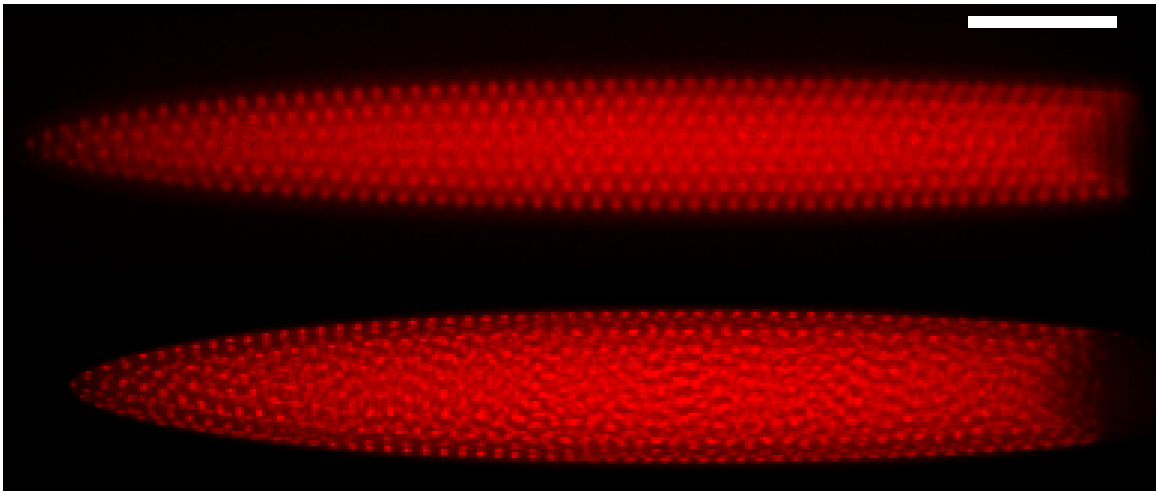

Figure 3.1: Experimental (top) and simulated (bottom) images of ion crystals showing isotope sorting. In each case, the red colored ions are $^{138}Ba^{+}$ ions and sympathetically cooled Ba^{+} ions of other isotopes are not visible. The scale bar is 200 μm in length.

direction of the laser:

$$\mathbf{F}_{L,i} = \mathbf{F}_0 - \beta \mathbf{v}_i, \tag{3.3}$$

where β must be positive to ensure damping. It is often sufficient experimentally to use a single laser introduced axially for laser cooling in which case $\mathbf{F}_0 = F_0\hat{\mathbf{k}} = \pm F_0\hat{\mathbf{z}}$. This pressure term results in an offset from the trap center for laser cooled ions and is most noticeable experimentally as an apparent asymmetry in a Coulomb crystal consisting of two or more isotopes of a particular atomic ion (*e.g.*, when lasers are detuned appropriately for $^{138}Ba^{+}$, other isotopes which do not fluoresce collect on the end of the trap nearest the introduction of the beams). This is illustrated both experimentally and in MD simulations in Figure 3.1. To simulate balanced beams (*i.e.*, a pair of beams in both the $+\hat{\mathbf{z}}$ and $-\hat{\mathbf{z}}$ directions), simply setting $F_0 = 0$ is sufficient.

The two terms of Equation (3.3) can be found by considering an ion in motion with velocity $\mathbf{v}$. This is most easily done by Doppler shifting the detuning, *i.e.* replacing Δ with $\Delta + \mathbf{k} \cdot \mathbf{v}$, and applying this substitution to the force due to absorption followed by spontaneous emission given in Equation (2.51). Considering the one-dimensional case

with the ion moving in the opposite direction as the laser, the force becomes

$$F = -\hbar k \frac{s_0 \Gamma/2}{1 + s_0 + [2(\Delta + kv)/\Gamma]^2}. \tag{3.4}$$

When the ion is moving slowly, *i.e.*, when the Doppler broadening is small compared to its natural linewidth Γ, a Taylor series expansion around $v = 0$ gives the expression [104]

$$F = F|_{v=0} + v \left.\frac{dF}{dV}\right|_{v=0} + O\left(v^2\right). \tag{3.5}$$

Performing the derivative and evaluating at $v = 0$ results in the damping coefficient β as defined in Equation (3.3) as

$$\beta = -\hbar k^2 \frac{4 s_0 (\Delta/\Gamma)}{[1 + s_0 + (2\Delta/\Gamma)^2]^2}. \tag{3.6}$$

Note the explicit negative sign ensures that for red-detuned light ($\Delta < 0$), β is positive and therefore damps ion motion. Damping is maximized when $\Delta = -\Gamma/2$ and $s_0 = 2$ which gives $\beta_{\max} = \hbar k^2/4$. For Ba^+, with a cooling laser wavelength of 493 nm and a transition linewidth of $\Gamma \approx 2\pi \times 15$ MHz, this evaluates to $\beta_{\max} \approx 4.3 \times 10^{-21}$ kg/s. More realistically, the damping coefficient ends up being around an order of magnitude lower than this maximum value. Since the Doppler shift does not change significantly for ions that are already at low temperatures, and because the magnitude of β is generally small, the damping coefficient is given to the simulation as a constant parameter that is provided at run time.

From Equation (3.5), the radiation pressure term F_0 is clearly described by the force from spontaneous emission for an ion at rest and a laser at zero detuning:

$$F_0 = -\hbar k \frac{\Gamma}{2} \frac{s_0}{s_0 + 1}. \tag{3.7}$$

The magnitude of this force saturates to $F_0 = -\hbar k \Gamma/2$ and typical values for F_0 are of order 10^{-20} kg·m/s^2 ($F_0 \leq 6.3 \times 10^{-20}$ kg·m/s^2 for Ba^+). As with the damping term, since this force is quite small, it is passed as a fixed parameter at the beginning of each simulation run. Although only the one-dimensional case is considered above, it is straightforward to translate back into vector notation for the three-dimensional case.

3.1.3 Coulomb interaction

The Coulomb interaction is modeled by treating all ions as point particles and computing the force on each ion due to every other ion. These calculations thus take up the majority of the computational time since this requires $O(N^2)$ computations. The force on ion i is

$$\mathbf{F}_{C,i} = \frac{Z_i e}{4\pi\epsilon_0}\nabla \sum_{j\neq i} \frac{Z_j e \mathbf{r}_{ij}}{\left|\mathbf{r}_{ij}\right|^2}, \tag{3.8}$$

where $\mathbf{r}_{ij}$ is the vector between ions i and j. At each time step, this term is calculated for each ion before applying any forces in order to avoid accumulating error. Modern CPUs have multiple cores, and this feature is exploited to great effect for Coulomb force calculations by parallelizing these calculations across each core using the OpenMP architecture[1]. Even so, the electrostatic calculations remain the primary computational bottleneck.

It is of particular importance for the Coulomb force that the time step is small enough. Since the electrostatic force is very strong for small ion separations, ions that are very close to one another have a tendency to get pushed beyond the geometry of the trap when the time step is too large. This is particularly problematic when dealing with initial conditions and will be discussed in further detail in Section 3.2.2.

3.1.4 Heating effects

Without implementing a heating model, the simplistic laser cooling model of (3.3) would result in cooling well below the Doppler limit for a single ion. Furthermore, as discussed in Section 2.2.2, with only Doppler cooling, real trapped ions typically reach temperatures of several tens of mK, well above the Doppler limit. In order to account for this discrepancy, heating models must be added to increase the ion kinetic energy into the regime where Equation (3.3) remains a fairly accurate description of laser cooling.

Although there are many potential sources of heating in an ion trap (*e.g.*, electric field noise [155] and RF heating [156]), the most relevant for experiments presented in this thesis

[1] http://www.openmp.org/

which involve large, Doppler cooled Coulomb crystals at low q parameters are collisions with background gases since the former heating sources are primarily a concern when using ions in the motional ground state for quantum information experiments. A fairly realistic model of such collisions involves estimating the collision rate between neutral background gases and the ions and applying random momentum kicks to ions consistent with this rate and the mass of the neutral gas molecule. A simple model for the collision rate between ions and neutrals is the Langevin model and is thoroughly discussed in Section 6.2. Typical collision rate constants using this model are of order 10^{-9} cm^3 s^{-1}. Assuming the background gas is at room temperature and at a pressure of 10^{-10} torr, this corresponds to a collision rate of only 0.001 s^{-1} per ion. However, when a collision does occur, the change in ion velocity can be quite large, sometimes in excess of $\Delta v = 100$ m/s for collisions with background N_2 molecules, for example [146]. Because these collisions are both rare and violent, using the Langevin model to reproduce collisional heating effects for a simulation that lasts for only a few ms (compared to experimental exposure times of tens to hundreds of ms or longer) is not the most ideal method. In order to produce a reasonable facsimile of experimental images, the collisional heating model chosen instead applies appropriately small momentum kicks at fixed time steps. The important point is that the overall heating rate of the entire ensemble due to collisions should have a realistic value, not necessarily the frequency and magnitude of momentum kicks caused by collisions. Typical heating rates chosen are a few K/s, with the corresponding kick magnitudes depending on the mass of the ions being simulated and the frequency at which they are applied [146].

3.2 Implementation

Ion MD simulations were implemented in C++ with a front end Python script which sets the initial conditions and simulation parameters and handles plotting and other data processing tasks at the end of each run. Numerical integration is performed using the leapfrog

integration technique due to simplicity of implementation and because it conserves the energy of the system (*i.e.*, it is a symplectic integrator).

3.2.1 Leapfrog integration

The leapfrog integration method can be used to integrate differential equations taking the form

$$\ddot{x} = F(x)/m, \tag{3.9}$$

or as a system of two first order differential equations

$$\left.\begin{aligned} \dot{v} &= \frac{F(x)}{m} \\ \dot{x} &= v \end{aligned}\right\} \tag{3.10}$$

with the dots signifying differentiation with respect to time. Note that strictly speaking, leapfrog integration requires that the force F must only be a function of position. Although the laser force of Equation (3.3) has a dependence on velocity, the magnitude of the force is small enough that any error accumulated by this is negligible.

For a constant time step Δt, the equations to update the position and velocity at time step i are [157]

$$\left.\begin{aligned} x_i &= x_{i-1} + v_{i-1/2}\Delta t \\ a_i &= F(x_i)/m \\ v_{i+1/2} &= v_{i-1/2} + a_i\Delta t. \end{aligned}\right\} \tag{3.11}$$

From these expressions, it is apparent why the integration scheme is named leapfrog: the position and velocity calculations "leapfrog" one another by calculating the position and then the half time step velocity. An equivalent way of writing the integration without explicitly using half time steps is [157]

$$\left.\begin{aligned} x_i &= x_{i-1} + v_{i-1}\Delta t + \frac{1}{2}a_{i-1}\Delta t^2 \\ a_i &= F(x_i)/m \\ v_i &= v_{i-1} + \frac{1}{2}(a_{i-1} + a_i)\Delta t. \end{aligned}\right\} \tag{3.12}$$

Although this version looks quite different, a bit of inspection shows that it is in fact equivalent. In each case, the new positions are calculated using the previous position and velocity with the new acceleration being calculated with the new position. In this implementation, the new velocities are still calculated in a "leapfrog" way by splitting the contributions of the accelerations of the previous and current time step. Since it is somewhat simpler conceptually since it does not require half time step velocities, the second form of Equations (3.12) is used for numerical integration.

Leapfrog integration is a second order method, meaning overall error is of order Δt^2 [158]. This is in contrast to the simplistic Euler method which is first order, but still requires the same number of function evaluations per time step [159]. With a sufficiently small, constant time step, the leapfrog algorithm is stable even under oscillatory motion such as that of a trapped ion. The leapfrog method is also time-reversible and symplectic, meaning that it conserves the energy of the system and is therefore better suited to MD simulations than alternative methods such as Runge-Kutta integration. For further information on the leapfrog method, see Refs. [157, 158, 160].

3.2.2 Initial conditions

Generating proper initial conditions requires some care. In principle, positions and velocities could be initialized randomly using Gaussian distributions. This would be a reasonable model when starting from a thermal, room temperature cloud of ions. However, in practice, this causes problems if not all the ions are laser cooled or the time step is too large. Because of the strength of the Coulomb interaction at short range, if a sympathetically cooled ion is randomly initialized very close to another ion, it will be violently thrown far from the other ions and not be able to rethermalize since the Coulomb force is much weaker for large separations.

In order to overcome this difficulty, initial positions are determined by first finding a minimum potential energy configuration [161, 162]. The simulation is then started with

the positions found through minimization and with zero velocity (*i.e.*, at absolute zero temperature). Heating effects are then introduced in order to bring the ions to a realistic temperature. This method, while not exactly physical, is justified in that laser cooling is modeled as a viscous force with constant damping instead of a more realistic photon recoil model, and is therefore time reversible.

There are a number of well known optimization routines that could be used to find the true potential energy minimum of the system [163]. However, because of the number of evaluations required for computing the potential energy due to the Coulomb interaction, many of these algorithms would require far too long to find the potential minimum for large N. Instead, minimization is performed by first randomly distributing ions and then treating all ions as laser cooled ions for a short period of time with a large damping coefficient β. This allows for rapid thermalization and therefore brings the ions very close to their true minimum energy configuration. One downside to this approach is that it essentially requires running the simulation twice, although initial positions could be cached and used later when repeating simulations under similar conditions.

One further improvement that could be added for finding initial conditions is to use any number of Coulomb force approximations in the initial minimization step. For example, the well-known particle mesh Ewald method is a commonly used approximation for electrostatic interactions in MD simulations and requires $O[N\log(N)]$ evaluations instead of $O(N^2)$ for point to point Coulomb calculations [164]. Multigrid summation or the particle-particle-particle mesh method (P3M) provides an even larger speedup requiring as few as $O(N)$ computations [158, 165, 166]. Alternatively, a nearest neighbor search algorithm, such as k-NN, could be used to only count the electrostatic contribution of ions within a certain radius of each target ion. Any of these methods would take some work to implement, but could also likely be used along with a minimization algorithm to potentially find a more optimal set of initial conditions than by first treating all ions as laser cooled. A final, alternative initialization method implemented in similar MD simulations of large

Coulomb crystals is to first keep a small fraction of core ions fixed in a bcc lattice structure at a theoretically expected density and allow the remaining ions to evolve under Equation (3.1) [167, 168].

3.3 Results

In its present state of development, IonMD is mostly useful for qualitative comparisons with experimental images. Ion trajectories and final positions in three dimensions can be recorded; example trajectories are given in Figure 3.2 and three-dimensional renderings of ion crystals in Figure 3.3. Additionally, CCD images can be simulated in a manner similar to that presented in Ref. [145]. Because images can be simulated with arbitrary resolution, and experimental imaging has finite resolution, the correspondence between simulated and experimental images is never one-to-one. Nevertheless, this offers the ability to visualize the sympathetically cooled, non-fluorescing ions in a Coulomb crystal that would not be visible experimentally. To simulate CCD images, the position of each ion is projected onto an image plane at 45° between the $\hat{\mathbf{x}}$ and $\hat{\mathbf{y}}$ axes at every time step. These coordinates are binned and added to a 2-D pixel array which serves as a simulated CCD. Over the course of the simulation run, this results in an effective density plot representing the probability of finding an ion at any given location. This method does not explicitly take the depth of field of the imaging optics used in the experiment into account, but ions in a larger crystal which are far from the center of the trap are generally more free to move about and so are accordingly more blurred than ions near the center of the crystal. In a simple case, an ion chain consisting of several Ba^+ ions of various isotopes is shown in Figure 3.4. A series of simulated images showing an increasing number of Ba^+ ions for otherwise constant trap parameters is shown in Figure 3.5.

In order to differentiate between ion species, IonMD saves separate simulated CCD data files for each unique m/Z ratio. This allows for visualizing where the various ion species accumulate in the multi-component Coulomb crystal. Simulated CCD images are

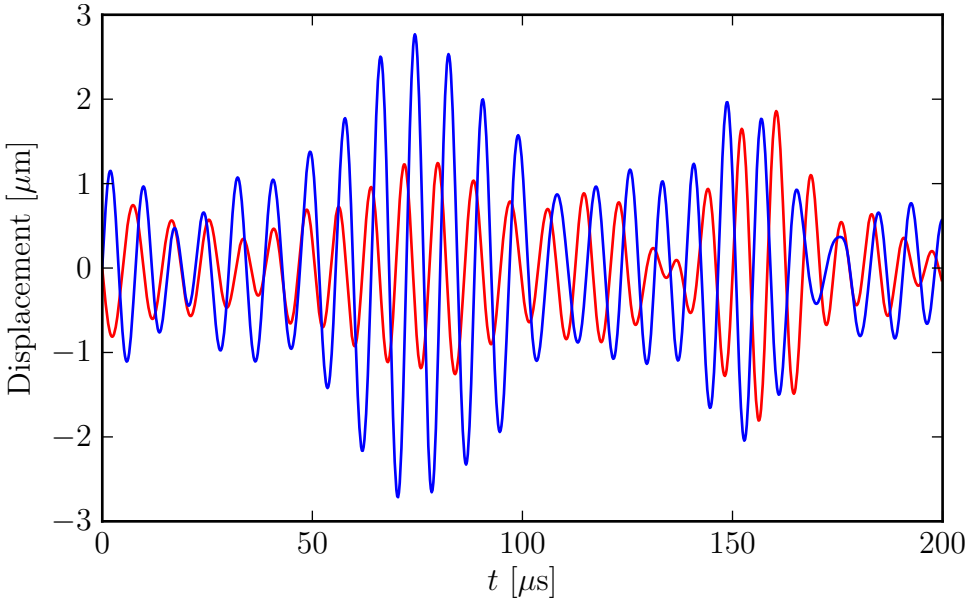

Figure 3.2: Simulated ion trajectories in the x (red) and y directions (blue). Only secular motion is simulated for one ion in a crystal of 14 ions. When many ions are present, trajectories can be quite complicated because of random kicks for modeling of heating and the complex coupling between all ions.

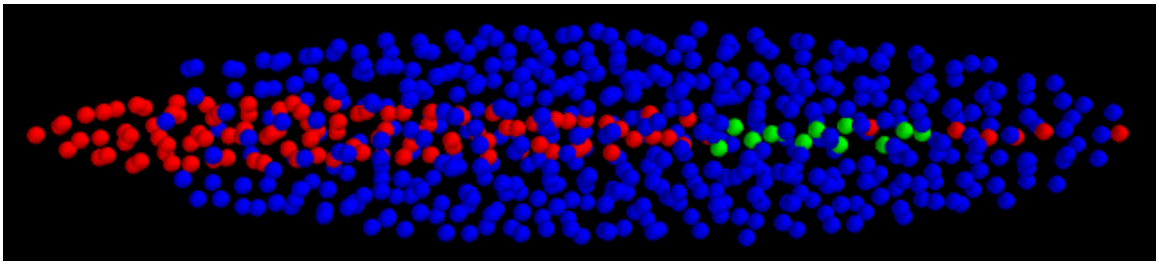

Figure 3.3: 3-D rendering of a simulated ion crystal consisting of $N = 600$ ions. The 108 red particles are laser cooled $^{138}Ba^{+}$ ions, the 12 green particles are sympathetically cooled $^{136}Ba^{+}$ ions, and the remaining 480 ions are sympathetically cooled BaI^{+} molecular ions.

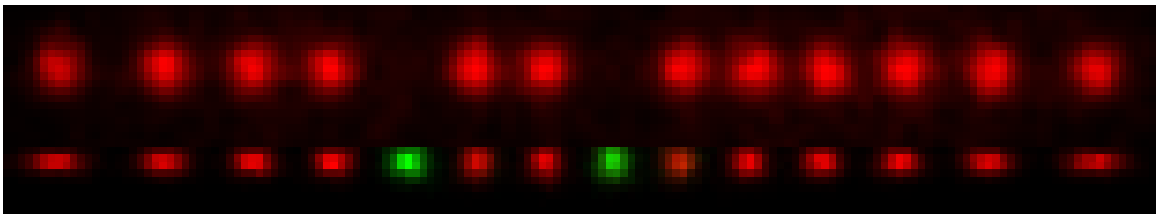

Figure 3.4: Experimental (top) and simulated (bottom) Ba^{+} ion chains. Red colored ions are laser cooled $^{138}Ba^{+}$ ions and the two green colored ions are other isotopes that are sympathetically cooled (not visible in the experimental image).

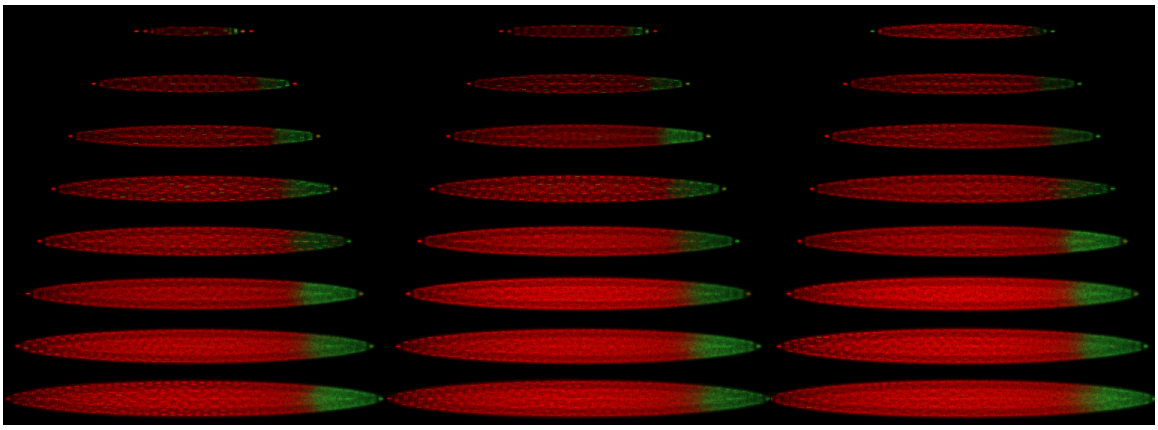

Figure 3.5: Simulated CCD images of increasing numbers of Ba^+ ions. Red indicates $^{138}Ba^+$ ions and green indicates ions of other Ba^+ isotopes. The top left image consists of 25 ions with each subsequent image adding 25 more, ending with 600 ions in the bottom right. In each case, 90% of the total number of ions are laser cooled $^{138}Ba^+$ isotopes with the remaining 10% being the sympathetically cooled Ba^+ isotopes. The cooling laser points to the left.

saved as RGB images with the default color scheme chosen such that the first three unique species are colored red, green, and blue. This choice allows for quickly hiding ion species in external graphics editors by selectively disabling the red, green, or blue color channels. For four or more m/Z ratios, hiding of particular ion species must instead be done by only loading the desired CCD data files when producing the RGB images. Simulated CCD images are useful in estimating proportions of sympathetically cooled ions relative to laser cooled ions (as in Figure 3.6) and can even be used to predict whether or not a particular sympathetic coolant would be cold enough for crystallization. For example, simulations indicate that it should be possible to sympathetically crystallize Th^{3+} ions ($m/Z \approx 77.3$ amu) using laser cooled Ba^+ ($m/Z \approx 138$ amu) ions (see Figure 3.7). This is not particularly surprising given the wide range of m/Z differences that have been shown to be amenable to sympathetic cooling, but such a scheme could potentially be of use in measuring properties of Th^{3+} by simplifying laser stabilization requirements and, more importantly, reducing systematics from gas phase measurements performed with many ions.

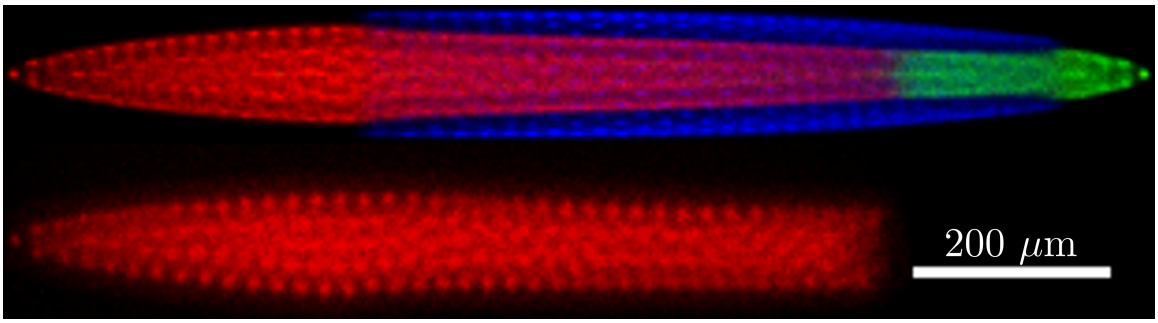

Figure 3.6: Comparison of simulated (top) and experimental (bottom) images containing Ba^+ and $BaCl^+$ ions. In each case, the red colored ions are laser cooled $^{138}Ba^+$ ions, while the green and blue sympathetically cooled ions are respectively $^{136}Ba^+$ and $BaCl^+$ (not visible experimentally). Although the agreement is not exact, such comparisons allow for reasonable estimates on experimental ion numbers. In this case, the simulation contains $N = 1000$ ions, 600 of which are laser cooled, 60 are the non-fluorescing barium isotope, and the remaining 340 are $BaCl^+$ molecular ions.

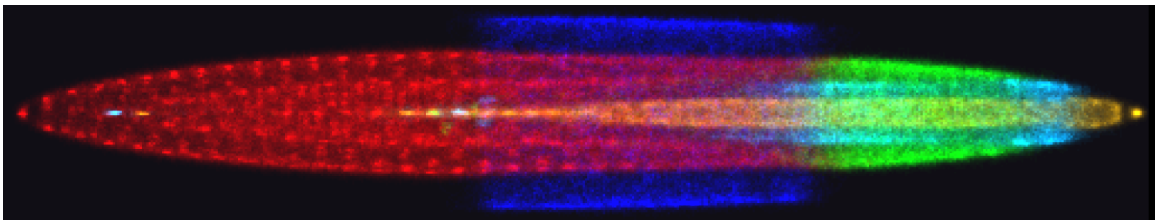

Figure 3.7: Simulated image demonstrating sympathetic cooling of Th^+ (blue), Th^{2+} (cyan), and Th^{3+} (yellow) using laser cooled $^{138}Ba^+$ (red). Green ions are other isotopes of Ba^+ that are not directly laser cooled.

3.4 Summary and future work

Simulations performed with IonMD provide several useful benefits. By comparing simulated images with experimental ones, an approximate number of ions, both laser and sympathetically cooled, can be determined without first needing to perform some sort of fluorescence calibration on a small, countable ion crystal. Furthermore, MD simulations can visualize non-fluorescing ions and therefore aid in the interpretation of experimental images of multi-component Coulomb crystals. In the current implementation, there remains some room for future enhancements. Besides optimizing the minimization routines for generating initial conditions, the simulations could be improved by providing information about the ion temperature. This could allow for determining total simulation run time based on a target temperature instead of the current method of running until a maximum simulation time is reached. Additionally, by comparing simulated images of ions at a known temperature with experimentally acquired CCD images, a reasonable estimate of the effective experimental temperature for both laser cooled and sympathetically cooled ions could be made [145]. By incorporating these improvements, a library of simulated ion crystals could be built for comparing with experimental images under a variety of conditions. By combining this library with a more automated image comparison system, it would become very easy to deduce experimental properties such as ion number and temperature.

Chapter IV

EXPERIMENTAL SETUP

This chapter details the various experimental apparatus that are common to both the Th^{3+} lifetime measurements presented in Chapter 5 and the Ba^{+} reaction studies of Chapter 6. The details of the design and implementation of the linear Paul trap used are given in Section 4.1. Section 4.2 describes the laser setups used and the separate laser locking schemes for each experiment.

4.1 Lifetime trap

Earlier work with Th^{3+} ions employed a trap originally designed by Corey Campbell in the Kuzmich lab [50] and later modified by Layne Churchill to incorporate a channel electron multiplier (CEM) to enhance mass spectrometry capabilities [110]. The trap used for the bulk of the work presented in this thesis, henceforth referred to as the lifetime trap, is similar to the CEM trap and was designed to incorporate parts of the design that proved successful (an overview of this trap is shown in Figure 4.1). Like the CEM trap, it utilizes a linear Paul trap configuration with a large trap radius to allow for the loading of a large number of ions. Primary differences include a longer overall trap length and the absence of a CEM.

The lifetime trap is housed in a Kimball Physics 6" spherical octagon vacuum chamber (part number MCF600-SphOct-F2C8). The RF electrodes are a set of four stock 304L stainless steel tubes of outer diameter 0.25" and wall thickness 0.056 ± 0.005". The tubes were cut by hand to be about 2" in length[1] and were polished using a bench grinder. The tubes slip over ceramic rods of diameter 0.188 ± 0.006". The ceramic rods are supported

[1]The lifetime trap design can easily accommodate different length traps. 2" was chosen so that the length of the trap fills the viewing area of a 6" CF window.

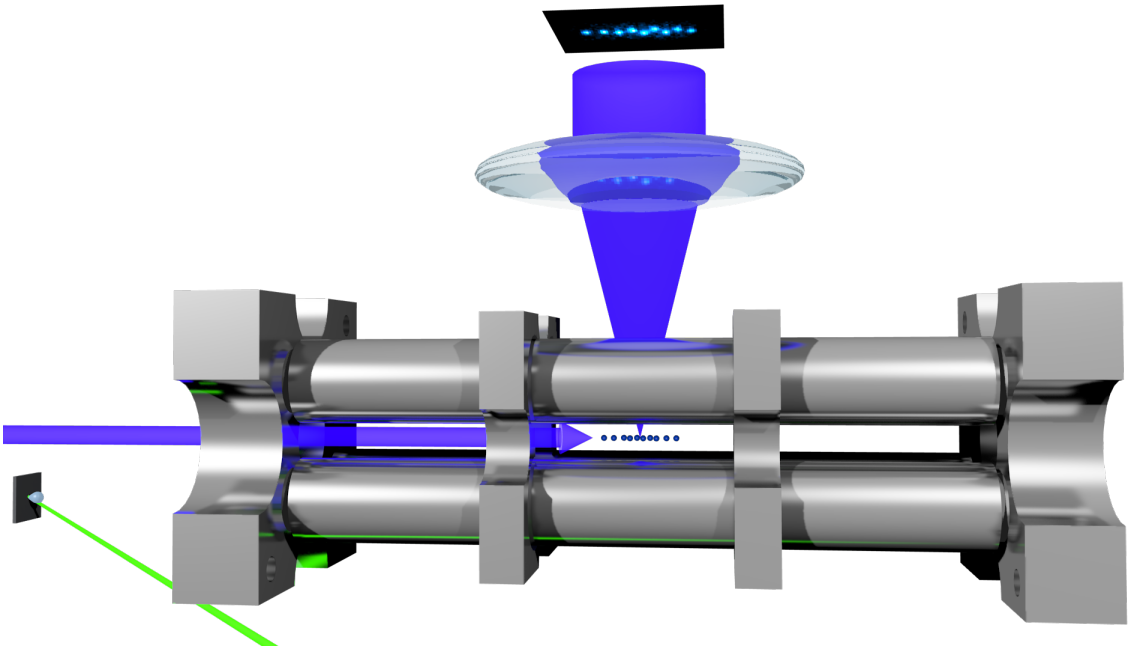

Figure 4.1: Overview of the experimental setup of the ion trap. Ba^{+} or Th^{3+} ions are loaded by ablating a metal Ba or Th target (far left) using a pulsed, frequency-tripled Nd:YAG laser (green, diagonal beam). Light for fluorescence imaging and/or laser cooling is introduced axially (blue beam) and ions are imaged on a EMCCD camera using a NA $\approx$ 0.34 achromatic objective lens.

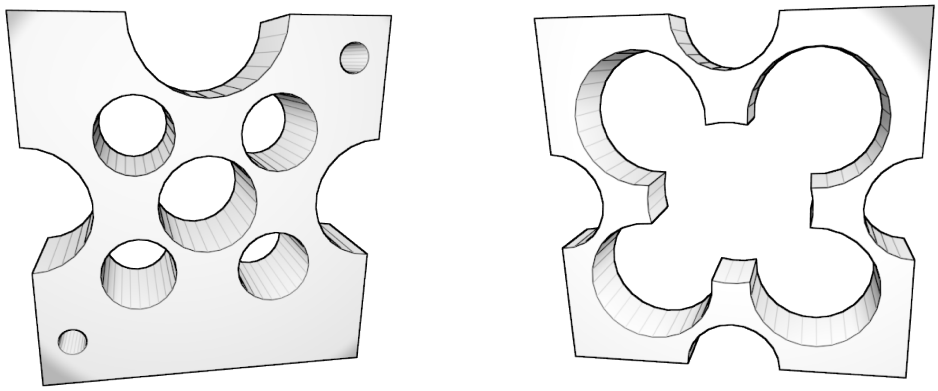

Figure 4.2: Sketches of the two types of machined end cap electrodes used with the trap. (Left) Outer end caps double as a support structure for the ceramic rods on which the RF electrodes rest (four holes surrounding the central hole). The large central hole is for optical access and axial loading of ions. The two smaller holes on the exterior accommodate smaller diameter ceramic rods from which further components could be built off of. (Right) Mickey Mouse end cap. These end caps are designed to slip over the RF electrodes (insulated using polyimide) without introducing significant electrical shielding of the radial confining potential. Part of the electrodes extend into the trap in order to provide tighter axial confinement.

by two custom designed stainless steel end caps (see Figures 4.2 and 4.3b) with the RF tubes positioned such that there is a small gap between them and the outer end caps. Using polyimide tubing and PTFE washers for electrical isolation, the outer end caps are bolted to Kimball Physics C series stainless steel plates, which in turn are attached to Kimball Physics groove grabbers secured to the grooves of opposite 2.75" CF flanges of the spherical octagon. Electrical connections are made by spot welding 0.015" diameter stainless steel wire insulated with polyimide tubing of inner diameter 0.0199" (SmallParts[2] part number SWPT-017-12-*) directly to each electrode. The other end of each wire is then connected to an electrical feedthrough pin by way of BeCu push-on connectors purchased from Accu-Glass Products, Inc.

To provide further axial confinement closer to the center of the trap, two additional end caps are used[3]. Initially, these simply consisted of pairs of stainless steel wire insulated

[2]Now owned by Amazon and known as AmazonSupply.com.

[3]Subsequently, these interior end caps are the ones being referred to unless specified otherwise. While the ceramic-supporting electrodes could be used, in practice they were usually held at ground.

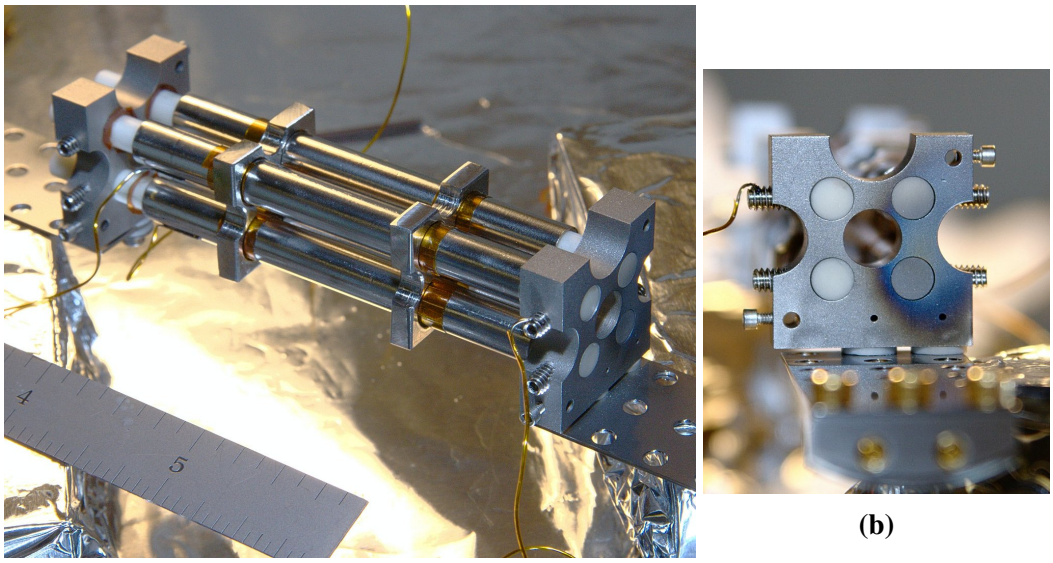

(a) (b)

Figure 4.3: Photographs of the lifetime trap. (a) A full view of the trap in air. The positions of the electrodes are adjusted further after the trap has been placed in the vacuum chamber. (b) A view of the front outer end cap after thousands of ablation events.

with polyimide tubing wrapped around the RF electrodes. However, this resulted in excess ion micromotion which could not be fully compensated for, likely due to asymmetries in their placement. To replace the wire end caps, "Mickey Mouse end caps" (see Figure 4.2) were machined to slide over the RF electrodes and insulated using polyimide tape. Axial confining potentials using these end caps calculated with SIMION are plotted in Figure 4.4. Note that for small Coulomb crystals which only span $\sim$ 1 mm in the axial dimension, the axial potential is harmonic to a good approximation. This approximation is significantly worse as the axial extent increases, however.

To confine ions radially, RF is applied to the stainless steel tubes using one of two different RF power supplies: a commercially available RF power supply (Ardara Technologies PSRF-100) or a home-built RF power supply. The Ardara power supply has two RF outputs with 180° phase difference and can apply separate DC offsets to each output. The precise frequency is dependent on the capacitive load, and since it can handle a load of up to several hundred pF, can be tuned by adjusting the length of leads to the trap RF electrodes or adding additional capacitors. When originally purchased, the power supply

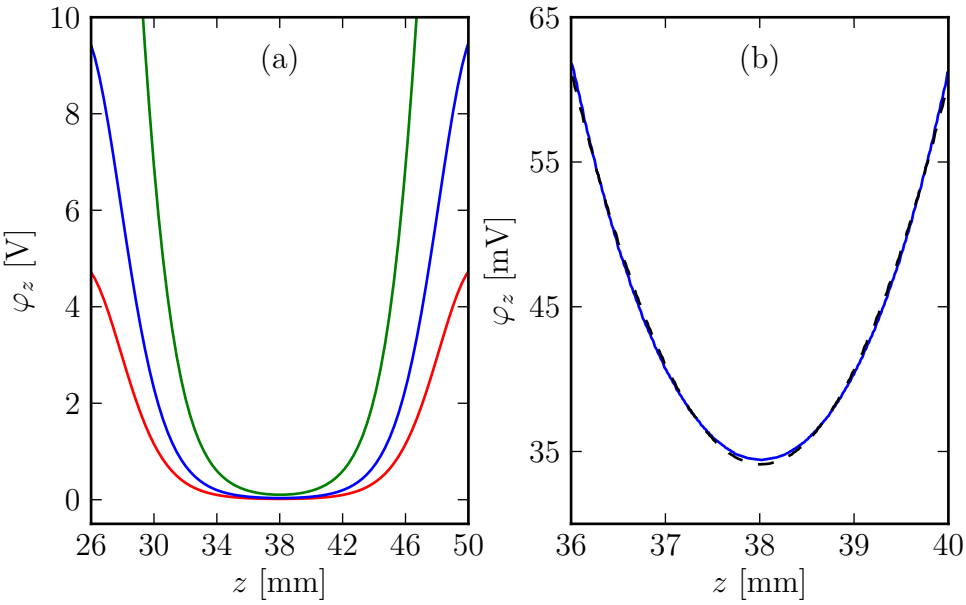

Figure 4.4: SIMION calculations of the axial potential φ_z resulting from the Mickey Mouse end caps. (a) Axial potential with end caps held at voltages 50 V (red), 100 V (blue), and 300 V (green). (b) Near the center of the trap, the axial potential is approximately harmonic (dashed line).

oscillated near 2 MHz under the standard test load of 33 pF. Since then, it has been modified by the manufacturer to oscillate at 3.80 MHz under the same test load in order to allow for a higher RF frequency on the trap, which results in a deeper trap (see Section 2.1.3). The Ardara power supply was ultimately abandoned due to unreliable performance at low RF voltages. Although this likely could have been fixed by the manufacturer, the home-built supply[4] was constructed since it has the advantages of a built-in ability to compensate for excess micromotion, the option to introduce radial secular excitations, and more flexibility in the RF frequency. The home-built supply is a copy of the one presented in full detail in Ref. [50] and so will not be further described here.

The loading procedure is similar to that which is described in Refs. [49, 50, 110]. In short, a target is placed 15 mm from the outer end cap and offset from the trap axis to avoid blocking laser access. The third harmonic (λ = 355 nm) of a pulsed Nd:YAG laser

[4]The home-built supply was originally designed by Corey Campbell and Scott Centers based on the power supply of the Stanford Research Systems Residual Gas Analyzer.

(Continuum MiniLite) is focused to a spot size of $\sim 75\ \mu$m on the target. The trap can be loaded both with buffer gas or in vacuum. The former is most useful for ions which either cannot be laser cooled or ions like Th^{3+} which are inefficiently laser cooled. For buffer gas loading of Th^{3+}, between 10^{-6} and 10^{-5} torr of He at room temperature was used. When all loading parameters are optimized[5], a large quantity of Th^{3+} (along with electrons and other charge states of Th) is produced in the ablation plume, some of which enters the trapping region. At this point, the front end cap voltage is raised from ground to 100–300 V with a rise time of ~ 25 ns. Th^{3+} is then trapped and collisionally cooled by the He buffer gas to a few hundred K (Figure 4.5), along with other ions from the ablation plume that are stable at the loading RF voltage (Figure 4.6). Multiple YAG shots can be used to increase the number of ions trapped provided the end cap timing is optimized. For loading Ba^+ ions without buffer gas, the procedure is largely the same, except that the cooling laser starts red detuned by about 100 MHz. Over a period of several seconds, the detuning is slowly swept up closer to resonance and the Ba^+ ions are able to crystalize (Figure 4.7). Crystallization can be achieved more quickly by operating the trap at low q values where the laser cooling rate is more favorable relative to that of RF heating. The successive loading technique is less reliable without the use of buffer gas, but given the strong fluorescence signal of Ba^+ and the ability to load thousands of Ba^+ ions with a single YAG shot, such a method is unnecessary.

Since ablation produces many ions that are simultaneously stable, it is necessary to remove all undesired ions to increase the fluorescence signal of ion clouds and reduce micromotion-induced heating from non-laser cooled ions. The two methods used here to accomplish this are:

1. *U pulse method*: Adjust V and U such that only a particular ion species is stable.

[5]Loading parameters include, but are probably not limited to: end cap gate timing, ablation laser power, focal length of the final Nd:YAG lens, angle of this focusing lens with respect to the Nd:YAG beam, and, inexplicably, the angle of incidence of the Nd:YAG beam on the target. Loading is optimized by tweaking all of these until maximum fluorescence following ablation is seen.

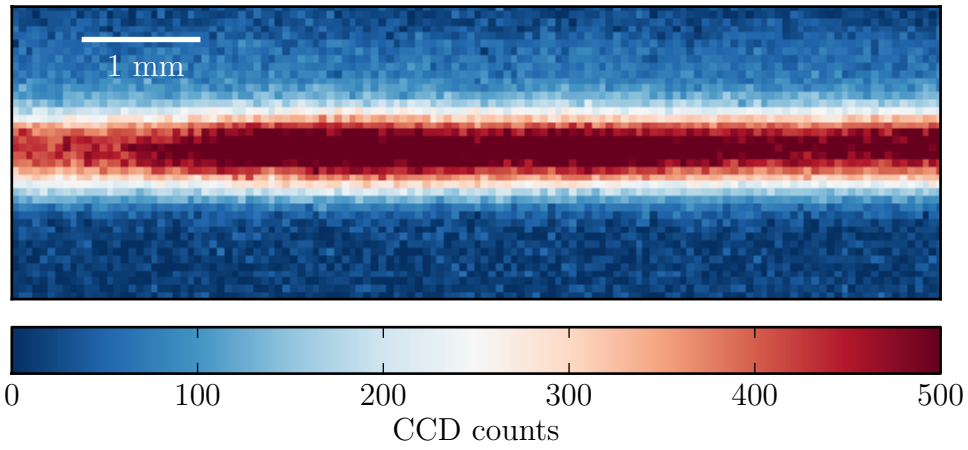

Figure 4.5: A false color fluorescence image captured immediately following an exceptionally good load of Th^{3+} in the presence of $\sim 10^{-5}$ torr He buffer gas. In this 0.5 s exposure, magnification is 0.75×. The cloud of ions extends beyond the edge of the CCD's collection area.

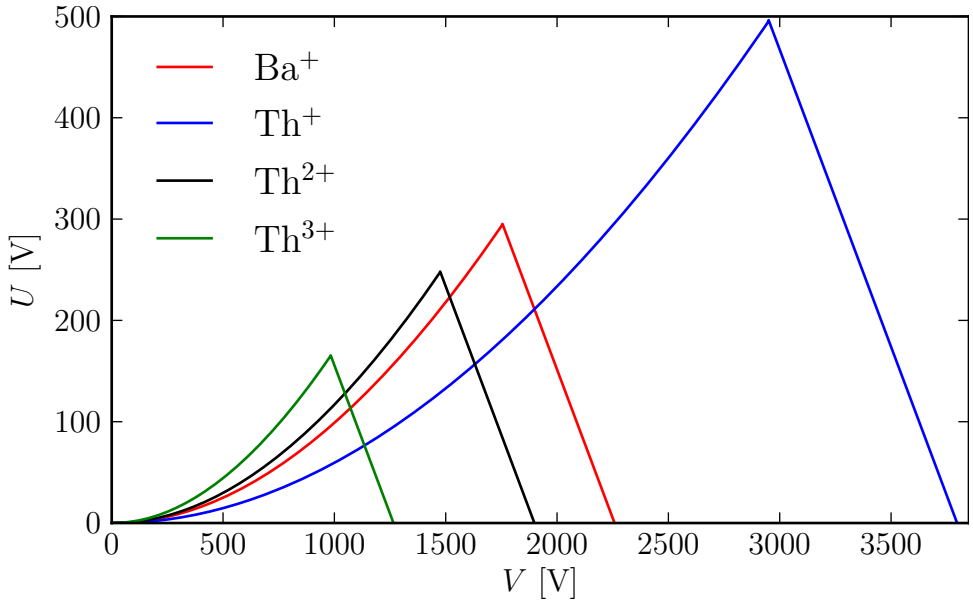

Figure 4.6: Comparison of lifetime trap stability regions for several ions likely to be present following ablation of the Th target. In order to enhance fluorescence of Th^{3+}, it is necessary to eject other trapped ions after loading.

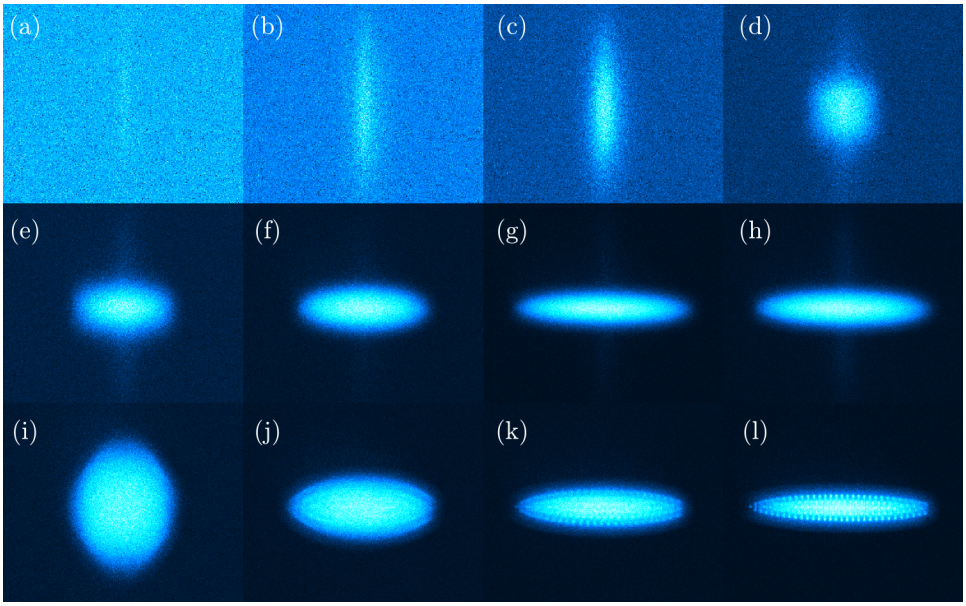

Figure 4.7: A sequence of images showing the process of loading Ba^+ ions and forming a Coulomb crystal without buffer gas. The total time from start to finish is about 10 s. (a) Immediately following ablation, Ba^+ ions begin to fluoresce in response to red detuned light at 493 nm. (b)-(h) Ba^+ ions begin to localize and condense near the trap center as the average temperature decreases. Note the faint ring of still hot ions surrounding the cooler liquid-like core. (i)-(k) The RF voltage is ramped to a very low value and back to its starting value in about 200 ms to eject any heavy contaminants and to allow for more rapid cooling. (l) The Ba^+ ions are now crystallized at a temperature of a few tens of mK.

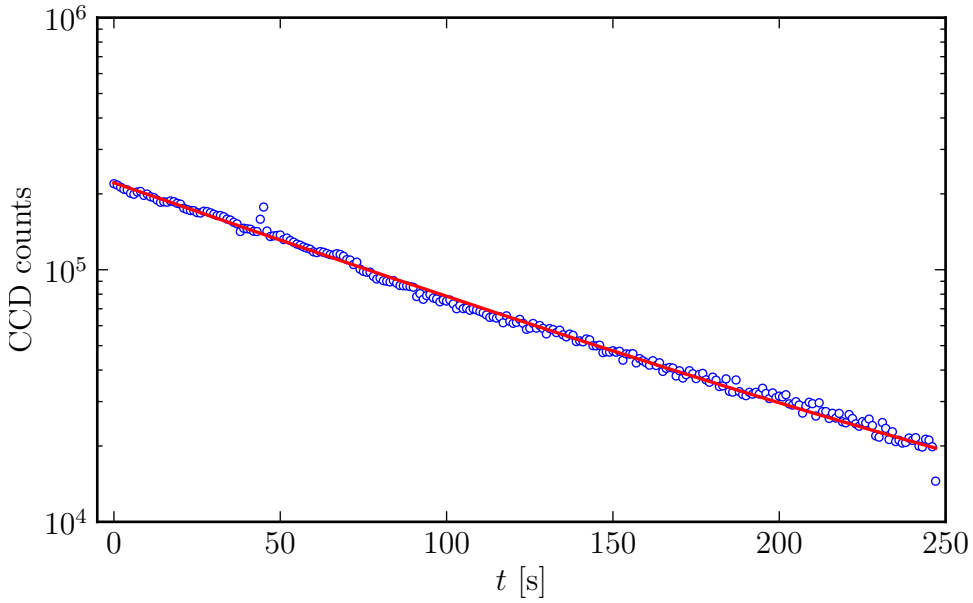

Figure 4.8: A typical measurement of trapped Th^{3+} lifetime in the presence of He buffer gas. Circles are background subtracted fluorescence counts measured on a region of interest of a CCD during a 0.5 s exposure. The line is an exponential fit with $1/e$ lifetime of $\tau = 93 \pm 1$ s.

2. *V ramp method*: Briefly ramp V near the higher and lower edges of the theoretical stability curve for the desired ion to remove effectively lighter and heavier contaminants, respectively.

Each method could in principle work equally well, but in practice, the V ramp method is easiest since then the only high voltage required is that of the RF power supply. For the purposes of mass spectrometry, rather than simply purifying the trap contents, a variation of the U pulse method was developed and is presented in detail in Section 6.3.2.

Although the lifetime trap was originally intended for use with Th^{3+}, a barium target was placed near the thorium target in order to facilitate initial laser alignment and optimization of front end cap timing. Ba^+ fluoresces very brightly at the visible wavelength of 493 nm and unlike Th^{3+}, does not diminish rapidly due to reactions with background gases (see Figure 4.8 and Refs. [83, 110]) making it an ideal ion for testing the trap.

Due to charging and other sources of stray DC voltages, ions can be offset from the RF null at the trap center. Since the RF micromotion amplitude is proportional to the ion

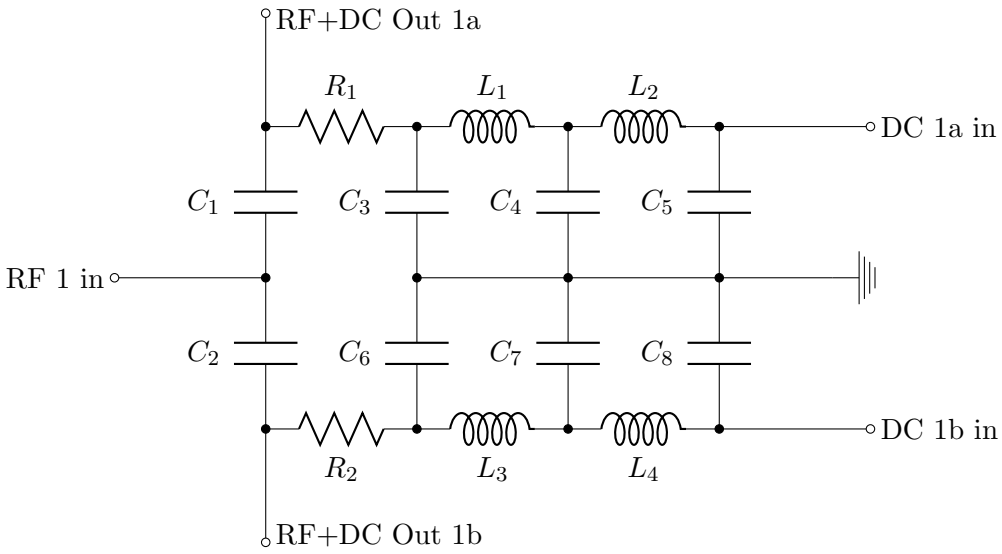

Figure 4.9: Micromotion compensation circuit schematic. This circuit is duplicated so that there is one for each RF output of the Ardara RF power supply.

Table 4.1: List of parts for the micromotion compensation circuit.

Component	Value	Notes
C1, C2	0.01 μF	
C3–C8	1000 pF	AVX P/N 1825WA102KAT1A
R1, R2	1 MΩ	
L1, L3	100 μH	Bourns P/N 6000-101K-RC
L2, L4	8.2 mH	

displacement from the center, this leads to what is known as excess micromotion. For purposes of minimizing this effect, it is common practice to allow for small DC biases to counteract these stray voltages either with additional electrodes or by applying the biases directly to the RF electrodes [169, 170]. Since the Ardara power supply has only two outputs, external circuitry is required in order to add four separate offsets to the RF electrodes. Based on suggestions from Randall Pedder at Ardara, this is accomplished by adding a Π filter network to isolate a DC power supply from the high voltage RF. A schematic for such a circuit is shown in Figure 4.9 along with a component list in Table 4.1. The home-built RF power supply incorporates a similar micromotion compensation circuit.

The procedure for minimizing micromotion is as follows. Start by loading a small number of Ba^+ ions and laser cooling them with appropriate applied RF and end cap voltages to obtain a linear chain or 2-D zig-zag configuration. A small Coulomb crystal is vital as it makes shifts from the small DC biases much more easily observable and because it minimizes intrinsic RF heating since micromotion is largest for ions on the exterior of an ion crystal. Imaging optics should have enough magnification to resolve the individual Ba^+ ions. When stray fields are not well compensated for, the ions will shift from their previous center as the RF voltage is lowered since the confining potential is weaker. By adjusting the compensation voltages at progressively lower RF voltages, the ions can be pushed back to the RF null at the center of the trap, thus minimizing micromotion.

4.2 Optical setup

4.2.1 Laser setup

The simplified level structures for Th^{3+} and Ba^+ are shown in Figure 4.10. With the exception of 493 nm, all wavelengths are directly accessible with external cavity diode lasers (ECDLs). A combination of commercial (Toptica DL-100) and home-built ECDLs were used. To obtain light at 493 nm, a commercial second harmonic generation (SHG) scheme is used (Toptica SHG-100). A laser diode at 986 nm in an ECDL is doubled with a potassium niobate ($KNbO_3$) crystal placed in a bow tie cavity to increase SHG efficiency. As both barium lasers require more effort than a standard ECDL, further details on both the 493 nm and 650 nm lasers are given in Appendix E.

4.2.2 Locking cavities

Many atomic physics experiments using neutral atoms are greatly aided by the ability to directly lock to a spectral line of the atom being probed by using saturated absorption spectroscopy in an atomic vapor cell as a reference. This is of course not generally possible with atomic ions and so several techniques for laser stabilization have been developed for trapped ion experiments. One common technique is to lock to a nearby transition in a

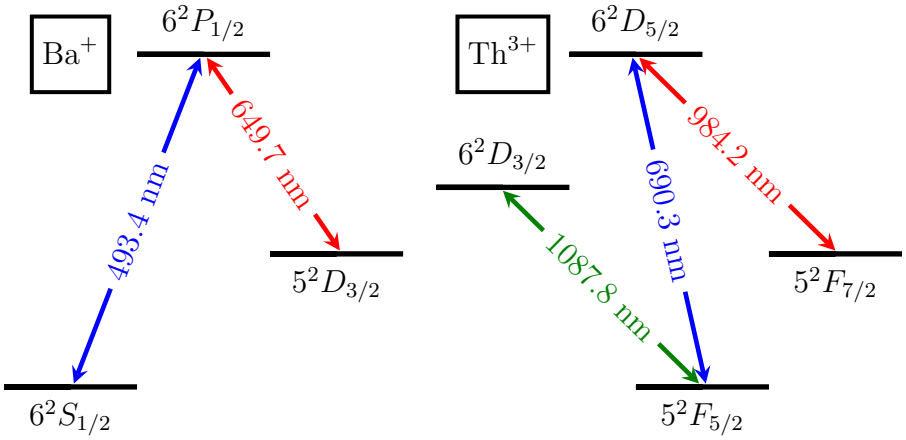

Figure 4.10: Simplified level structure diagrams of Ba^+ (left) and Th^{3+} (right).

molecule such as I_2 in a vapor cell and then shift the laser frequency with an AOM or EOM the required amount to be near resonance with the trapped ions. This method, though, requires a molecule with a spectral feature near enough that of the atomic ion transition to be able to easily shift to. Furthermore, many ions commonly used in trapped ion experiments have three level Λ systems which would generally require using two distinct molecular vapor cells and sets of modulators for appropriately shifting frequencies. Another more recent technique is to monitor the laser frequency with a wavelength meter interfaced with a computer and maintain that frequency using a digital feedback loop. This has the advantages of being largely independent of wavelength and being very easy to setup as everything is controlled in software and does not require any kind of external reference (except for recalibrating the wavelength meter from time to time). It is, however, usually more limited in bandwidth than analog locking techniques, though this is not a major concern with many commonly used ions when only Doppler cooling.

Perhaps the most commonly used laser stabilization technique for trapped ions, and the one employed in this thesis, is the Pound-Drever-Hall transfer lock technique. In this method, a Fabry-Pérot cavity is locked to an externally stabilized reference laser. This laser is often either a frequency stabilized HeNe laser or a ECDL stabilized to a spectral line of atoms or molecules in a vapor cell. Once the cavity is locked to the reference laser, other

lasers are subsequently locked to the cavity. This method has the advantage of providing an exceptionally stable reference often without the necessity of applying large modulation frequencies in order to shift from the cavity resonance to the ion resonance (*c.f.* molecular vapor cells) and is bandwidth limited only by the electronic circuits used for feedback. The primary disadvantage to transfer locks is that the index of refraction of air varies not only with wavelength, but also with temperature, pressure, and humidity [171, 172]. Thus if a pair of laser wavelengths differ by a significant amount, steps must be taken to mitigate drifts from day to day[6]. Common solutions include placing the cavity under vacuum (as in Section 4.2.3) or other constant pressure and temperature environment, or simply actively controlling the temperature (as in Section 4.2.4). Although the relative frequencies can still drift in this latter case, the time scales are long enough to not affect experiments that last for several hours.

Because the photon scattering rate is highly sensitive to laser detuning for laser cooled ions, stabilization of the lasers was vital for the measurements made in the Ba^+ reaction experiments in order to reliably measure relative ion numbers by monitoring fluorescence. Similarly, with the exceptionally narrow linewidths, stabilizing lasers for laser cooling Th^{3+} ions is absolutely necessary, though is less important for Doppler-broadened Th^{3+} ions in buffer gas. Both experiments utilized similar Pound-Drever-Hall transfer lock approaches and are described below.

4.2.3 Thorium locking cavity

In order to lock the three lasers needed for cooling and fluorescing Th^{3+}, a transfer cavity similar to that described in Ref. [51] was constructed. The cavity is locked to a 780 nm reference laser which is itself locked to the $F = 2 \rightarrow F' = (2, 3)$ crossover of ^{87}Rb. The three thorium lasers are then each in turn locked to the cavity as close as possible

[6] Or more frequently when your lab climate control is not very good!

Table 4.2: Calculated thorium cavity parameters. Reflectances listed are from specifications provided by RMI. The two with higher precision were individually listed by the manufacturer, whereas the others were determined from the provided reflectance plot. Free spectral ranges and linewidths are given in MHz.

Laser	Mirror reflectance	FSR	Finesse	Linewidth
690	0.99805	590	1610	0.367
780	0.994	590	522	1.130
984	0.981	590	164	3.604
1088	0.9826	590	179	3.297

to their respective transitions, with necessary frequency shifting performed using acousto-optic modulators (AOMs). A detailed description of the cavity follows.

The cavity mirrors were purchased from Rocky Mountain Instrument Company. They have a radius of curvature of 250 mm and have a broadband dielectric coating that is > 98% reflective for wavelengths between 650 nm and 1100 nm. The mirrors are separated by a 1" length cylindrical piezoelectric element and a 9" length of Invar with a hole bored along its symmetry axis to give a total cavity length of 10". With a rubber O-ring placed behind one mirror, the mirrors and Invar spacer are held in place using aluminum lens tubes and retaining rings. This particular length was chosen in order to give a free spectral range of < 600 MHz to more easily accommodate shifting from the cavity lock points to the transition wavelengths using AOMs which typically only have a bandwidth of $\sim$ 10 MHz on top of the carrier frequency of 100–200 MHz. Table 4.2 lists parameters for the cavity for each wavelength.

In order to combat the aforementioned drifts due to daily changes in the index of refraction of air, the cavity was placed under vacuum. The cavity assembly was put in a vacuum chamber consisting of two standard length 2.75" CF tees and one standard length 2.75" CF nipple. One of the tees has a feedthrough for making connections to the PZT, and the other has a CF to Swagelok adapter with a bellows-sealed valve for pumping out the chamber. The chamber is pumped down to $< 10^{-4}$ torr using a turbomolecular pump and sealed. Even without active pumping, the bellows-sealed valve is sufficient to maintain this

pressure for months.

An overview of the cavity optical setup is given in Fig. 4.11. All four beams are combined using three longpass filters (ThorLabs part numbers FEL1050, FEL0950, and FEL0750[7]). At the output of the cavity, the 690 nm and 780 nm beams are separated from the 984 nm and 1088 nm beams with an 850 nm longpass filter (Edmund Optics part number NT48-560). The transmitted light from the two longer wavelengths are then detected using a single InGaAs detector (ThorLabs PDA10CF). Meanwhile, the 690 nm and 780 nm beams are further split with a 780 nm longpass filter[8] and detected seperately on Si detectors (New Focus model 1801 high speed photoreceivers). To generate error signals, each beam is modulated either by use of an electro-optic phase modulator or by dithering the laser current. Frequencies are chosen such that an optimal error signal is generated and that the 984 nm and 1088 nm signals can be demodulated on a single detector (*i.e.*, one frequency must not be an overtone of the other). Figure 4.12 displays typical cavity transmission signals used for locking the 1088 nm laser which is representative of the signals used for each laser.

4.2.4 Barium locking cavities

For locking the lasers needed for Ba^+ ion laser cooling and fluorescence, a slightly different scheme was used. Instead of placing a cavity in vacuum, a pair of cavities with active temperature stabilization were constructed using the same mirrors as above in a scheme similar to that presented in Ref. [174]. Active termperature stabilization serves two purposes: first, it serves to make the cavity stability better since active stabilization helps mitigate thermal fluctuations. Second, as the index of refraction of air for a given wavelength is most sensitive to temperature [172], holding the temperature constant keeps the relative spacing of

[7] These filters are not designed to be used as dichroics, but they worked well enough for this application. Some mode distortion does occur on the reflected beams which results in a degradation of transverse mode suppression.

[8] At a 45 degree angle of incidence, the cutoff is shifted sufficiently to transmit nearly 100% of the 780 nm beam while still reflecting the 690 nm light.

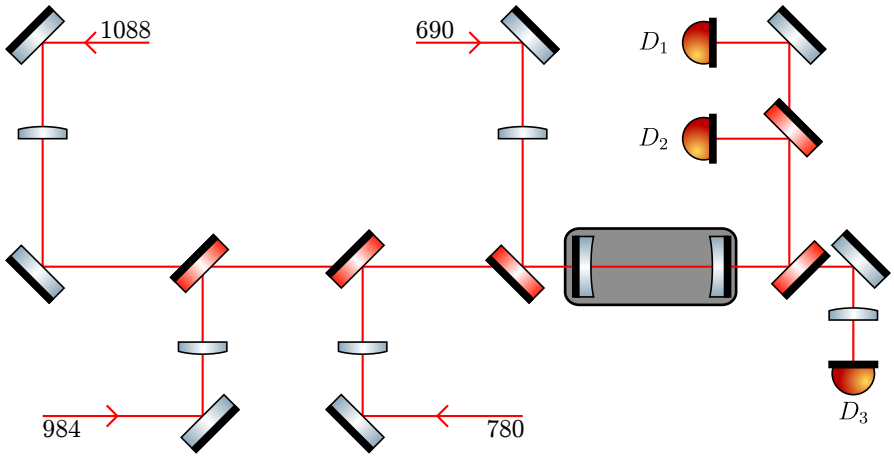

Figure 4.11: Optical setup for the thorium cavity locking scheme. Light from a 780 nm laser locked to the $F = 2 \rightarrow F' = (2, 3)$ crossover is sent through a Fabry-Pérot cavity of length $L \approx 10$" which is under vacuum at $< 10^{-4}$ torr. The cavity is then locked to the 780 nm light using detector D_1 (New Focus model 1801-FS silicon detector). The remaining lasers are subsequently locked to the cavity using detector D_2 (New Focus model 1801-FS) for the 690 nm light and detector D_3 (ThorLabs model PDA10CF InGaAs detector) for the 984 nm and 1088 nm light. See text for further details on the locking scheme. This figure and subsequent optics layout diagrams contain graphics obtained from Ref. [173].

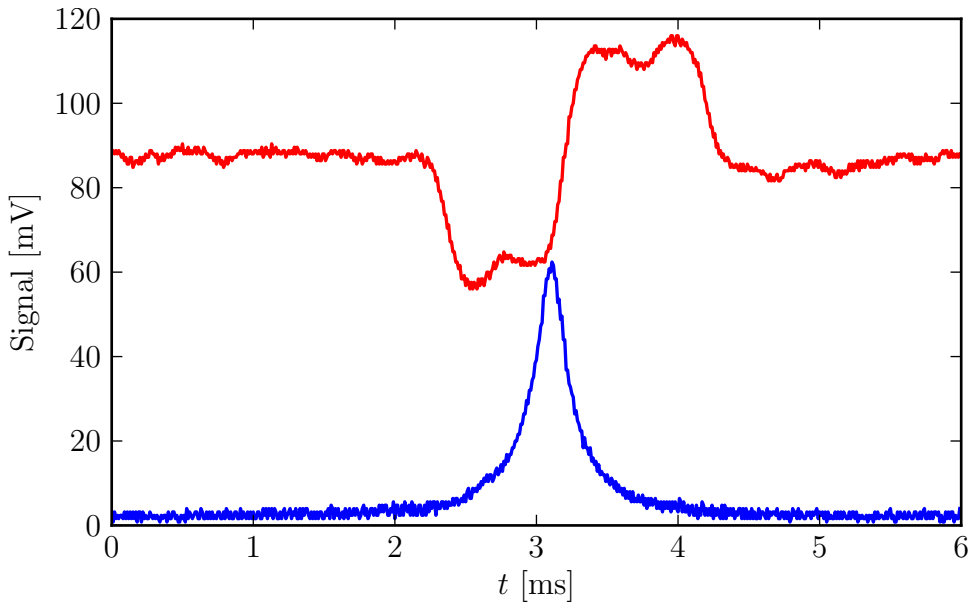

Figure 4.12: A typical cavity transmission signal of the 1088 nm laser (blue) and the generated error signal (red, offset for clarity).

cavity modes for different wavelengths fairly constant. Since separate cavities were used for each barium laser wavelength, instead of choosing a very long cavity length in order to accommodate frequency shifts possible with AOMs for several different wavelengths simultaneously, detunings can be controlled for each laser separately with EOMs or AOMs. Then, in order to find a convenient point such that the TEM_{00} mode for both the reference laser and the unstabilized laser, one needs only adjust the cavity PZT or the cavity temperature to tune its length.

The general optical setup for the Ba^+ laser stabilization scheme is illustrated in Figure 4.13. As with the thorium cavity of the preceding section, the reference laser is a 780 nm laser locked to a transition in Rb, this time locked to the $F = 2 \rightarrow F' = (2, 3)$ crossover[9] in ^{85}Rb. Light from the locked 780 nm laser is split between the two cavities, with the light going to the 650 nm cavity first passing through an EOM to add sidebands large enough to lock to. These sidebands are later shifted in order to change the 650 nm detuning. Meanwhile, a portion of the 986 nm light (the fundamental wavelength used for SHG to produce 493 nm light for Ba^+ ion cooling and fluorescence) similarly passes through an EOM before being coupled into its cavity. For generating error signals, the current of each laser diode is dithered at some unique RF frequency in order to provide sidebands.

Once all beams are optimally coupled into their cavities, the cavity length and EOM modulation frequencies are adjusted in order to overlap transmission peaks used for locking each laser. With transmitted modes well overlapped, the cavities are each locked to their 780 nm reference signal, and the 650 nm and 986 nm lasers are each locked to its respective cavity. Transmission and error signals for the 780 nm/986 nm cavity are shown in Figure 4.14. From time to time, significant changes in the weather, and thus index of refraction, can require a significant adjustment to the cavity length by adjusting the temperature set point such that transmitted modes overlap. However, this rate of change is slow enough

[9]This line was chosen simply because the cavity lengths at the time of initial setup were such that this transition was the most convenient to use rather than separately adjusting each cavity length

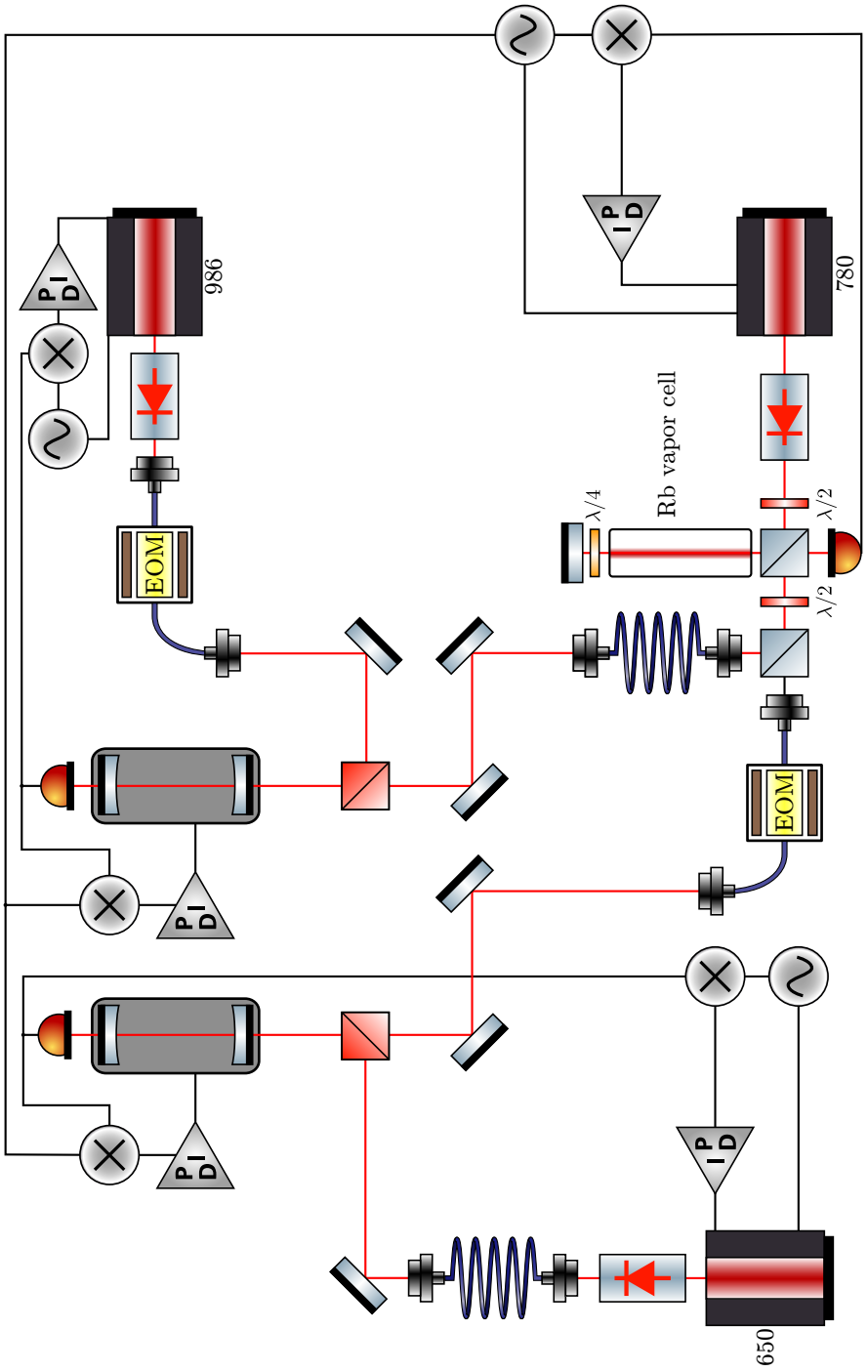

Figure 4.13: Schematic outline of the barium laser stabilization scheme. Two Fabry-Pérot cavities are temperature stabilized and locked to a 780 nm reference laser which is in turn locked to the $F = 2 \rightarrow F' = (2, 3)$ crossover saturated absorption line of ^{85}Rb.

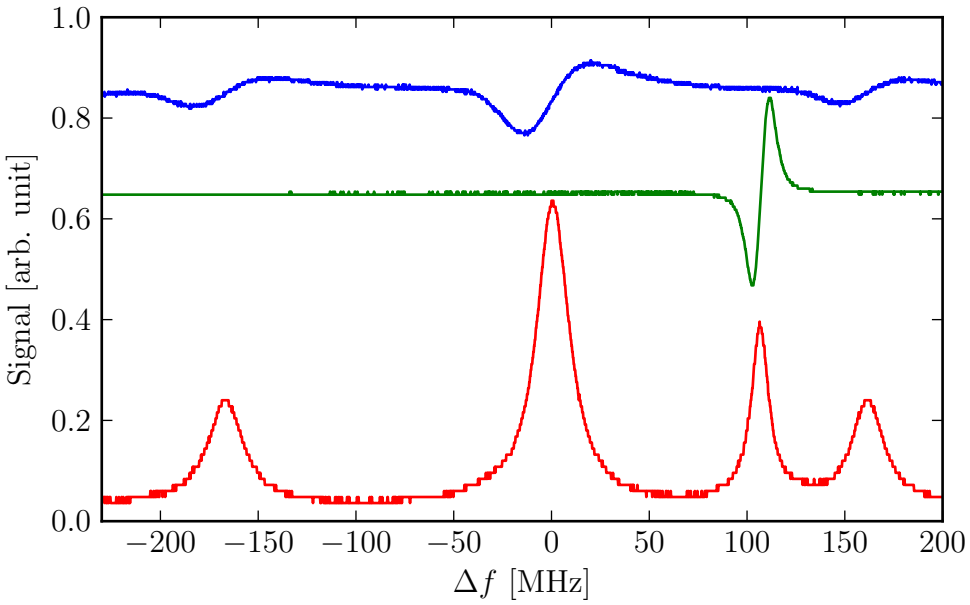

Figure 4.14: Cavity transmission signal of 780 nm and 986 nm light with sidebands at $\Delta f = \pm 161$ MHz produced by modulating the 986 nm light with an EOM phase modulator (DC component from the photodetector in red). With the cavity locked to the error signal from the 780 nm transmitted light (green), the 986 nm laser is locked to one of its sideband error signals (blue). In order to change the detuning of the 493 nm light seen by Ba^+ ions at the trap, the EOM modulation frequency is adjusted. The lock follows this shift provided the shift is performed at a rate low enough for the locking circuit to handle.

that relative laser lock points do not usually shift by more than a few MHz over a period of several hours. Indeed, over the course of a reaction rate measurement experiment presented in Chapter 6, which can last up to half an hour, there is no measurable change in ion fluorescence per ion due to lock point drift.

Chapter V

TH IV LIFETIME MEASUREMENTS

Precision spectroscopic measurements with trapped ions has a long history (see, *e.g.*, Ref. [175]). Earlier studies typically dealt with either ion beams [176,177] or trapped ion clouds in the three-dimensional Paul trap geometry [175, 178, 179]. Modern high precision techniques often instead deal with single trapped ions in order to minimize potential systematic effects [129, 180–182]. Although using a single, laser cooled Th^{3+} ion would be ideal, this approach is much more challenging than with other ions due in large part to the difficulty in laser cooling Th^{3+} ions because of the very narrow cycling transition linewidths of order 100 kHz (*cf.* alkaline earth metal ion linewidths of order 10 MHz). Instead, as a first attempt at measuring electronic lifetimes of Th^{3+}, thermal clouds of ions cooled with buffer gas were used. This of course raises the possibility of a number of systematic effects which must be accounted for. Many questions about these systematics could not be adequately addressed with the experimental apparatus described in Chapter 4, but nevertheless, preliminary results of this investigation are reported here.

This chapter describes measurements of the $6^2D_{5/2}$ excited state lifetime. The Th^{3+} electronic level structure is fairly unique among ions that can be laser cooled in that its ground state is an F level and its excited states are D states rather than the usual $S \leftrightarrow P$ cycling transitions (see Figure 4.10). Furthermore, for the three level Λ system using the 690 nm and 984 nm lasers, the branching ratio to the metastable $5^2F_{7/2}$ state is favored by about 10:1 over decay back to the ground $5^2F_{5/2}$ state [183]. For these reasons, the study of the Th^{3+} electronic levels is of interest to theorists looking to improve *ab initio* calculation methods [53]. The general scheme to measure the lifetime is to first populate the level and then measure fluorescence as ions decay back to the $5^2F_{5/2}$ ground state. Section 5.1

describes this experiment. Due to inconsistencies in being able to load Th^{3+}, only the $6^2D_{5/2}$ state lifetime was able to be measured. In Section 5.2, possible sources of systematic error are discussed. Despite the somewhat preliminary nature of the measurement, the average over many trials was found to be in agreement with theoretical predictions [53, 184].

5.1 $6^2D_{5/2}$ lifetime measurement

In order to measure the decay of ions from the $6^2D_{5/2}$ excited state, ions must first be pumped into the excited state. Then, with excitation lasers shut off, a fast photodetector, such as an avalanche photodiode (APD), can resolve the time at which photons arrive. After many experimental cycles, enough data is accumulated in order to perform a nonlinear least squares fit of the data to an exponential decay curve. The general progress of this data acquisition is illustrated in the simulated data collection shown in Figure 5.1. This simulation shows the arrival times of emitted photons from a single Th^{3+} ion with an increasing number of experimental cycles. In this simplified model, every emitted photon is detected (*i.e.*, unit collection efficiency is assumed) with no background or dark counts and the atom is modeled as a two level system. Nevertheless, by factoring in an estimate of the collection efficiency and the branching ratio to the ground state, this model can be used to make a rough estimate of the amount of time required to achieve a desired statistical uncertainty of the fit.

In this case, to obtain a 1% statistical uncertainty, 10,000 decay periods of 3 μs are required. Since the ion must first be pumped into the excited state, this time must be doubled giving the required observation time in the case of collecting every photon emitted as $T_{\text{coll},0} = 60$ ms. As silicon APDs are much more efficient at visible wavelengths, it is more advantageous to measure 690 nm photons than 984 nm photons (see Appendix F). Using the branching ratio b_{21} for the 690 nm transition and assuming an overall collection efficiency[1] of $\eta_{\text{coll}} = 0.01$ gives a total collection time of $T_{\text{coll}} = T_{\text{coll},0} \cdot \eta_{\text{coll}}^{-1} \cdot b_{21} \approx 1$ hour.

[1] Overall collection efficiency includes numerical aperture, solid angle, fiber coupling efficiency, APD

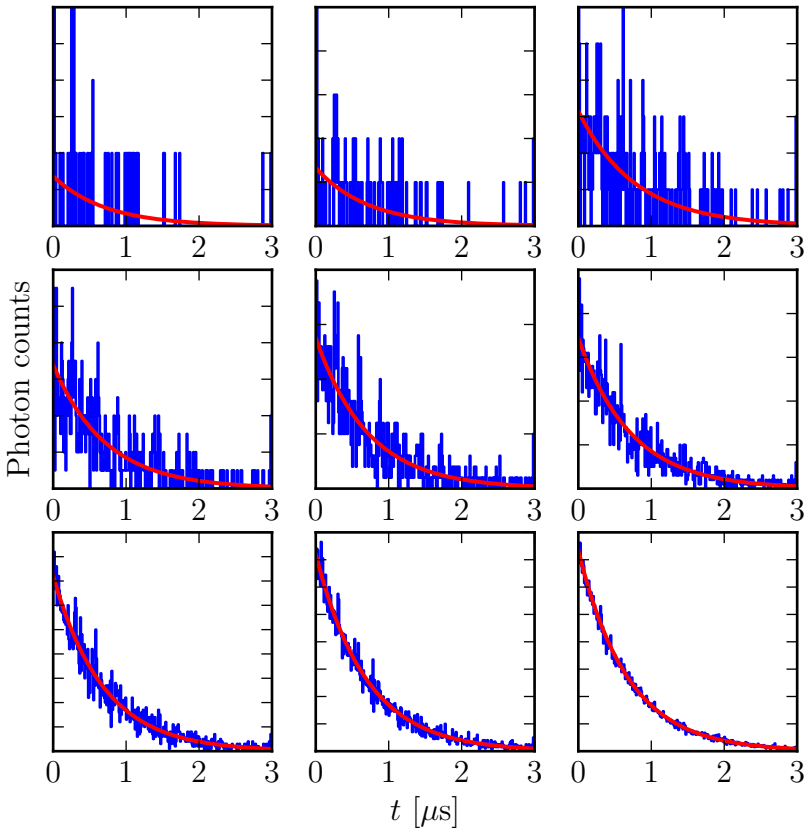

Figure 5.1: Simulated measurement of the $6^2D_{5/2}$ state lifetime measurement. In this simplified example, every emitted photon is detected (*i.e.*, unit collection efficiency is assumed) with no background or dark counts and the decay model considers only a two level atom. Nevertheless, by factoring in an estimate of the collection efficiency and the branching ratio, this model can be used to determine to first order the amount of time required to achieve a desired statistical uncertainty of the nonlinear least squares exponential fit (red curves). Each measurement (blue steps) has an increasing number of data accumulation sweeps, starting with 50 and ending with 50,000.

This estimate still neglects background light levels and APD dark counts, but it is the same order of magnitude as usual experimental observation times for achieving similar statistical error.

The measurement of the $6^2D_{5/2}$ state lifetime was conducted in the presence of between 10^{-5} and 10^{-4} torr of helium buffer gas with a minimum purity of 99.9999% (AirGas Built In Purifier Helium). Such high purity is required in order to minimize the loss rate of

quantum efficiency, and accounting for any other losses through optical components. An overall efficiency of 1% under the circumstances is likely somewhat of an overestimate but still realistic.

Th^{3+} due to reactions with impurities introduced along with the buffer gas [83]. Even with background pressures of $< 5 \times 10^{-11}$ torr, the Th^{3+} trap lifetime is limited to only a few minutes (see Figure 4.8), which is insufficient for accumulating enough statistics for a good fit. As a result, ions were loaded and data was acquired for one to two minutes before pausing data collection, reloading, and then resuming data acquisition.

Using an AOM on each beam, 690 nm and 984 nm beams illuminate the Th^{3+} ions along the trap axis for fluorescence and state preparation. By introducing the AOM modulation frequency through a fast RF switch, this allows for shuttering each beam very rapidly with a fall time of a few tens of ns (see Figure 5.2). To initially populate the excited $6^2D_{5/2}$ state, the AOMs are operated in the open state for several μs. Meanwhile, the APD gate is set to the TTL low position, which prevents it from counting any photons during this optical pumping period. Upon completion of this period, the AOMs are turned off, extinguishing the light at the trap, the APD gate is opened, and a TTL start signal is given to a FAST ComTec P7888 multichannel scaler (MCS or multiscaler) in order to begin counting photon arrival times (a schematic view of this timing sequence is shown in Figure 5.3). TTL signals for RF switches, gating, and MCS are provided by a Stanford Research Systems DG645 digital delay generator.

Fluorescence is collected from ions using a NA ≈ 0.34 achromatic objective lens with focal length $f = 75$ mm oriented transverse to the trap axis. A dichroic separates the 690 nm and 984 nm emitted photons. An Andor iXon DV887 back-illuminated electron-multiplying CCD camera collects the light at 984 nm for optimization of loading parameters and for monitoring the remaining amount of Th^{3+}. 690 nm light is fiber coupled into a 1 mm diameter core multimode fiber (ThorLabs type FT1000EMT) which terminates at the single photon counting module (SPCM) APD (Perkin-Elmer SPCM-AQR-13-FC) with a measured quantum efficiency at 690 nm of around 60%. Gated output from the APD is filtered through a Stanford Research Systems SR400 single photon counter which serves as a discriminator to set the threshold at which to count a detection event. The output of the

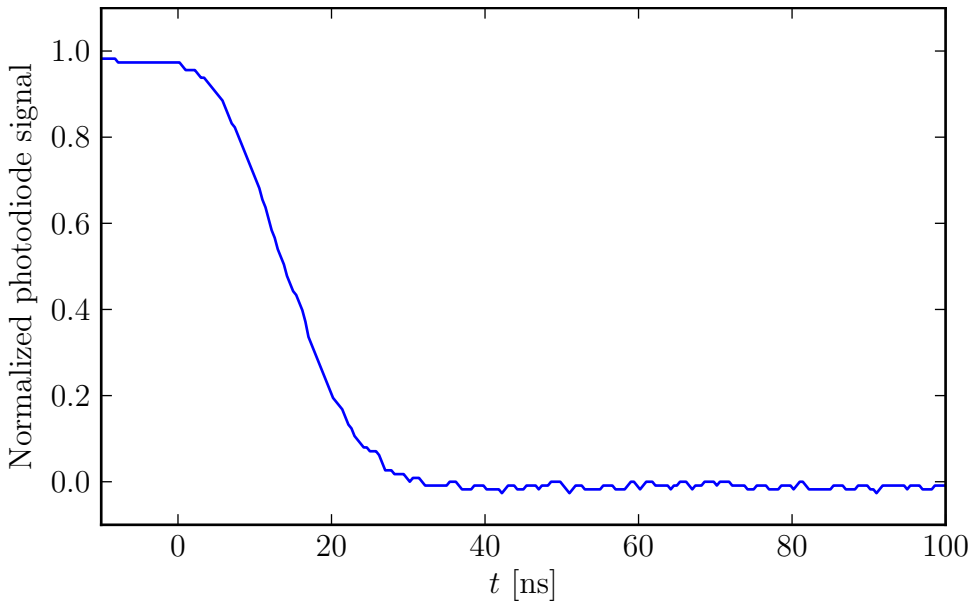

Figure 5.2: Photodiode signal of the 984 nm laser shuttering. At $t = 0$, a trigger is sent to an RF switch which turns off the RF modulation frequency to the AOM which serves as a high speed optical shutter. Here, the fall time for complete turn-off of the beam at the experimental chamber is 36 ns.

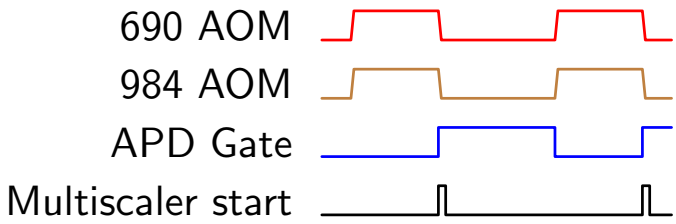

Figure 5.3: Timing diagram for measuring the $6^2D_{5/2}$ excited state lifetime (not to scale). 690 nm and 984 nm light illuminate the trapped Th^{3+} ions to populate the $6^2D_{5/2}$ state and then are turned off in a few tens of ns. At around the same time, gating electronics allow for APD counts to be collected and a start trigger is sent to the multiscaler.

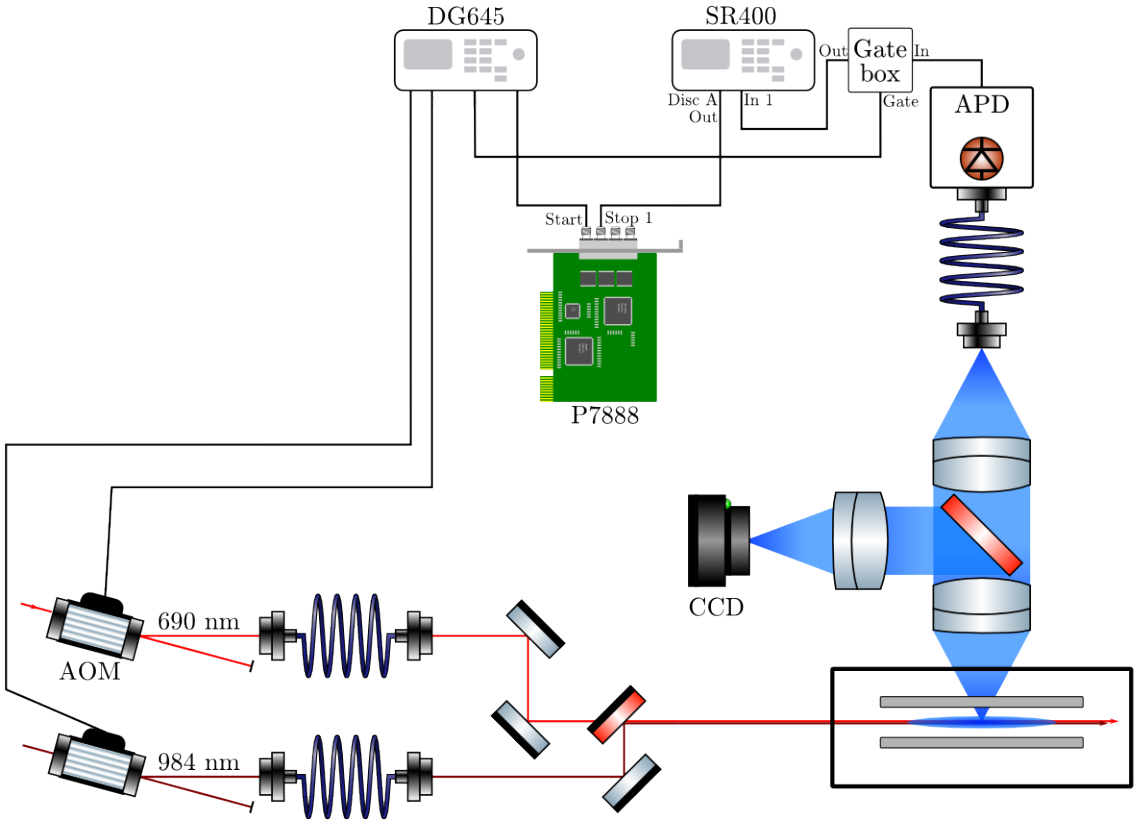

Figure 5.4: Overview of the experimental setup for measuring the Th^{3+} $6^2D_{5/2}$ state lifetime. To populate the $6^2D_{5/2}$ state, the 690 nm and 984 nm beams pass through AOMs which serve as fast optical switches. A digital delay generator controls how long the illumination remains before switching off the AOM. Fluorescence from ions in the presence of He buffer gas is collected by a CCD (984 nm light) and a single photon counting module APD (690 nm light). The APD signal is filtered through a gate box and discriminator before being converted to an arrival time using a MCS.

discriminator is then wired to the `STOP1` input of the MCS which bins the photon arrival time. An overview of the experimental setup is given in Figure 5.4.

In order to eliminate some systematics, fits are made to background subtracted data. The background is collected in the same manner as the data but with no ions in the trap or buffer gas in the chamber. Background acquisition is performed for a period of time that lasts at least as long as the total data acquisition time. Since it is never a perfect match, the background counts are multiplied by a scaling factor before subtracting from the raw data. The scaling factor is chosen such that the mean value of the last N points of the background

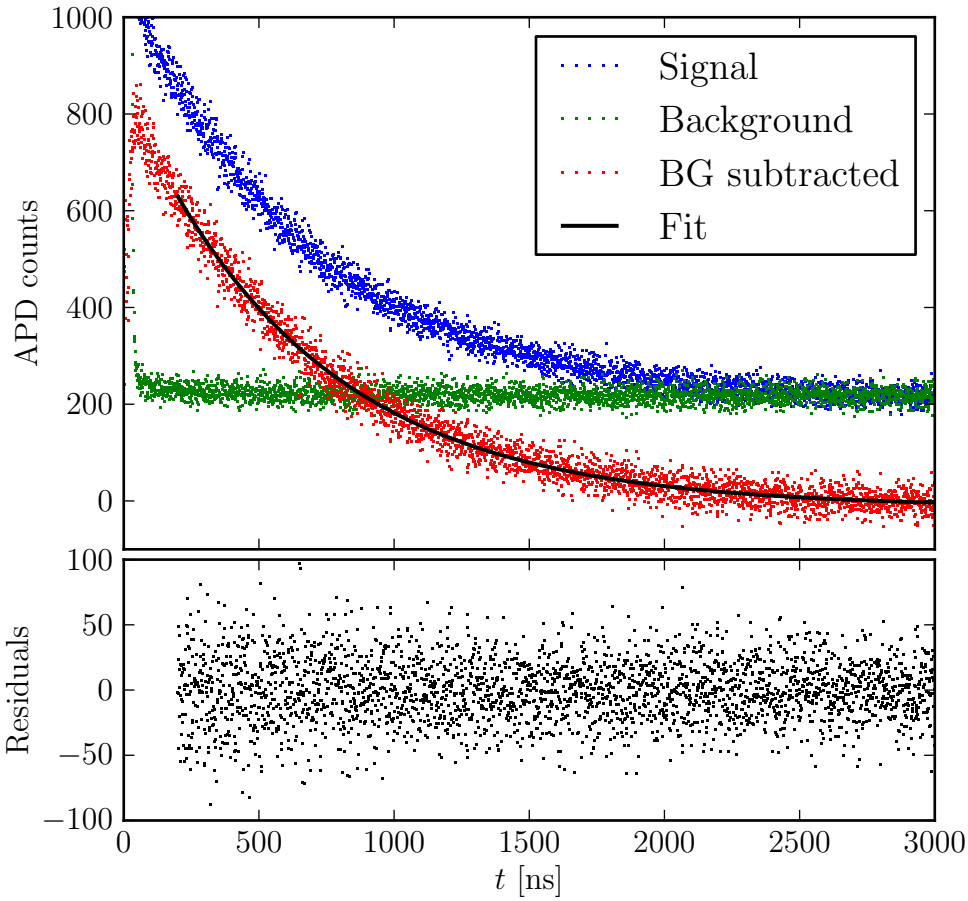

Figure 5.5: A typical $6^2D_{5/2}$ lifetime measurement. Accumulated photon counts with lasers shuttering and no ions present (green) is subtracted (red) from raw data (blue) with ions present for fitting (black line). He pressure in this measurement was 1.8×10^{-5} torr and the fit indicates a lifetime of $\tau = 672 \pm 5$ ns.

match that of the data. A nonlinear least squares fit to the background subtracted data is performed on the data starting at $t = 150$ ns until the end of the acquisition period ($t = 3\mu$s) in order to eliminate stray counts from the incomplete turnoff of the excitation beams. A typical measurement showing the raw data, background, and background subtracted data along with the fit is shown in Figure 5.5.

5.2 Discussion

Performing the measurement of the $6^2D_{5/2}$ state lifetime using many ions in the cloud phase and in the presence of a buffer gas introduces several possible sources of systematic error. In order to eliminate (or at least identify) systematic errors, it was therefore necessary to

Table 5.1: A tabulated list of experimental conditions for the Th^{3+} lifetime measurements of Figure 5.6.

Variable	Comments
He pressure	No measurable effect (see Figure 5.7)
Laser powers	No measurable effect
RF frequency	No measurable effect
End cap voltages	No measurable effect
RF voltage	See text of Section 5.2 and Figure 5.8
Micromotion compensation	See text of Section 5.2 and Figure 5.8

Table 5.2: Summary of theoretical and measured Th^{3+} lifetimes in ns.

State	Theory [184]	Theory [53]	Experiment, this work
$6^2D_{3/2}$	1090.0	1086(89)	—
$6^2D_{5/2}$	676.0	678(46)	679(22)
$5^2F_{7/2}$	1.07×10^9	—	—

conduct measurements of the $6^2D_{5/2}$ state lifetime under a variety of experimental conditions which are listed in Table 5.1. The compiled measurements are all displayed in Figure 5.6 which also compares the mean result with the theoretical predictions of Refs. [53, 184], which are also listed in Table 5.2.

Collisions with buffer gas atoms are well known to have the possibility of influencing observed radiative lifetimes due to collisional quenching and fine structure mixing [178]. The latter effect does not play a role here since there is only one metastable state. Collisional quenching is particularly important when measuring metastable state lifetimes since they are decidedly more long-lived than excited states. It is also conceivable, however, that collisions between buffer gas He atoms and Th^{3+} ions in the excited $6^2D_{5/2}$ state could induce transitions to another state. Such exchanges of energy can be written as [179]

$$Th^{3+}(6^2D_{5/2}) + He \longrightarrow Th^{3+}(5^2F_{5/2}) + He + \Delta E_1 \tag{5.1}$$

$$Th^{3+}(6^2D_{5/2}) + He \longrightarrow Th^{3+}(5^2F_{7/2}) + He + \Delta E_2 \tag{5.2}$$

$$Th^{3+}(6^2D_{5/2}) + He \longrightarrow Th^{3+}(6^2D_{3/2}) + He + \Delta E_3, \tag{5.3}$$

where the internal state of the Th^{3+} ion is given in parentheses and the ΔE_i are the total

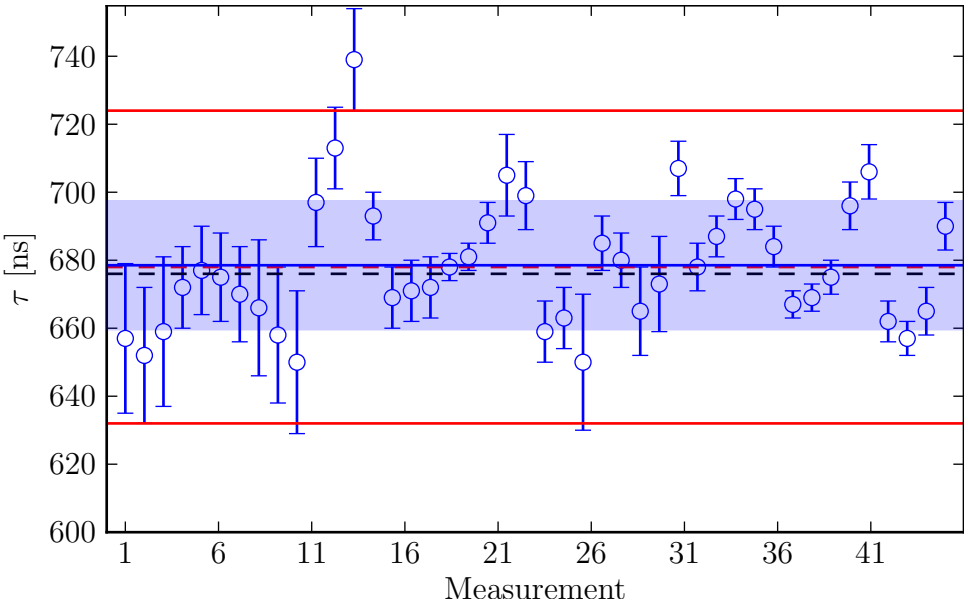

Figure 5.6: Compilation of $6^2D_{5/2}$ lifetime measurements made in buffer gas under various conditions. Error bars on each data point reflect statistical error of the fits. The blue solid line is the mean of all measurements with the standard deviation denoted by the blue shaded region. The black dashed line represents the theoretical value of Ref. [184] while the red dashed line indicates the theoretical value of Ref. [53]. The red solid lines are $\pm 1\sigma$ for the quoted uncertainty of the latter theoretical value. All experimental data points are included in the average and standard deviation calculations.

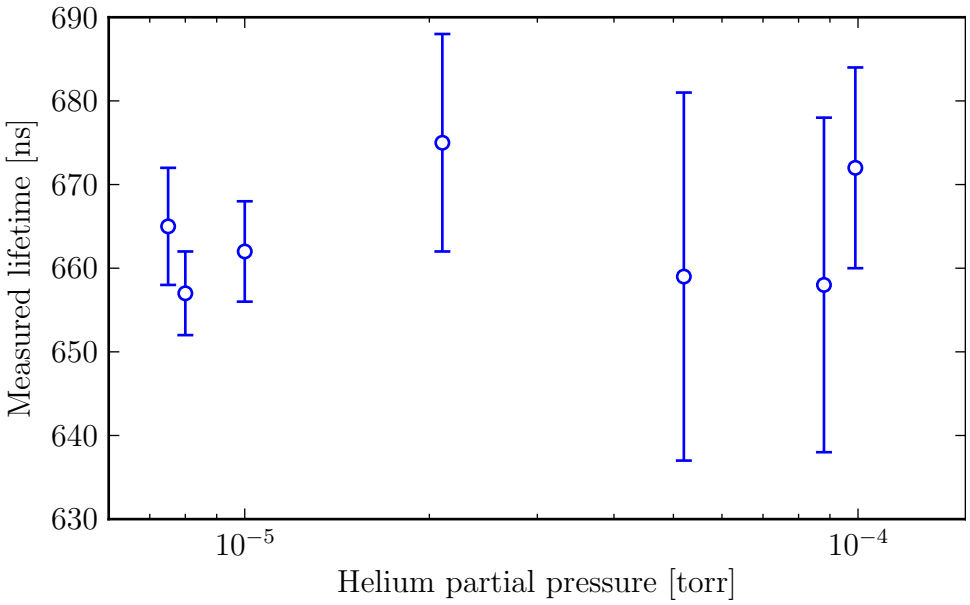

Figure 5.7: Measured $6^2D_{5/2}$ state lifetime versus helium pressure. In each measurement, the peak-to-peak RF voltage is $V \approx 900$ V. No indication of a dependence of the lifetime on pressure was observed. The larger error bars at higher pressures are due simply to shorter data accumulation times and therefore greater statistical uncertainty.

changes in translational energy of the system[2]. Any quenching effect that is present can be measured simply by varying the amount of buffer gas in the system and extrapolating the difference in measurements to zero pressure [185]. Lifetime measurements were performed at different helium partial pressures while keeping other variables constant in order to verify that no systematic effects would arise (see Figure 5.7). Despite the decidedly large statistical error on some of these measurements, there were no indications that pressure variation over about a decade has any effect.

Blackbody radiation might also induce transitions between the excited and ground states which would lead to systematic errors. The blackbody induced deexcitation rate can be written as [186]

$$\Gamma_{bb} = b\frac{2J_2+1}{2J_1+1}A_{21}\frac{1}{\exp(\hbar\omega_{21}/k_BT)-1}, \tag{5.4}$$

where b is the branching ratio for the $2 \rightarrow 1$ transition, A_{21} is the Einstein A coefficient,

[2]If either the buffer gas or ions were molecules, ΔE would also incorporate any change in rotational and vibrational energies.

and J_i is the angular momentum of the atomic state i. For the $6^2D_{5/2} \rightarrow 5^2F_{5/2}$ transition at 690 nm, this works out to be of order 10^{-25} s^{-1}, far less than the actual radiative lifetime and therefore negligible. Even for the $6^2D_{3/2} \rightarrow 5^2F_{5/2}$ transition at the near infrared wavelength of 1088 nm, this rate is still orders of magnitude lower than the quantity to be measured and so of little consequence.

RF micromotion may also play a role in the measured lifetime. Stray voltages, possibly due to patch potentials or charge buildup on insulators, can push ions away from the RF null along the trap axis which contributes to excess micromotion since the micromotion amplitude is proportional to the distance from the trap axis. If not well compensated for, these stray voltages can lead to very large micromotion amplitude at low voltages where trap confinement is weakest. In the first iteration of the trap, polyimide-insulated stainless steel wires wrapped by hand around the RF electrodes were used as inner end caps. The resulting asymmetric geometry made it impossible with the micromotion compensation technique described in Section 4.1 to fully compensate for excess RF micromotion, and thus its presence was noticeable at low voltages. A series of $6^2D_{5/2}$ state lifetime measurements at several RF voltages were made holding all other experimental variables constant (see Figure 5.8). Most systematic effects when measuring lifetimes would lead to a decrease from the true lifetime, but these data clearly show an apparent increase for larger micromotion amplitudes at the lower RF voltages. In the case of a single laser cooled ion, this effect can be attributed to excess heating of the ion [180]. In the experiments presented in this chapter, however, many ions are used and Doppler-broadened to the point where laser light is unlikely to contribute a significant amount of cooling when illuminating the ions, and thus this explanation is lacking. Thus, the precise reason for the effect of the RF voltage on the measured lifetime is not well understood, but was the motivation behind creating the symmetric Mickey Mouse end caps. No further measurements were made, however, because after returning the chamber to ultrahigh vacuum following the end cap

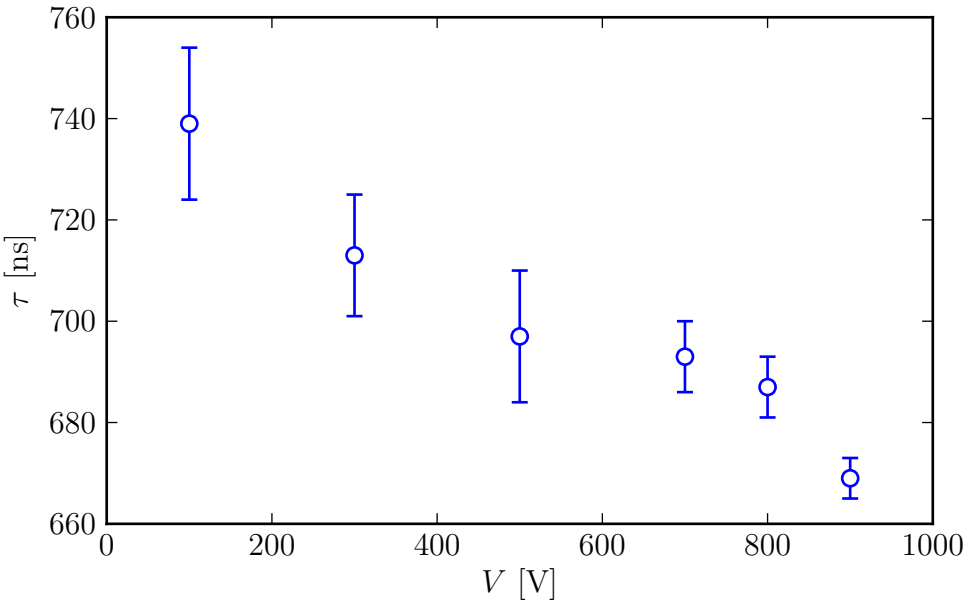

Figure 5.8: Individual measurements of the $6^2D_{5/2}$ state lifetime measurement at several different RF voltages holding all other trap and buffer gas parameters approximately constant. The partial pressure of helium buffer gas for these measurements is around 2×10^{-5} torr. The large variation in the measured lifetimes with RF voltage, coupled with the inability to fully compensate for excess micromotion, implies that the systematic effect is likely related to the RF micromotion amplitude.

installation, Th^{3+} could no longer be loaded for undetermined reasons. Difficulties in loading Th^{3+} have long stalled experiments, and despite prolonged efforts at finding a solution to this problem, one was not found in this instance, and so a different direction was taken for the ion trapping project.

There are a number of other possible sources of systematic error related to using a large number of ions which were not directly tested for here and could be explored in the future once the loading problem is addressed. These include [181]: pulse pileup; radiation trapping in which some ions reabsorb photons emitted by other ions before they can reach the detector; subradiance and superradiance; and transit effects in which ions move in and out of the collection region before decaying. Of these, the last effect is the most likely to be relevant here since the fiber collection mode only covers a small fraction of the ion cloud.

5.3 Conclusion

Despite the preliminary nature of the $6^2D_{5/2}$ state lifetime measurement, results of different measurements were encouragingly consistent for a variety of trap and buffer gas parameters apart from the excess micromotion effects discussed above. Despite these difficulties, these early results are in agreement with the state of the art theoretical predictions. With the addition of measurements of the lifetimes of the $6^2D_{3/2}$ excited state and $5^2F_{7/2}$ metastable state, theoretical models could be further refined. Future experiments can further improve upon the results presented here by performing measurements on laser cooled ions. This would eliminate a number of possible systematic effects discussed in this chapter. Although long integration times would be necessary, the ideal measurement would be to use a single laser cooled (or sympathetically cooled) Th^{3+} ion.

Chapter VI

CHEMICAL REACTIONS WITH TRAPPED BARIUM IONS

6.1 Introduction

In the past several years, there has been a growing interest in the study of molecular ions for their potential applications of extending quantum control to the molecular regime [69, 71], precision measurements [11], and for studying chemistry in the truly quantum regime [187]. The use of laser cooled ions allows for the study of reactions at collisional energies below that of room temperature in the center of mass frame. Even lower temperature collisions can be studied by velocity selection of polar molecules [86], and with the rapid development of techniques for cooling the internal degrees of freedom of molecules [64, 188–190], the study of ion-neutral molecule reactions at the quantum level is now attainable.

Several studies of chemical reactions between laser cooled ions and neutral molecules have been performed over the course of the past decade or so. These include several studies with both Ca^+ [19, 84, 86, 191] and Ba^+ [82] ions. With the exception of the studies of reactions producing CaF^+ and a measurement of production of $BaCl^+$ due to the presence of background HCl present in a vacuum chamber [192], there has been little study of reactions for producing alkaline earth monohalide ions, a promising class of molecules that are amenable to cooling to the rovibrational ground state via collisions with ultracold neutral atoms [93, 94]. Presented in this chapter are experiments for producing barium monohalide ions, BaX^+ (X = F, Cl, Br, I) by using and characterizing reactions between laser cooled Ba^+ ions and neutral molecular reactants. Where possible, reaction rate constants were also measured.

6.2 Classical rate models

The rate τ^{-1} at which a general chemical reaction A + B $\longrightarrow$ C occurs is given by [193]

$$\tau^{-1} = k(T) n_A^{\alpha} n_B^{\beta}, \tag{6.1}$$

where k is the reaction rate constant which is in general a function of temperature, n_A and n_B are the number densities of reactants A and B, and α and β are empirically determined constants which determine the so-called order of the reaction. In the case where the concentration of reactant A (gas phase neutral molecules) overwhelms that of reactant B (trapped and laser cooled atomic ions), such as is the case with the reactions studied here, the reaction is considered to be pseudo-first order. In such a reaction, the ions and neutral molecules react at a rate

$$\tau^{-1} = kn, \tag{6.2}$$

with n being the gas number density. From this expression, k thus has units of volume per unit time and the population of reactant B decays exponentially. Fundamentally, for a reaction event to occur between two isolated reactants, they must collide. Thus, if we assume a unit probability for a reaction event when a collision occurs[1], from dimensional analysis, k may be expressed as

$$k = \sigma v, \tag{6.3}$$

where σ is the collisional cross section and v is the relative velocity between the reactants. The problem of theoretically predicting rate constants is therefore equivalent to calculating cross sections.

The simplest theory describing collisions between ions and neutral molecules in the gas phase is the well-studied Langevin model [194]. It treats the ion as a point particle with charge Ze and considers neutral molecules which do not possess a permanent dipole moment, are spherically symmetric, and have dipole polarizability α. The potential between

[1] For an exothermic reaction (*i.e.*, a reaction which does not require any external input of energy in order to proceed), this is a reasonable assumption.

the ion and neutral molecule then scales like r^{-4} [194], where r is the distance between the centers of mass of the reactants. These assumptions lead to a cross section of[2]

$$\sigma_L = 2\pi \frac{Ze}{v} \sqrt{\frac{\alpha}{\mu}}, \tag{6.4}$$

where μ is the reduced mass. Substituting this expression for the cross section into Equation (6.3) yields the theoretical reaction rate constant

$$k_L = 2\pi Ze \sqrt{\frac{\alpha}{\mu}}, \tag{6.5}$$

which is commonly referred to as the Langevin rate constant in honor of Paul Langevin who originally developed this model of ion-neutral interactions [195]. Typical values of k_L are of order 10^{-9} cm^3 s^{-1}.

There are some limitations to the Langevin model. First, as already mentioned, it does not apply to polar molecules and demands spherical symmetry. Second, it does not accurately predict reaction rates for endothermic reactions since it assumes every collision results in a reaction. It is worth noting, though, that even for endothermic reactions, the internal electronic configuration of the ion (say if laser cooling) can supply enough energy to the system to overcome the potential barrier to reaction, in which case the rate is dependent on the fractional population in excited states, and so a measured reaction rate is highly dependent on laser detunings and intensities. Despite these shortcomings, the Langevin model remains a useful tool for estimating reaction rate constants and many reactions do indeed adhere closely to its predictions.

For molecules with a permanent dipole moment of magnitude d, the leading term in the interaction potential scales like $r^{-2}\cos(\theta)$, where θ is the angle between the dipole and the line connecting the centers of mass of the reactants, instead of r^{-4}. The Langevin model can be extended for this case by adding an additional term [196]

$$k_D = 2\pi Zed \sqrt{\frac{2}{\pi \mu k_B T}}. \tag{6.6}$$

[2] In the subsequent discussion of rate constants, Gaussian-cgs units are used as they are what is most commonly found in the literature.

This expression for k_D presumes that the dipole is "locked in" to the point charge (*i.e.*, $\theta \equiv 0$). In reality, the dipole has some finite probability of pointing towards the charge, and so k_D is given a nonnegative prefactor $c \leq 1$ to account for the dipole orientation probability distribution. The total reaction rate constant between a charged point particle and a polar molecule can then be expressed as

$$k = k_L + ck_D. \tag{6.7}$$

To lowest order, by setting $c = 1$, this expression can be used to obtain an upper bound estimate of the rate constant.

A somewhat more sophisticated approach is to estimate k by considering the average dipole orientation (ADO) model [197]. In this model, the polar molecule is treated as a rigid rotor in order to obtain $\bar{\theta}(r)$, the average value of θ, which is then used to compute an average cross section for predicting the rate constant. Even with the relatively simple assumptions of the ADO model, determining the rate constant in this manner requires several fairly complicated numerical integration steps. The ADO model can be further improved by explicitly considering conservation of angular momentum [198]. Other methods for predicting ion-polar molecule rate constants involve using a variational [199] or quantum scattering [200, 201] approach. In all cases, the dynamics are much more complicated than the simple Langevin model and may or may not provide accurate predictions depending on the specifics of a given reaction. As such, when applicable here, the simple approach of setting $c = 1$ to obtain an upper bound estimate is used.

6.3 Product mass determination

A number of techniques exist for determining the masses confined in an ion trap [202–206]. When a laser cooled species is present, nondestructive mass detection can be performed by supplying an AC voltage whose frequency is swept through all possible secular resonances for each ion species potentially trapped. When an ion is near resonance with the applied AC frequency, its increased kinetic energy in response to the AC field causes it to heat,

and through the mutual Coulomb repulsion leads to heating of all other trapped ions. This heating in turn results in a change in fluorescence of the laser cooled ions which can be used to detect the presence of sympathetically cooled species. Section 6.3.1 describes this method in detail.

Additionally, there are several destructive techniques for determining trapped masses [8, 83, 192, 207]. As discussed in Chapter 2, the Mathieu stability parameters depend on the mass to charge ratio, and therefore a Paul trap can be operated such that only a certain range of masses are stable. Traditionally, destructive mass spectroscopic techniques require the use of a charge sensitive detector such as a channel electron multiplier (CEM) or Faraday cup. Because the chamber for the Ba^+ reaction experiments was not equipped with any such detector, a new technique was developed to exploit the properties of Coulomb crystals for identifying heavier product masses. This technique is described in Section 6.3.2.

6.3.1 Nondestructive mass determination

Recall from Section 2.1.3 that for a single ion, the radial secular frequency for $U = 0$ is given by $\omega_r = (\omega_0^2 - \omega_z^2/2)^{1/2}$ where $\omega_0 = ZeV/(\sqrt{2}mr_0^2\Omega)$ and $\omega_z = [2Ze\kappa U_{EC}/(mz_0^2)]^{1/2}$. Because of the inverse dependence on mass in both ω_0 and ω_z, each ion species has a different resonant frequency and so a supplied AC voltage in principle allows for the differentiation of different masses. Unfortunately, the presence of many ions introduces shifts in frequencies due to the Coulomb coupling between ions (see Figure 6.1) which can make absolute determination of mass difficult [202]. Additionally, the length of the trap used here makes the axial potential deviate significantly from the harmonic approximation for large ion numbers (see Figure 4.4) which makes the axial frequency respond to a change in end cap voltage differently than with a single ion present (see Figure 6.2). In the case of precisely two localized ions, the modes of oscillation in the axial direction can be written exactly as [19, 203]

$$\omega_\pm = \left[(1 + M) \pm \sqrt{1 - M + M^2}\right]\omega_z, \tag{6.8}$$

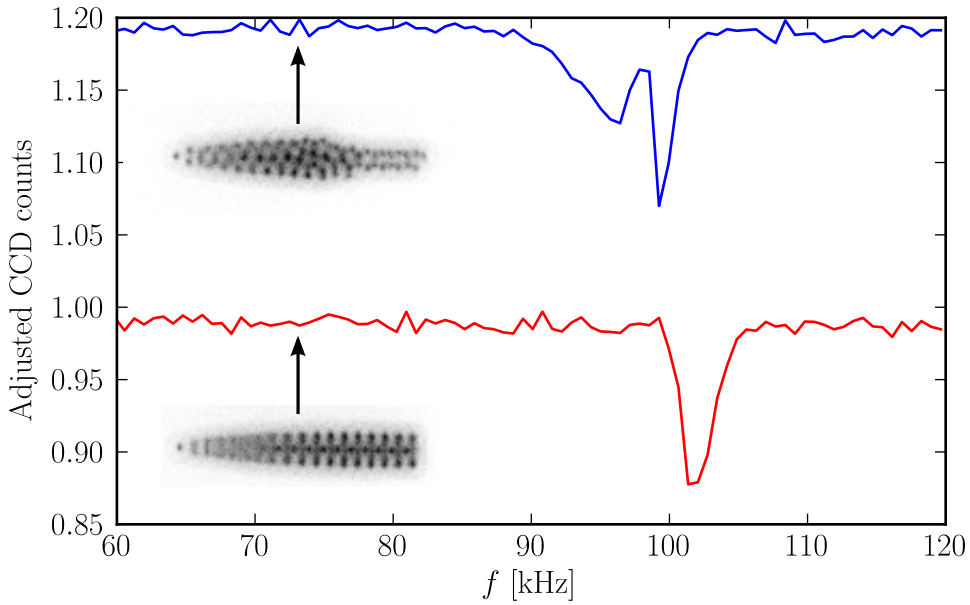

Figure 6.1: Comparison of AC frequency sweeps with (top) and without (bottom) molecular ions. Following an AC frequency sweep, the ion crystal containing molecular ions was purged of ions heaver than Ba^+ by briefly adjusting the trap voltages U and V to values at which ions with a mass to charge ratio of a few amu more than that of $^{138}Ba^+$ are unstable and therefore ejected from the trap. The subsequent AC frequency sweep shows a significant shift in the Ba^+ motional resonance frequency.

where $M = m_1/m_2$ and ω_z corresponds to the single particle frequency of m_1[3]. By detecting fluorescence in phase with the perturbing AC field, it is possible to achieve relative mass resolutions of better than 10^{-4}. This technique, while highly precise and robust, was nonetheless not easily implemented in the experiments presented in this chapter for a number of reasons. First, in order to perform such measurements, it is necessary to be able to repeatedly load only two ions. With the ablative loading technique discussed in Section 4.1, this is simply not practical. Additionally, because ablation is not isotope-selective, it can be difficult to be assured that only two Ba^+ ions have been loaded as there could be some number of other non-fluorescing Ba^+ ions of other isotopes also present.

Instead, radial AC secular sweeps were performed on large Coulomb crystals. Despite the frequency shifts, these measurements are still sufficient to give an estimate of reaction product masses relative to that of laser-cooled Ba^+. The general technique for these types

[3] Additionally, this assumes $Z = 1$.

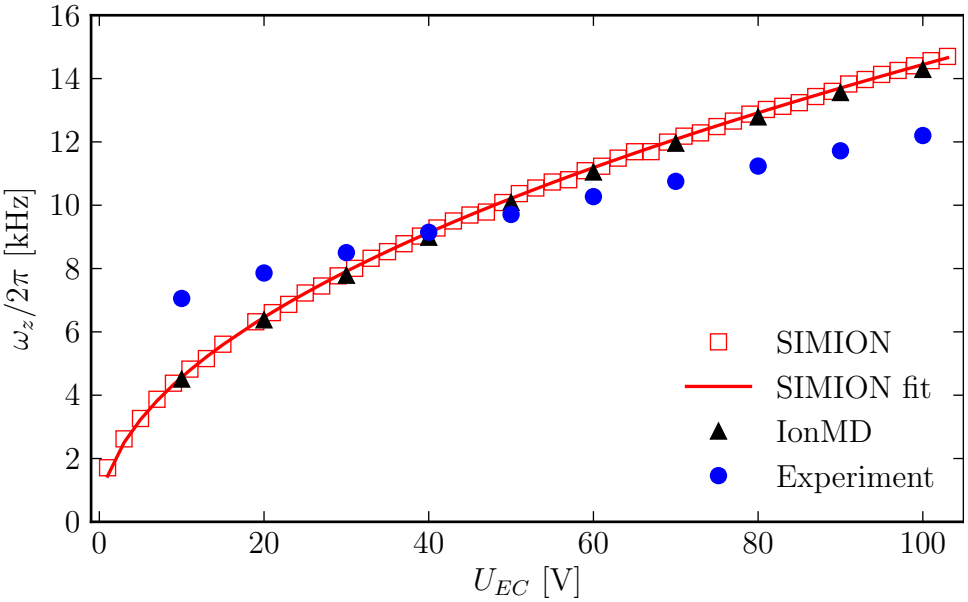

Figure 6.2: Comparison of simulated and measured axial secular frequencies. Trajectories for single ions were simulated in SIMION (squares) and used to determine the axial secular frequency for several end cap voltages U_{EC}. The axial frequency ω_z in this case conforms very well to the harmonic potential model where $\omega_z \propto \sqrt{U_{EC}}$ (solid line). Likewise, the center of mass frequency for 100 Ba^+ ions simulated in IonMD (triangles) responds to the end cap voltage quadratically as expected from the pseudopotential model used in the simulation. The experimentally determined response of ω_z to changes in U_{EC} using hundreds of ions (circles) deviates significantly from the harmonic potential prediction.

of measurements is as follows. Hundreds of Ba^+ ions are loaded and cooled to the crystal phase. Subsequently, the ions are allowed to react for several minutes with a neutral gas (see Section 6.4 for experimental details). At this point, the Coulomb crystal should show signs of the presence of other ions besides Ba^+. Next, one of the four RF electrodes is modulated with an additional AC voltage with the frequency swept in sync with the CCD camera in order to record Ba^+ fluorescence versus applied AC frequency.

Results of such a scan are displayed in Figure 6.3 for a Coulomb crystal consisting of Ba^+ and BaO^+ formed by the reaction

$$Ba^+ + O_2 \longrightarrow BaO^+ + O. \tag{6.9}$$

This reaction, which has been studied extensively elsewhere [82, 208], is endothermic by 1 eV[4]. The activation energy is low enough, however, that ions in the $P_{1/2}$ excited state have sufficient energy for reaction (6.9) to proceed rapidly enough to produce a sufficient proportion of BaO^+ ions for performing these measurements. Because reaction (6.9) is known to be the only reaction between Ba^+ and O_2 near room temperature, and since high purity O_2 is readily obtained, ambiguity in results can be minimized, making reaction (6.9) useful for testing and optimizing the AC sweep procedure.

Due to the deviations from the ideal single ion resonance frequencies discussed above, absolute mass identification from motional resonance coupling as implemented here is not possible. Instead, mass identification is based on knowledge of the chemical reactions involved and what the likely reaction products should be as well as comparing scan results of Coulomb crystals containing molecular ions produced using different reactions. In the event that a reaction can result in multiple product masses, this method is insufficient to fully identify the reaction products when at least one of the products is near the mass of another trapped ion. For example, in the reactions between Ba^+ and CH_3Cl (see Section 6.4.2), the production of BaH^+ is exothermic from the $P_{1/2}$ excited state of Ba^+. Since BaH^+

[4]See Appendix A for a brief review on estimating enthalpies of reaction to determine this, as well as data tables for these calculations.

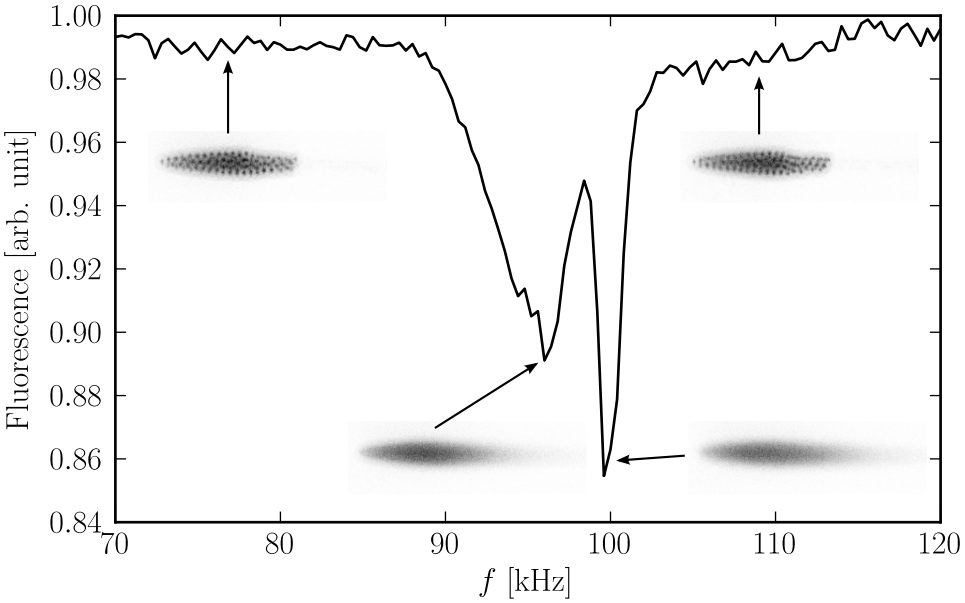

Figure 6.3: AC frequency sweep of a Ba^+ + BaO^+ ion crystal. Snapshot images show the trapped ions at the points indicated. Despite the heating and crystal melting evident in the two images associated with sympathetically and laser cooled ions, comparison of the first and last images shows that there is no total ion loss.

is only 1 amu heavier than Ba^+, a signature of its presence would not be distinguishable from the resonance of Ba^+ itself. Indeed, even with only Ba^+ ions of several isotopes present, the resolution of an AC frequency sweep is only good enough to provide one mass spectral feature.

Mass resolution is further limited by the Ba^+ q parameter used for most frequency sweeps. At higher RF voltages (and thus larger q), the RF heating rate of the ions is greater than at lower RF voltages. Ideally, AC frequency sweeps would be performed at fairly high V since this increases the separation between the resonant frequencies due to the dependence of ω_r on V. However, if the laser cooling rate is not fast enough to counteract the heating from the applied AC signal when near resonance, the crystal will melt and subsequently enter the gas phase. In principle, the AC sweeps could be repeated with sequentially lower amplitude until melting no longer occurs, but in practice, this greatly reduces the signal to noise ratio of these sweeps. Instead, a compromise RF voltage must be used such that the crystal never fully melts but also allows for a pronounced fluorescence

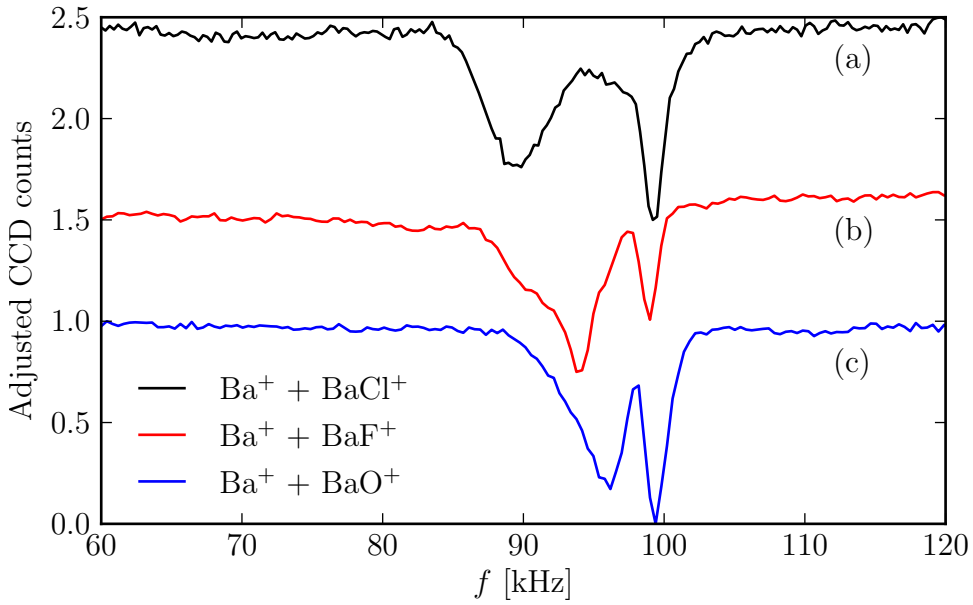

Figure 6.4: AC frequency sweep comparison following reactions between Ba^+ and (a) CH_3Cl, (b) SF_6, and (c) O_2. Lower resonance frequencies indicate ions of greater m/Z, and therefore these sweeps indicate that each reaction results in the desired products $BaCl^+$, BaF^+, and BaO^+. CCD counts are scaled and offset for clarity.

response when sweeping through sympathetically cooled ion resonances.

Limitations aside, AC frequency sweeps still proved useful in determining reaction product masses. A comparison of AC sweeps following reactions between Ba^+ and O_2, SF_6, and CH_3Cl is given in Figure 6.4. It is clear from these sweeps that since the resonance frequencies of the products are all different relative to that of Ba^+ that reactions are in fact due to the gases introduced and not some contaminants or residual background gases.

6.3.2 Coulomb crystal mass spectrometry

To overcome some of the limitations to AC frequency sweeps for mass determination, a simple method capable of a few amu resolution was developed that utilizes Coulomb crystals and the Mathieu stability parameters q [Equation (2.6)] and a [Equation (2.7)]. We know from the pseudopotential of Equation (2.29) and the results of the MD simulations of Chapter 3 that when crystallized, heavier ions will form shells surrounding lighter ions. This is visible in a fluorescence image of laser cooled ions as an apparent deformity in the

crystal structure. Barring reactions involving charge exchange, all reaction products that remain trapped will be heavier than Ba^+ and thus form on the exterior of the multi-component crystal. By applying DC pulses $\pm U/2$ to each RF electrode, the trap can be made unstable for heavy sympathetically cooled ions while remaining stable for lighter ions. This results in both a change in the crystal structure (the apparent deformity vanishes) as well as an overall contraction of the crystal towards the center of the trap (which appears as a shift towards the center for a multi-isotope crystal with one axial cooling beam). Thus by repeatedly performing this operation at several values of V and U, a portion of the Mathieu stability curves can be effectively mapped out and the heavier mass can be determined with better accuracy (albeit destructively) than with AC frequency sweeps. Because this method requires the use of Coulomb crystals in order to determine ejection of heavy masses, we call this technique Coulomb crystal mass spectrometry (CCMS).

In practice, the certainty with which U is known is much higher than that of V. This is due to the nature of the high voltage probes used to monitor the RF voltage which need to be calibrated for the frequency of the voltage they are measuring. The calibration procedure typically requires measuring a square wave at a fixed frequency with the probe and adjusting a variable capacitor built in to the probe until the ringing is minimized. However, this is most easily done by disconnecting the probe from the trap, which changes the total capacitance and therefore the resonant frequency, reducing the accuracy of the calibration. To get around this problem, after the ejection of heavy masses, U pulses are applied to record the value at which Ba^+ ions are ejected. Then in order to identify the heavier mass, a V scaling parameter is found by fitting the Ba^+ ejection data to the theoretical stability boundary curve using the polynomial fit of Equation (2.15). Finally, with this scaling of the measured values of V, the U values for heavy ion instability are fit to Equation (2.15) to extract the mass. The validity of this method was again first tested using the reaction (6.9) with results shown in Figure 6.5.

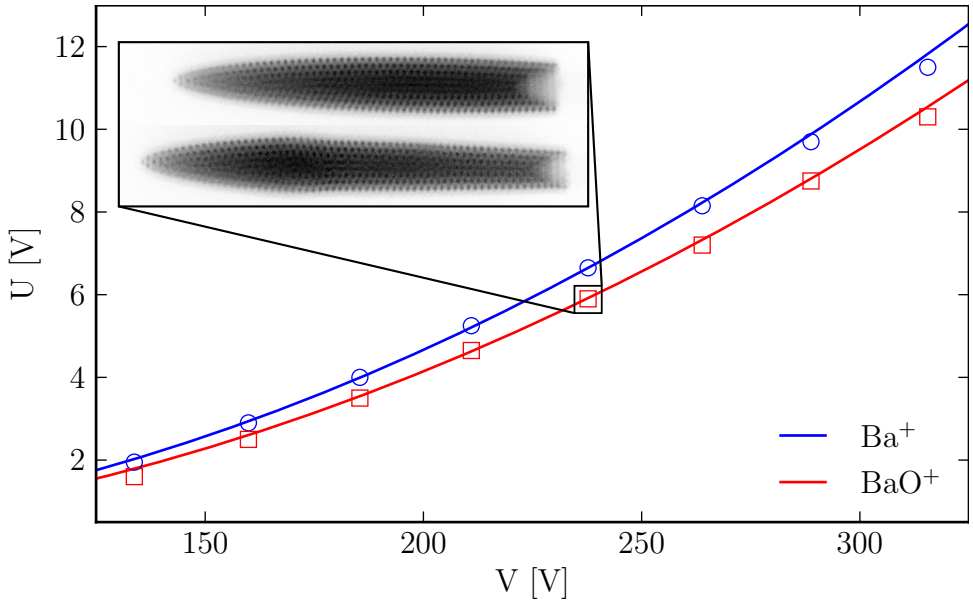

Figure 6.5: Coulomb crystal mass spectrometry of $Ba^+ + BaO^+$ ion crystals. Each square (circle) represents the DC voltage U required to eject BaO^+ (Ba^+) for a given RF voltage V. The blue curve is the theoretical Mathieu stability boundary for $m/Z = 138$ amu used for scaling the measured V values. Inset images show the Coulomb crystal before (bottom) and after (top) pulsing the U value indicated to eject BaO^+ ions. The red curve is a fit of the square data to the Mathieu stability curve. The fit gives a mass of 154.3 ± 0.9 amu, in excellent agreement with the mass of $^{138}Ba^{16}O^+$.

6.4 Reaction rate measurements

To measure reaction rate constants, there are a few methods available, each one involving measuring the loss rate of trapped reactant ions over time. Perhaps the ideal approach would be to simply count the number of ions as a function of time. Indeed, with small enough initial Coulomb crystals, this is a possibility, and can even be done with large crystals if the ion number can be precisely determined using MD simulations [82]. However, this either requires small enough numbers to count by hand or with image processing software, thus requiring more data for good statistics, or a large amount of computing time to produce MD simulated images that quantitatively correspond to observed images. Another method is to measure the volume of the crystal (as projected onto a two-dimensional CCD image) occupied by the laser cooled ions relative to the initial volume as a function of time. As more ions react, the volume occupied by the laser cooled ions decreases proportional to the loss rate. This method is acceptable so long as the ion density is approximately uniform, which is generally a reasonable assumption when the ion number does not get too large and the masses of all trapped ions are approximately the same [84].

Alternatively, with well-stabilized lasers (see Section 4.2.4), the integrated fluorescence from the laser cooled ions can be measured as a function of time since the number of scattered photons is proportional to the number of ions. Although the photon scattering rate depends on temperature, by operating the lasers in a regime where the observed fluorescence response to detuning is dominated by power broadening, this can be mitigated. By comparing the detected fluorescence to detuning for Coulomb crystals at different stages of a reaction (see Figure 6.6), it can be shown that there is no significant change to the measured lineshapes, meaning that the temperature of the laser cooled ions remains roughly constant and thus the scattering rate per ion can be treated as constant for a fixed detuning (see Figure 6.7). Additionally, it has also been shown explicitly by comparing numbers determined from quantitative MD simulations that measuring the exponential decay of fluorescence is directly proportional to the number of laser cooled ions [82]. This method is

straightforward, does not suffer from statistics or computing issues as with counting, and avoids potential systematic errors when using very large Coulomb crystals and so was the method employed for the experiments presented here.

In order to create BaX^+ molecular ions, reactants are leaked into the vacuum chamber at partial pressures of up to order 10^{-9} torr. At such pressures, trapped ions remain in an ordered state. SF_6, CH_3Cl, and Br_2 are utilized as reactants. SF_6 and CH_3Cl are in the gas phase at room temperature and are stored in a reservoir of about 500 mL. The reservoir was filled to pressures of slightly more than 1 atm which was then connected to the inlet of the leak valve. Br_2 is a liquid at room temperature, but has a sufficiently high vapor pressure ($\sim$ 185 torr [209]) to use as a gas phase reactant. A few mL of liquid bromine was added to a small reservoir at rough vacuum which was connected to the leak valve inlet.

To extract the rate constant from measured loss rates, it is necessary to know the concentration of the reactant gas. In the experiments presented in this thesis, this is accomplished by monitoring the pressure in the vacuum chamber after opening the leak valve and allowing the leak rate and pumping speed to reach an equilibrium. Pressures are monitored with a Bayard-Alpert ion gauge and it is assumed that the pressure reading is dominated by the reactant gas introduced, a fairly reasonable approximation since the background pressure ($\lesssim 5 \times 10^{-11}$ torr) is many times lower than the partial pressures introduced and any reactions between Ba^+ ions and residual background gases happen at a negligible rate. From Equation (6.2), we expect the loss rate τ^{-1} to increase linearly with reactant gas pressure. Thus by measuring the loss rate at different pressures, k can be determined from a linear fit to the data and assuming the introduced gas is at room temperature ($T = 298$ K). In the resulting fit, a finite y-intercept is interpreted to indicate a background loss rate mechanism [83] while a finite x-intercept indicates the background pressure.

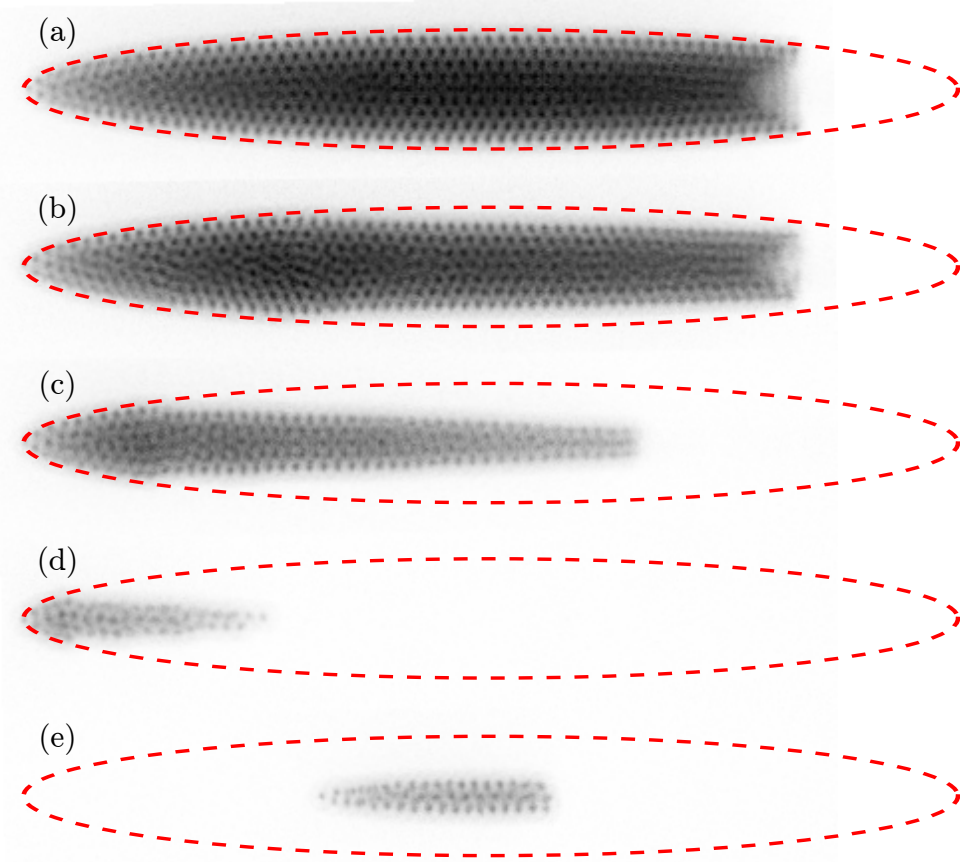

Figure 6.6: (a) A Coulomb crystal consisting of hundreds of laser cooled $^{138}Ba^{+}$ ions (dark regions) and sympathetically cooled Ba^{+} ions of other isotopes (not visible). (b)–(d) Subsequent images of the Coulomb crystal at different stages of a reaction with SF_6. (e) The remaining Ba^{+} ions as in (d) but following the ejection of heavy reaction product ions. The dashed ellipse in each image represents the approximate extent of the original Coulomb crystal in (a). Fluorescence indicates no loss of $^{138}Ba^{+}$ ions between (d) and (e). The major and minor diameters of each ellipse respectively measure about 1860 μm and 260 μm.

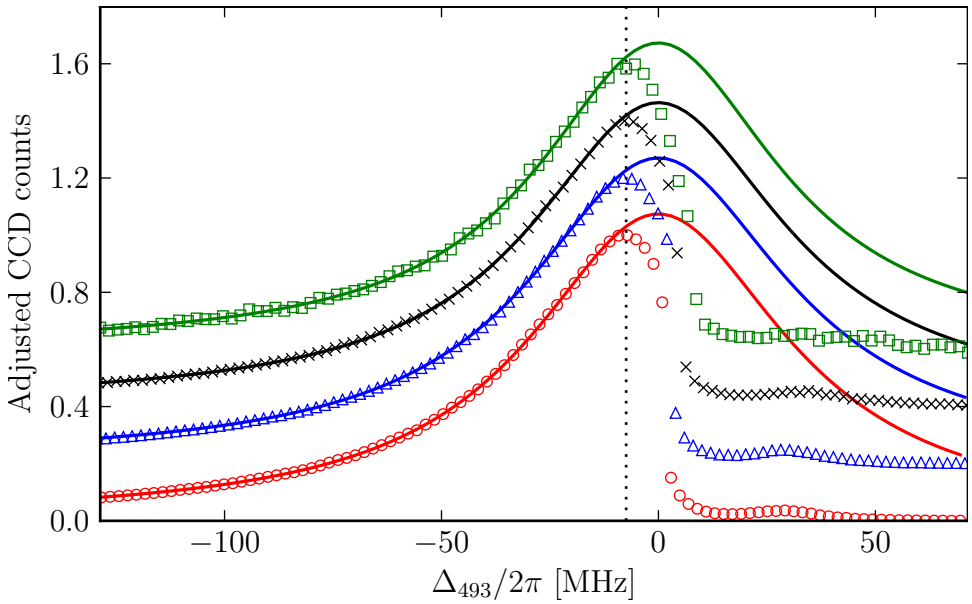

Figure 6.7: Measurements of $^{138}Ba^{+}$ fluorescence versus 493 nm laser detuning at different stages of the reaction with SF_6 in Figure 6.6. Absolute counts are background subtracted and scaled for comparison and offset for clarity. Circles, triangles, crosses, and squares correspond respectively to Figures 6.6(a), (b), (c), and (d). In each case, the reaction is halted by removing the reactant gas from the chamber prior to performing the measurement. Solid lines are Lorentzian fits to the data up to the point indicated by the dotted line with an average Lorentzian linewidth of 35(1) MHz. Near the blue detuned side of resonance, fluorescence drops off dramatically as the ions are heated.

Likely the largest single source of error in the measurement of reaction rates as performed here is the ion gauge used for pressure measurements. With only a single, uncalibrated ion gauge being used to measure low pressures of reactant gases, pressure measurements can only be considered to be accurate to within a factor of two or three. Additionally, some care must be taken in recording pressures since the ion gauge controller implicitly assumes a residual atmosphere of nitrogen. To account for this, the absolute pressure reading must be adjusted by using ion gauge correction factors ϵ which can be found in the ion gauge manual [210]. The corrected pressure reading is then given by $P_\epsilon = P/\epsilon$. Unfortunately, experiments performed to determine these correction factors in some cases found very different values for certain gases which further adds to the uncertainty in the pressure readings. As such, all pressures reported here, when corrected, are also given with the particular value of ϵ used for transparency. The subsequent sections describe the various experiments characterizing reactions with the aforementioned molecules in further detail.

6.4.1 Reactions with sulfur hexafluoride

Sulfur hexafluoride (SF_6) is an inert, potent greenhouse gas belonging to the O_h point group, making the spherical symmetry assumption of the Langevin model fairly reasonable. The reaction pathway is given by

$$Ba^+ + SF_6 \longrightarrow BaF^+ + SF_5 \tag{6.10}$$

which is exothermic by 2.8 eV. As expected, Ba^+ ions are lost following the introduction of SF_6 into the chamber and replaced by heavier product ions. The fact that they are heavier is apparent both in the crystal structure (product ions collect on the exterior of the ion crystal) and in AC frequency sweeps (resonances due to product ions appear at lower frequencies than that of Ba^+ ions, see Figure 6.4). A typical loss rate measurement after introducing SF_6 is shown in Figure 6.8. Accumulated measurements for determining the reaction rate are shown in Figure 6.9. The deduced rate constant is consistent with the prediction of the Langevin model.

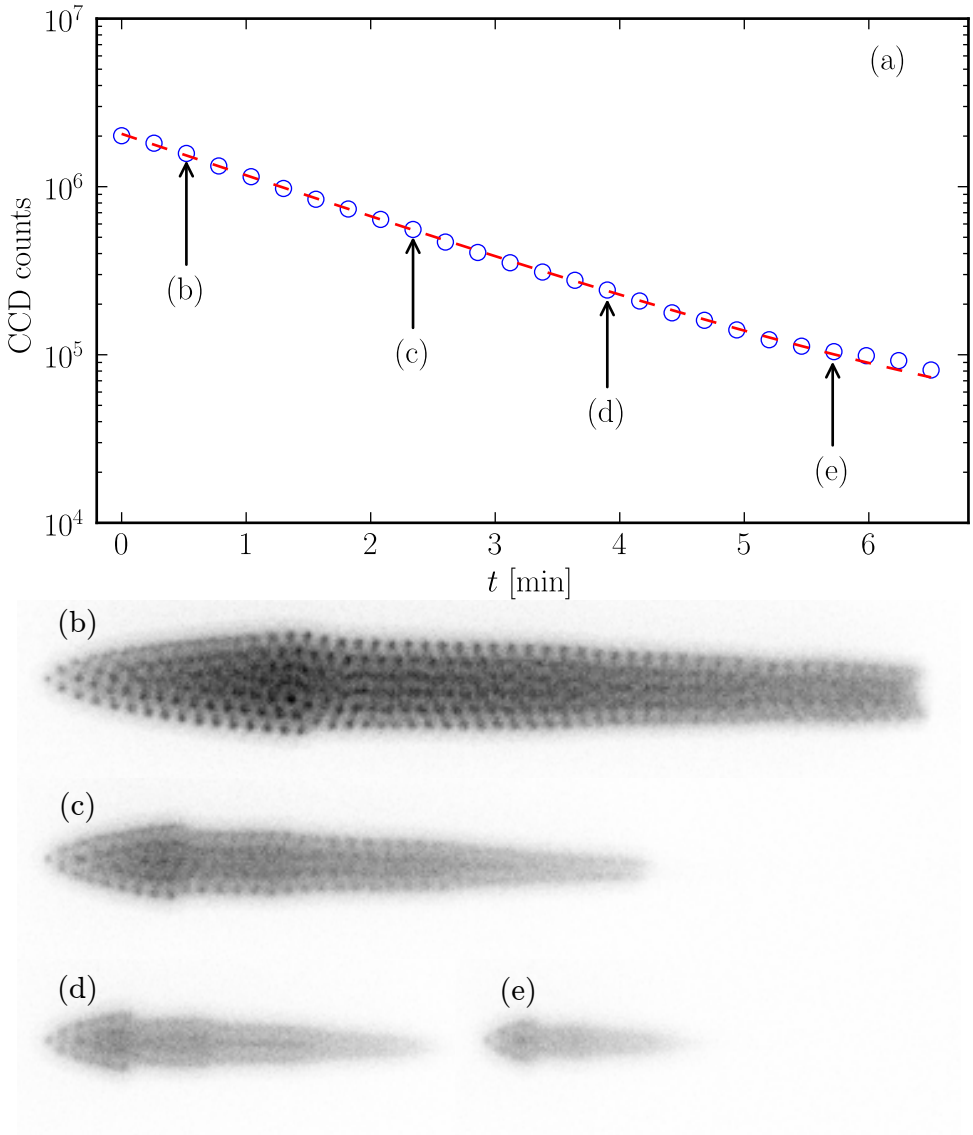

Figure 6.8: (a) A typical Ba^+ loss rate measurement due to reactions with SF_6 at a partial pressure of 2.8×10^{-10} torr. (b)–(e) Images of the Coulomb crystal over time as SF_6 reacts with Ba^+ to form BaF^+ ions. Note that the crystal structures show that reaction products collect on the exterior portion of the Coulomb crystal which indicates that they are heavier than Ba^+.

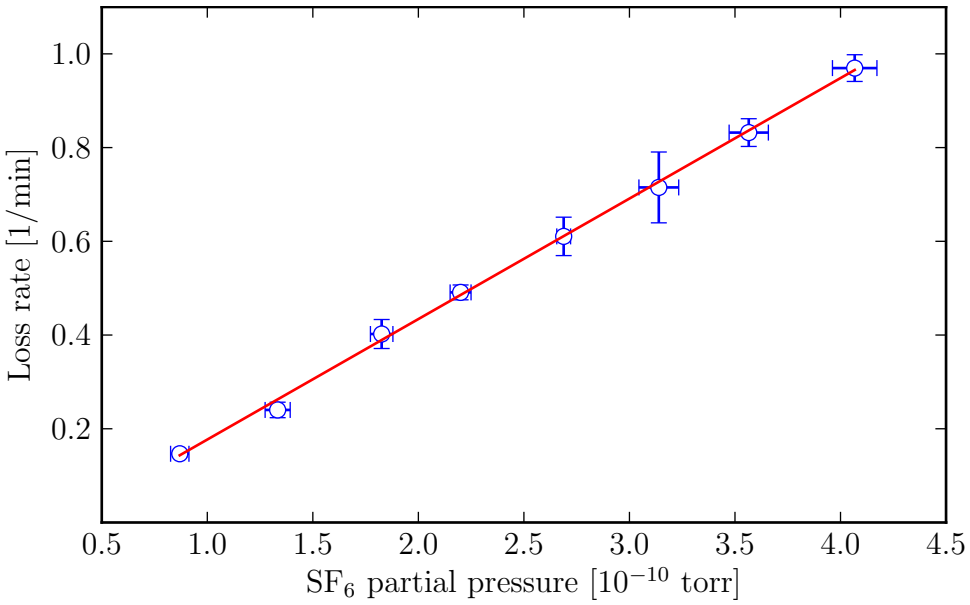

Figure 6.9: Reaction rate constant measurement for the reaction (6.10). Each point represents the average measured Ba^+ ion loss rate at a given target partial pressure. Vertical error bars represent the standard deviation of the measured loss rates and horizontal error bars indicate the standard deviation of the pressure recorded by the ion gauge. The solid line is a linear fit to the data. Partial pressures are using the ion gauge correction factor $\epsilon = 2.3$.

It should be noted that the masses of BaF^+ ($m/Z \approx 157$ amu) and BaO^+ ($m/Z \approx 154$ amu) are very close to one another. Given the uncertainties involved with determining masses by using AC frequency sweeps, a frequency sweep alone is not sufficient to conclusively show that Equation (6.10) is the reaction mechanism as opposed to reactions with contaminants. Furthermore, SF_6^+ ($m/Z \approx 146$ amu) also has a mass fairly close to that of BaF^+ and BaO^+. Charge exchange is energetically forbidden, however, since the ionization energy of SF_6 is > 15 eV compared to 5.2 eV for Ba [211, 212]. Additionally, theory predicts that SF_6^+ rapidly ejects a fluorine atom to become SF_5^+ which is lighter than Ba^+ by about 10 amu [213]. Since no Coulomb crystals were observed containing lighter sympathetically cooled ions, these last two points indicate that the reaction products must all be heavier than Ba^+. Nevertheless, in order to entirely rule out the possibility of reactions with contaminants, CCMS measurements were performed following reactions that occurred after the introduction of SF_6. The results shown in Figure 6.10, combined with the

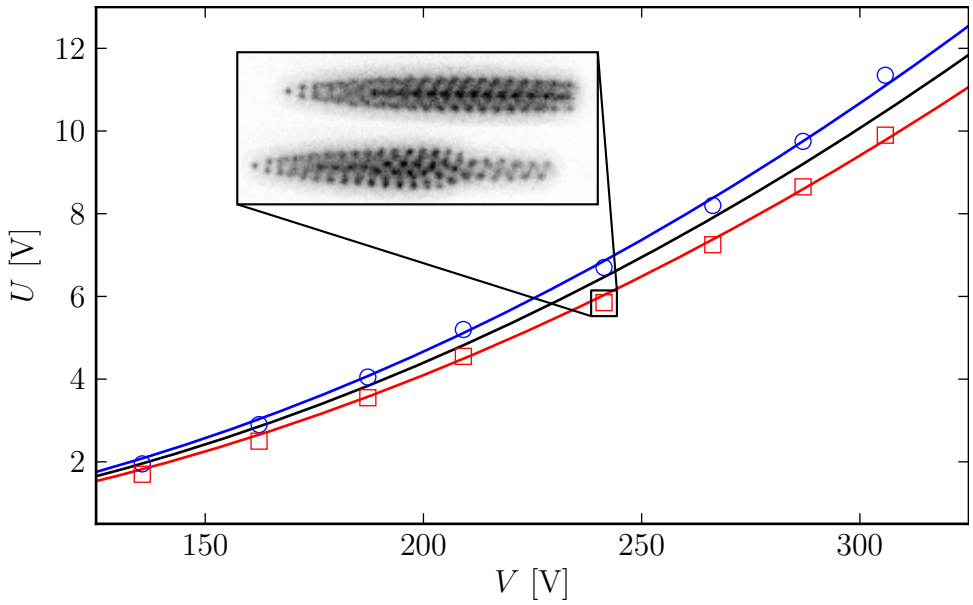

Figure 6.10: Coulomb crystal mass spectrometry of Ba^+ + BaF^+ ion crystals. The black curve represents the theoretical stability curve for SF_6^+. The inset images show an ion crystal before (bottom) and after (top) ejecting ions heavier than Ba^+ at the voltages indicated.

AC frequency sweeps and the energy considerations described above, allow us to conclude that we are in fact producing BaF^+ via the reaction (6.10).

6.4.2 Reactions with methyl chloride

Methyl chloride (CH_3Cl), also known as chloromethane, is an extremely flammable, moderately toxic gas. CH_3Cl was chosen as a reactant for producing $BaCl^+$ due in part to the success of other experiments in using it and fellow halomethane CH_3F in reactions with trapped, laser cooled Ca^+ ions [18, 19, 86]. The reaction

$$Ba^+ + CH_3Cl \longrightarrow BaCl^+ + CH_3 \tag{6.11}$$

is exothermic by 0.6 eV. Because CH_3Cl has a permanent dipole moment, the dipole corrected form of the Langevin model must be used to predict an upper bound on the reaction rate constant. Ba^+ ion loss rate measurements when adding CH_3Cl gas to the chamber were performed in an identical manner as those with SF_6 described above. The reaction (6.11) is likely the only exothermic reaction between Ba^+ ions in the ground state and CH_3Cl, but

the reaction

$$Ba^+ + CH_3Cl \longrightarrow BaH^+ + CH_2Cl \tag{6.12}$$

is endothermic by 2.3 eV, and so could occur with Ba^+ ions in the $P_{1/2}$ excited state. It is thus possible that BaH^+ ions were produced in some amount, though neither mass spectroscopic method had sufficient resolution to determine this with certainty. Additionally, there is insufficient data in the literature to estimate the reaction enthalpy for the reaction $Ba^+ + CH_3Cl \longrightarrow BaCH_3^+ + Cl$ and therefore determine whether or not it would be energetically allowable. However, it is sufficiently heavier than Ba^+ to be resolvable with AC frequency sweeps. Since no such resonances were observed, this reaction can be reasonably ruled out. Further studies with improved mass resolution via time-of-flight mass spectrometry [192] or high precision non-destructive techniques [203] would be necessary to fully analyze reaction products.

The results from a typical Ba^+ loss rate measurement are shown in Figure 6.11. All such measurements are compiled in Figure 6.12 from which the reaction rate constant was deduced assuming reaction (6.11) is the dominant reaction. The resulting rate constant was found to be consistent with the upper bound predicted by the dipole-corrected Langevin model.

6.4.3 Reactions with bromine and iodine

Although bromine (Br_2) and iodine (I_2) are respectively a liquid and a gas at room temperature, both have fairly high vapor pressures at room temperature (about 185 mtorr for Br_2 and 300 mtorr for I_2 [209]). In principle, then, the reactions of each with Ba^+ should be measurable in the same manner as with SF_6 and CH_3Cl. The reactions

$$Ba^+ + Br_2 \longrightarrow BaBr^+ + Br \tag{6.13}$$

$$Ba^+ + I_2 \longrightarrow BaI^+ + I \tag{6.14}$$

are each exothermic by 2.2 eV. In their aqueous ("wet") forms, both Br_2 and I_2 are not suitable for use with the stainless steel of the vacuum system, but are acceptable for short

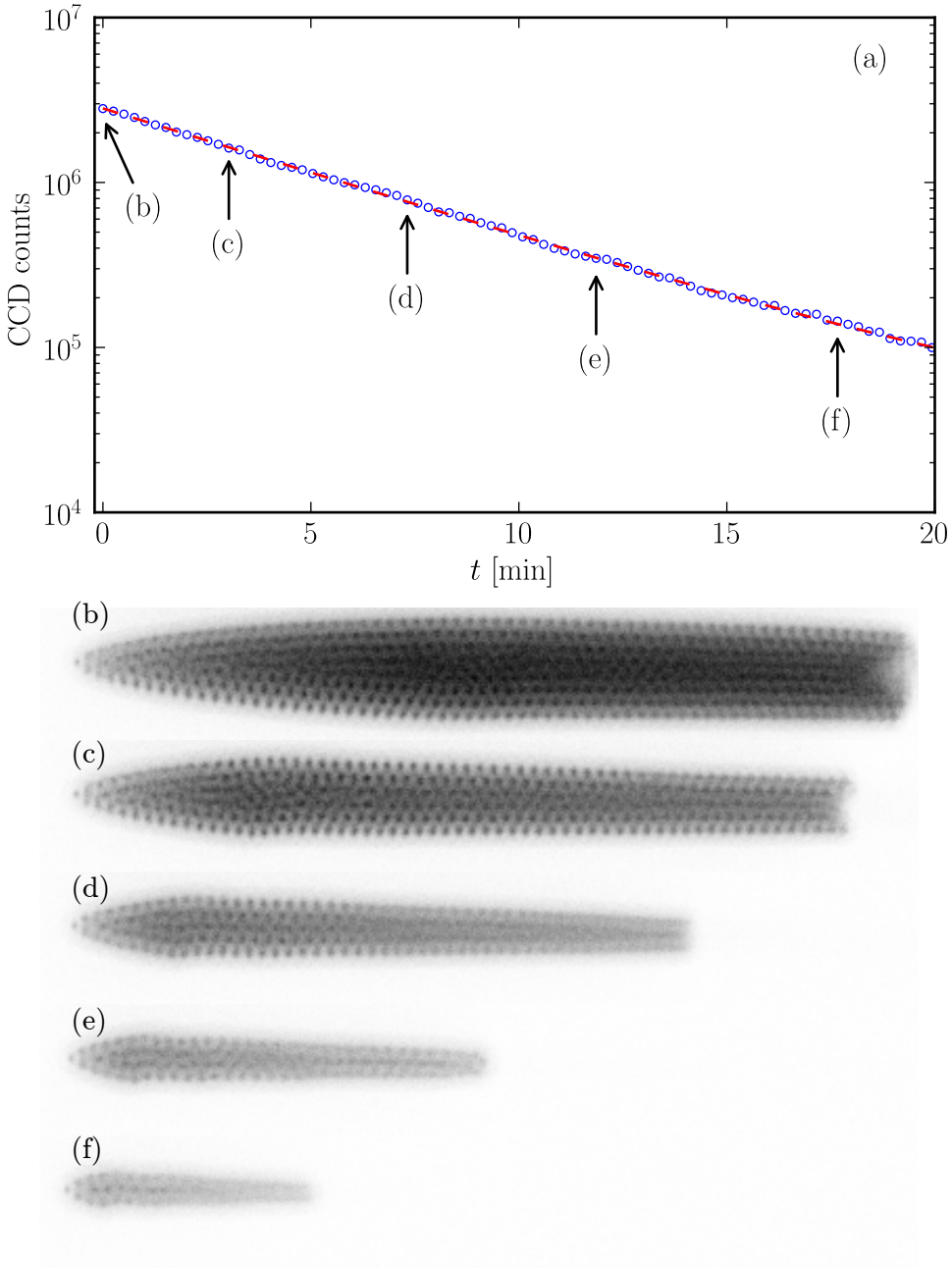

Figure 6.11: (a) A typical Ba^+ loss rate measurement in the presence of CH_3Cl gas at a partial pressure of 7.7×10^{-11} torr. (b)–(f) Images of the Coulomb crystal at the points indicated in (a).

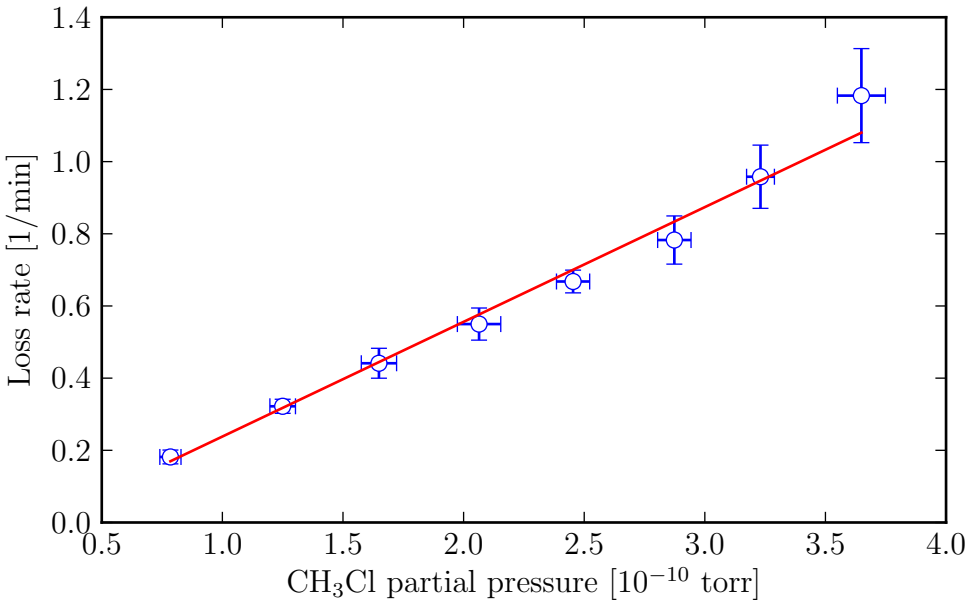

Figure 6.12: Reaction rate constant measurement between Ba^+ and CH_3Cl. The resulting fit assumes the reaction (6.11) is predominant. Pressures utilize the ion gauge correction factor $\epsilon = 2.6$.

term use in their "dry" forms, both of which can be easily obtained from various chemical suppliers. Nevertheless, much more care is required when handling these halogens compared to the gases used in the preceding sections. In each case, preparation of samples was performed in a fume hood. The liquid nature of Br_2 also introduces some complications in preparing a sample to be introduced to the vacuum chamber, the details of which will be discussed shortly.

BaI^+ has a mass of about 265 amu, nearly twice that of Ba^+. This strains the ability of Ba^+ to sympathetically cool BaI^+, but nevertheless, molecular dynamics simulations indicate that BaI^+ crystallizes thanks to sympathetic cooling at sufficiently low RF voltages (Figure 6.13). To get I_2 vapor into the chamber, several flakes of crystalline I_2 (several grams) were put in a standard length 1.33" CF nipple which is blanked on one end and fit with a CF to Swagelok adaptor and valve on the other. This assembly was connected to the fittings of the leak valve inlet and the residual atmosphere was evacuated to rough vacuum. From this point forward, the experimental procedure for attempted production of BaI^+ was the same as outlined in the preceding sections. Although reactions were observed, CCMS

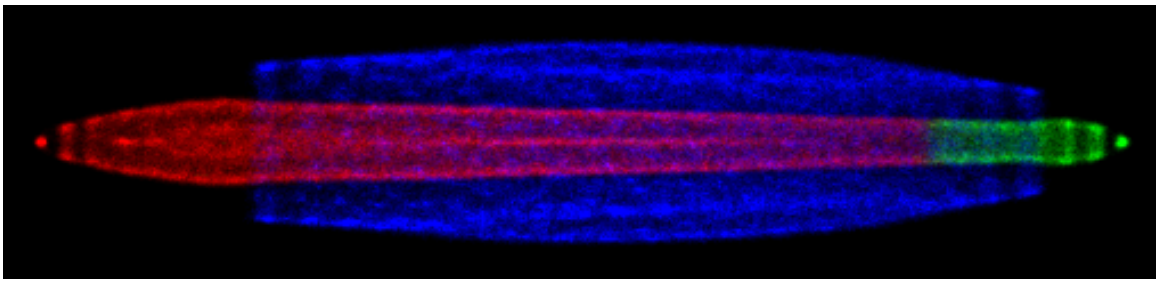

Figure 6.13: A MD simulation of sympathetically cooled BaI^+ Coulomb crystals. In this case, there are a total of $N = 600$ ions, 60% of which are BaI^+ (blue), and the remainder being $^{138}Ba^+$ (red) and $^{136}Ba^+$ (green).

mass determination, along with AC frequency sweeps, indicated that the major products were BaO^+. Because the leak valve had to be opened quite a bit more than with the gas phase reactants, it was presumed that reactions were occurring with contaminants and that little or no I_2 reached the stored Ba^+ ions. Given that the leak valve outlet was oriented without a line of sight to the trap, it is likely that any I_2 vapor in the UHV portion of the chamber ended up either adsorbed onto the chamber walls or pumped out of the system long before reaching the ions, thus precluding reactions from being studied.

For studying reactions between Ba^+ and Br_2, the liquid bromine must be prepared in such a way as to evacuate atmospheric contaminants from its reservoir without boiling away all of the liquid. To accomplish this, a reservoir was fashioned out of a stainless steel NPT tee fitting with two stainless steel valves and a blank on the remaining opening. A section of PVDF tubing was connected to one of the valves and filled with a few mL of bromine using a syringe. Meanwhile, the tee was evacuated through the second valve which was closed once rough vacuum was attained. After eliminating any air bubbles from the bromine in the PVDF tubing, its valve was opened to allow it to enter the reservoir. The valve was shut before all the liquid had been drained in order to prevent atmospheric contamination. Thus filled, the reservoir was connected to the leak valve inlet as before.

As with attempted reactions with I_2, it was necessary to open the leak valve considerably more than with the gas phase reactants. Furthermore, the pressure readings were

erratic, precluding the possibility of measuring loss rates at any specific pressure and therefore discounting a determination of the reaction rate constant. To further complicate matters, mass determination following initial attempts at $BaBr^+$ production indicated reactions with contaminants to form BaO^+ as before with I_2. In order to suppress reactions from occurring with contaminants, the cooling and repumper beams were blocked during subsequent reaction attempts when the leak valve was opened since the reaction (6.9) is endothermic with respect to the Ba^+ ground state, as is the reaction

$$Ba^+ + CO_2 \longrightarrow BaO^+ + CO, \tag{6.15}$$

which is another possible contaminant reaction [82]. Although the reaction with water

$$Ba^+ + H_2O \longrightarrow BaOH^+ + H \tag{6.16}$$

is exothermic, it has been observed to behave much like an endothermic reaction and therefore is greatly suppressed by extinguishing the laser light [208]. With the lasers blocked, reactions were allowed to proceed between Ba^+ and Br_2 for up to a couple of minutes before closing the leak valve and unblocking the cooling and repumper lights. After recooling, the resulting Coulomb crystals indicated the presence of a small fraction of heavier sympathetically cooled ions, far too few to expect any noticeable signature by using AC frequency sweeps. Indeed, such measurements showed only the response of Ba^+ itself.

To verify that $BaBr^+$ had been produced, CCMS measurements were performed on a few resulting Coulomb crystals. Since the fraction of sympathetically cooled ions produced from reactions was small, this also served as a good test of the limits of the CCMS technique which had heretofore been performed on Coulomb crystals with large fractions of non-fluorescing ions. Ejection of the small number of heavy ions resulted in a contraction of the crystal by only a few μm, but the imaging resolution was sufficient to resolve this, and therefore the method was still functional. The results from these measurements are shown in Figure 6.14 and strongly indicate that $BaBr^+$ was produced through the reaction (6.13).

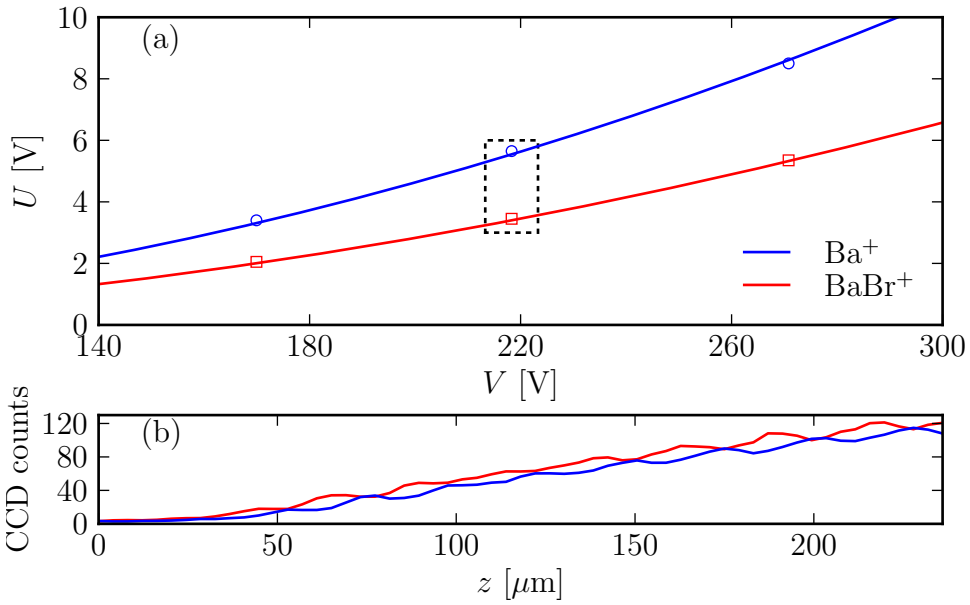

Figure 6.14: Coulomb crystal mass spectrometry of Ba^+ + $BaBr^+$ ion crystals. (a) U, V pairs for the ejection of $BaBr^+$ (red squares) and for the ejection of Ba^+ (blue circles). The solid lines correspond to the theoretical Mathieu stability parameters for each species. (b) Integrated fluorescence counts for a region of interest near the edge of the Coulomb crystal before (red) and after (blue) applying the voltages indicated with the dotted box in (a). Note the overall shift towards the center of the trap (to the right).

As with I_2, it is likely that the difficulty in producing $BaBr^+$ was due in part to little Br_2 reaching the stored ions. This is evidenced by the ion gauge giving inconsistent readings while Br_2 was leaked into the chamber. Adsorption onto the chamber walls is once again suspected as a likely explanation for the difficulty in producing $BaBr^+$. The significantly higher vapor pressure of Br_2 compared to I_2 may also explain why some $BaBr^+$ was produced but no BaI^+ was seen.

6.5 Conclusion

A summary of measurements compared with theoretical estimates of reaction rate constants is given in Table 6.1. In the two cases that were able to be measured, the rate constants were each consistent with the Langevin (SF_6) and dipole-corrected Langevin (CH_3Cl) models. Further studies with the leak valve oriented with a line of sight to the trapped Ba^+ ions could allow for a systematic study of reaction rates between Ba^+ and Br_2 and I_2, though given the

Table 6.1: Reaction rate constants between Ba^+ and neutral reactants used in this work in units of 10^{-9} cm^3 s^{-1}. Reaction rate constants k using uncorrected ion gauge pressure readings are multiplied by ion gauge correction factors ϵ to obtain the corrected reaction rate constants $k_\epsilon = \epsilon k$. Ion gauge correction factors are obtained from [210]. Also listed are the theoretical Langevin rate constant (k_L), dipole correction term (k_D), and upper bound corrected Langevin rate constant ($k_c \leq k_L + k_D$) using polarizabilities from [214–217] and dipole moment from [218].

Reactant	k	ϵ	k_ϵ	k_L	k_D	k_c
SF_6	0.6	2.3	1.3	0.6	—	—
CH_3Cl	0.6	2.6	1.6	0.8	2.0	≤ 3.7
Br_2	—	3.8	—	0.7	—	—
I_2	—	5.4	—	0.8	—	—

corrosive nature of the halogens, a more suitable method of production of $BaBr^+$ and BaI^+ using a gas phase reactant may involve the use of some other molecules containing Br or I. This approach is somewhat complicated by the fact that many equivalent molecules to those studied here are either highly toxic (*e.g.*, CH_3Br and CH_3I) or in the liquid phase at room temperature (*e.g.*, CH_3I). Nevertheless, the results presented here demonstrate that the production of barium monohalide ions can be easily achieved with the right selection of reactant. Many more gas phase reactants exist containing F, rather than the other halogens, which are non- or mildly toxic making BaF^+ the best candidate of the barium monohalide ions for future work in rovibrationally cooling molecular ions produced via reactions.

Chapter VII

CONCLUSION AND FUTURE DIRECTIONS

This thesis has presented experiments involving the measurement of electronic lifetimes of the Th^{3+} ion as well as studies of the formation of barium monohalide molecular ions through chemical reactions with trapped and laser cooled Ba^{+} ions. The first experiment was unfortunately cut short due to unexplained difficulties in consistently loading Th^{3+} produced by laser ablation, a recurring problem in other experiments with such ions. Preliminary results showed that, despite many possible systematic effects, the use of a large number of Th^{3+} ions in the presence of a rather large amount of buffer gas relative to the background pressure did not seem to drastically affect the measured lifetimes, with the exception of the measured dependence of observed lifetime on the RF voltage, which was particularly noticeable at lower RF amplitudes. Although the precise mechanism was not understood, the dependence of the measured lifetime on RF voltage was attributed to excess micromotion that could not be fully compensated for due to inadequate end cap electrode design. Subsequently, improved end caps were fabricated and installed, and from that point forward, no evidence of loading Th^{3+} was seen again. Nevertheless, some preliminary measurements of the $6^2D_{5/2}$ excited state lifetime were made with Th^{3+} ions in buffer gas, the average value of which is in agreement with state of the art theoretical predictions, a good indication that the theoretical models used are quite robust.

The second experiment explored the production of molecular ions through reactions with laser cooled Ba^{+} ions. This method of production results in molecular ions that, while not in the rovibrational ground state, are automatically cooled translationally through their Coulomb interaction with the remaining Ba^{+} ions. By choosing appropriate reactant gases to use, different molecular ions can be produced, making this method of molecular ion

production much more versatile than other methods such as laser ablation of a specific target. In particular, the experiments presented in this thesis focused on the production of barium monohalide ions, BaX^+, which hold a great deal of promise for cooling to the rovibrational ground state via sympathetic cooling with ultracold neutral atoms since the BaX^+ ions have both large dissociation energies and the neutral precursor BaX have large ionization energies. These two factors make BaX^+ highly unlikely to charge exchange or react with sympathetic coolant neutral atoms.

An important step towards studying ultracold molecular ions is examining production methods. Here, reaction rate constants were measured for two different reactions with Ba^+ to produce the barium monohalide ions BaF^+ and $BaCl^+$. While the reaction rate constant was not quantifiable, a third reaction with Ba^+ was verified to occur which produced $BaBr^+$ molecular ions. With these three reactions, BaF^+, $BaCl^+$, and $BaBr^+$ were all sympathetically cooled by the remaining Ba^+ ions. Mass spectroscopic techniques were used to verify the production of the desired molecular ions, though more work will need to be done in order to fully determine reaction pathways and branching ratios in cases where multiple reactions could conceivably occur.

7.1 Future directions

7.1.1 Thorium

The long term goal of the thorium project, finding—and ultimately exploiting—the nuclear isomer ^{229m}Th state has still not been realized. Progress has been modest, in large part due to the technical challenges in working with an ion in its third ionization state and with $^{229}Th^{3+}$ ions in particular. Despite these challenges, the Kuzmich group has had success with directly laser cooling $^{229}Th^{3+}$ ions as well as sympathetically cooling them with laser cooled $^{232}Th^{3+}$ ions. Either cooling method will be necessary in order to achieve single ion addressability for a high precision nuclear clock.

Because both the long term goal of driving the isomer transition and the more modest

goal of measuring Th^{3+} electronic state lifetimes have been made more difficult by the challenges in producing and loading Th^{3+}, a worthwhile endeavor would be to thoroughly study the production process of laser ablation. Time of flight mass spectrometry (TOFMS) on ablation products from a thorium target has already been performed by Zimmermann *et al.* [219], although that group was primarily concerned with producing singly ionized thorium. Additionally, the geometry of the target relative to the trap was considerably different than the axial loading method used in this thesis and other Th^{3+} experiments at Georgia Tech and used a pulsed nitrogen laser at $\lambda = 337$ nm rather than the third harmonic of a pulsed Nd:YAG laser at $\lambda = 355$ nm. Interestingly, despite observing a large peak due to Th^{2+}, Zimmermann *et al.* observed no such signature of Th^{3+}. At any rate, there remains much work to be done in order to understand how to fully optimize the production and trapping of Th^{3+}.

A simple experiment that could be performed to study the production of Th^{3+} ions via ablation could use a similar setup as with the ion traps used earlier. Because the problems experienced with loading Th^{3+} all occurred in similar target and trap configurations, a logical starting point for a TOFMS experiment would be to orient a target just outside a long ion guide which doubles as a trap with a gateable end cap. At the end of the guide furthest from the target would be a CEM or other charge sensitive device and the length of this guide would be chosen in order to satisfy usual TOFMS resolution requirements. With such a configuration, the experiment could be performed with or without the guide RF and end cap gating enabled, and each of these parameters could be varied in order to study their effects on the resulting ablation products reaching the detector. This experiment would be relatively straightforward to implement, and given the unexplained difficulties in loading Th^{3+} could prove very useful in diagnosing specific causes of this problem.

Measurements of the Th^{3+} electronic state lifetimes can also be improved, once Th^{3+} production and trapping is made more reliable. By using a single, cold Th^{3+} ion, systematic

effects due to buffer gas and the presence of many ions in the collection region can be minimized or eliminated. For measurements of the two excited states, a similar method to that which is presented in Chapter 5 could be used (*i.e.*, populating the excited state of interest, then turning off the illumination and recording photon arrival times). For measuring the metastable $5^2F_{7/2}$ state lifetime, a shelving method would be more ideal [220, 221]. In any case, perhaps the best approach would be to sympathetically cool a single Th^{3+} ion using a laser cooled ion such as Ba^+. By doing this, the Th^{3+} ion can be cooled continuously without the adverse systematic effects of constant illumination by near resonant light.

7.1.2 Molecular ions

The study of cold molecular ions has only just started to develop with much work remaining to be done. While ultracold neutral molecules have been studied in detail thanks to production methods such as Feshbach resonances and photoassociation [222], producing internally cold molecular ions has been more challenging. Recent years have seen the introduction of rovibrational cooling by optical pumping [69, 71], internal state relaxation through sympathetic cooling [94], as well as some proposals for direct laser cooling of a few special case molecular ions (*e.g.*, BH^+ and AlH^+) [66]. The first of these techniques is likely to apply to most ionic hydrides due to their large vibrational constants which results in a high probability for a molecule to be in the vibrational ground state. Furthermore, the translational motion of molecular ions can be trivially cooled via sympathetic cooling with a directly laser cooled atomic ion. Many direct laser cooling approaches, though, tend to suffer from a lack of generality and only apply to a few very specific molecular ions.

In addition to the prospect of cooling BaF^+ ions to the rovibrational ground state, there is also a great deal of cold chemistry yet to be studied with Ba^+ ions. Most studies to date of reactions between laser cooled ions and neutral molecules below room temperature have been undertaken with Ca^+ ions. Although it is also an alkaline earth metal and should therefore exhibit similar reaction dynamics as Ba^+, there are some differences, such as with

the reactions with CH_3Cl; in the case of Ca^+, the reaction rate with CH_3Cl was considerably slower than even the Langevin model predicts [19], whereas the Ba^+ reactions measured here were consistent with dipole-corrected upper bound rate constant predictions.

As only a small number of reactions were studied here, an obvious next step would be to study the reactions with further reactant gases. As mentioned in the conclusion to Chapter 6, other reactants could be chosen in order to more easily produce $BaBr^+$ and BaI^+, though the options here are somewhat more limited than those for the production of BaF^+ and $BaCl^+$. Out of known compounds which contain halogens, some potential gas phase reactants which are not overly toxic or combustible and are not too difficult to obtain include NF_3, CF_4, CH_2F_2, and CHF_3. Note, however, that these all contain fluorine and none of the other halogens. The hydrogen halides (HF, HCl, HBr, and HI) could also be used, though some extra caution would be necessary. These are all more commonly found in their aqueous, hydrohalic acid forms, but when not in solution, each is a colorless gas at room temperature. Additionally, SiF_4, while itself toxic and corrosive, can be produced in vacuo by heating $BaSiF_6$ to 300 °C [223].

The other principal avenue for future work is with cold reactive collisions between Ba^+ and neutral polar molecules. In order to obtain slow molecules, techniques include quadrupole velocity filters [19, 86], Stark decelerators [189, 224], and the related Zeeman decelerators [225, 226], among others [227]. These methods allow for studying reactions in low energy regimes where angular momentum and quantum effects play a more significant role than at room temperature, and thus are interesting to study in their own right. These techniques are generally limited to polar neutral molecules, but extending the work presented in this thesis to study such reactions between Ba^+ and polar molecules would be a fairly simple extension.

Appendix A

REACTION ENTHALPIES

In order to predict likely outcomes when attempting reactions, it is important to know whether or not they will react in the first place and what the possible end products are. This can be done by estimating the enthalpy of reaction ΔH_{rxn} for a possible reaction pathway. For reactions between ions and neutrals, this involves considering both bond dissociation energies as well as ionization energies. It follows from conservation of energy[1] that the enthalpy of reaction can be calculated by summing the enthalpies of any series of reactions such that the initial reactants and final products match. In other words, for the reaction $A + B \longrightarrow C + D$,

$$\Delta H_{rxn}(A + B \longrightarrow C + D) = \Delta H_{rxn}(A + B \longrightarrow E) + \Delta H_{rxn}(E \longrightarrow C + D) \tag{A.1}$$

for any intermediate products E.

As an example, consider the reaction $Ba^+ + SF_6 \longrightarrow BaF^+ + SF_5$. To determine ΔH_{rxn}, the dissociation energies of the Ba−F bond and F−S bonds are needed in addition to the ionization energies of Ba and BaF. Dissociation energies for several bonds are listed in Table C.5 and ionization energies in Table C.6. The reaction can be broken down into the following four steps:

$$Ba^+ + e^- \longrightarrow Ba$$

$$SF_6 \longrightarrow F + SF_5$$

$$Ba + F \longrightarrow BaF$$

$$BaF \longrightarrow BaF^+ + e^-$$

[1] Or Hess's law in this context, if you prefer.

The total change in enthalpy is the sum of the change in enthalpy for each step:

$$\begin{aligned}\Delta H_{rxn} &= -\mathrm{IE(Ba)} + D_0(\mathrm{F{-}S}) - D_0(\mathrm{Ba{-}F}) + \mathrm{IE(BaF)} \\ &= -5.2\ \mathrm{eV} + 3.6\ \mathrm{eV} - 6.1\ \mathrm{eV} + 4.9\ \mathrm{eV} \\ &= -2.8\ \mathrm{eV}.\end{aligned}$$

This and enthalpies of reaction for other reactions of relevance to this thesis are compiled in Table A.1.

Table A.1: Estimated enthalpies of reaction ΔH_{rxn} in eV for several reactions involving Ba^+ ions. Positive values indicate a reaction is endothermic. $*$ Reactions studied in this work. † Reaction studied in Refs. [82, 208]. ‡ Reaction studied in Refs. [192]. § Although these reactions are endothermic with respect to the ground sate of Ba^+, they are exothermic for Ba^+ ions in the $6^2P_{1/2}$ excited state.

Reaction	ΔH_{rxn}	Notes
$Ba^+ + O_2 \longrightarrow BaO^+ + O$	1	$*$, †, §
$Ba^+ + F_2 \longrightarrow BaF^+ + F$	-4.8	
$Ba^+ + Cl_2 \longrightarrow BaCl^+ + Cl$	-2.2	
$Ba^+ + Br_2 \longrightarrow BaBr^+ + Br$	-2.2	$*$
$Ba^+ + I_2 \longrightarrow BaI^+ + I$	-2.2	$*$
$Ba^+ + HCl \longrightarrow BaCl^+ + H$	-0.2	‡
$Ba^+ + SF_6 \longrightarrow BaF^+ + SF_5$	-2.8	$*$
$Ba^+ + CH_3Cl \longrightarrow BaCl^+ + CH_3$	-0.6	$*$
$Ba^+ + CH_3Cl \longrightarrow BaH^+ + CH_2Cl$	2.3	$*$, §
$Ba^+ + CF_4 \longrightarrow BaF^+ + CF_3$	-0.4	
$Ba^+ + CCl_4 \longrightarrow BaCl^+ + CCl_3$	-0.6	

Appendix B

PROGRAM LISTINGS

B.1 Stability determination

```
import os
import time
from numpy import *
from scipy.integrate import odeint, ode
import matplotlib.pyplot as plt

# Stability parameters
q, a = 0.6, 0.
qlist = arange(0, 10, 0.1)
alist = arange(-5, 10, 0.1)
n = len(qlist)*len(alist)
Q, A = meshgrid(qlist, alist)
S = zeros(Q.shape, dtype=int8)

# Initial conditions
xi_init_even = [1., 0.]
xi_init_odd = [0., 1.]
zeta = arange(0., pi, 0.05)

ti = time.clock()
t = ti
curr = 0
for i, q in enumerate(qlist):
    for j, a in enumerate(alist):
        # Mathieu equations expressed as 2 first order ODEs
        # xi[0] = u, xi[1] = u'
        xi_prime = lambda xi, zeta: [xi[1], -(a - 2*q*cos(2*zeta))*xi[0]]

        # Solve
        xi_even = odeint(xi_prime, xi_init_even, zeta)
        xi_odd = odeint(xi_prime, xi_init_odd, zeta)

        # Convergent?
        S[j,i] = int(abs(xi_even[-1,0] + xi_odd[-1,1]) <= 2)

        # Status update
        curr += 1
```

```
38          if curr%100 == 0:
39              tp = time.clock()
40              print "%i of %i in %.2f s" % (curr, n, tp-t)
41              t = tp
42  tf = time.clock()
43  print "Finished in %.2f s" % (tf - ti)
44  save("mathieu.npy", array([Q, A, S]))
```

B.2 Stability boundary calculations

An up to date version of this program can be downloaded at https://github.com/mivade/paultrap.

```
1   """
2   paultrap.py - Provides a simple object for calculating stability
3   boundaries for a linear Paul trap.
4
5   This program is free software: you can redistribute it and/or modify
6   it under the terms of the GNU General Public License as published by
7   the Free Software Foundation, either version 3 of the License, or (at
8   your option) any later version.
9
10  This program is distributed in the hope that it will be useful, but
11  WITHOUT ANY WARRANTY; without even the implied warranty of
12  MERCHANTABILITY or FITNESS FOR A PARTICULAR PURPOSE. See the GNU
13  General Public License for more details.
14
15  You should have received a copy of the GNU General Public License
16  along with this program. If not, see <http://www.gnu.org/licenses/>.
17  """
18
19  import numpy
20  import scipy.constants
21
22  q_e = scipy.constants.e
23  amu = scipy.constants.u
24  pi = numpy.pi
25
26  A = [-6.43e-2, 0.5256, -3.23e-3, 0]
27  B = [-1.173, 1.0657]
28  q1, q2 = numpy.arange(0, 0.706, 0.005), numpy.arange(0.706, 0.915, 0.005)
29  q = numpy.append(q1, q2)
30
31  class PaulTrap:
32      def __init__(self, radius, frequency):
33          """Initialize PaulTrap object with radius r0 and frequency f
34          in SI units."""
35          self.r0 = radius
```

```
36          self.Omega = 2*pi*frequency
37
38      def stability_qa(self):
39          """Returns the q, a boundary of stability for the Mathieu
40          equations."""
41          return q, numpy.append(numpy.polyval(A, q1), numpy.polyval(B, q2))
42
43      def stability_VU(self, m, Z=1.):
44          """Returns the Mathieu stability boundary in voltages for mass
45          given in amu and charge in units of e."""
46          q, a = self.stability_qa()
47          V = q*m*amu*self.r0**2*self.Omega**2/(2.*Z*q_e)
48          U = a*m*amu*self.r0**2*self.Omega**2/(4.*Z*q_e)
49          return V, U
50
51      def qa_to_voltage(self, q, a, m, Z=1.):
52          """Return the voltages for given stability parameters. Mass
53          given in amu."""
54          return [q*m*amu*self.r0**2*self.Omega**2/(2.*Z*q_e),
55                  a*m*amu*self.r0**2*self.Omega**2/(4.*Z*q_e)]
56
57      def voltage_to_qa(self, V, U, m, Z=1.):
58          """Returns the stability parameters for given voltages. Mass
59          given in amu."""
60          return [2*Z*q_e*V/(m*amu*self.r0**2*self.Omega**2),
61                  4*Z*q_e*U/(m*amu*self.r0**2*self.Omega**2)]
62
63  if __name__ == "__main__":
64      trap = PaulTrap(3.18e-3, 2.7e6)
65      print trap.stability_qa()
66      print trap.stability_VU(138.)
67      print trap.qa_to_voltage(0.6, 0., 138.)
68      print trap.voltage_to_qa(230., 0., 138.)
```

B.3 Three level system

```
1  from numpy import linspace, save
2  from qutip import *
3  from scipy.integrate import odeint
4
5  hbar = 1
6
7  # Basis states
8  gs = basis(3,0) # ground state
9  es = basis(3,1) # excited state
10 ms = basis(3,2) # metastable state
11
```

```
# Frequencies (units of G1)
G1 = 1 # 1/tau
b10, b12 = 3/4., 1/4. # branching ratios
delta01, delta21 = -2*G1*b12, -1*G1*b10 # detunings
R01, R21 = .01*G1, .01*G1 # Rabi frequencies

# Hamiltonian
H = 0.5*hbar*(R01*gs*dag(es) + R01*es*dag(gs) + \
            -delta01*es*dag(es) + R21*es*dag(ms) + \
            R21*ms*dag(es) + 2*(delta21 - delta01)*ms*dag(ms))

# Collapse operators
C_op_list = [sqrt(b12*G1)*ms*dag(es), sqrt(b10*G1)*gs*dag(es)]

# Expectation values to calculate
exp_list = [gs*dag(gs), es*dag(es), ms*dag(ms)]

# Solve
psi0 = es
t = linspace(0, 10, 1000)
out = mesolve(H, psi0, t, C_op_list, exp_list)

# Rate equation model
G10, G12 = G1*b10, G1*b12

def f(y, t):
    N0 = y[0]
    N1 = y[1]
    N2 = y[2]
    f0 = -N0*R01 + N1*G10
    f1 = N0*R01 - N1*(G10 + G12) + N2*R21
    f2 = -N2*R21 + N1*G12
    return [f0,f1,f2]

# Initial conditions
y0 = [0, 1, 0]

# Solve
rate_out = odeint(f, y0, t)
N = rate_out[:,0], rate_out[:,1], rate_out[:,2]

# Compare
colors = ['b', 'r', 'k']
labels = ["Ground", "Excited", "Metastable"]
plt.figure()
plt.hold(True)
for i in range(3):
```

```
59      plt.plot(t, out.expect[i], colors[i]+'-', label=labels[i])
60  for i in range(3):
61      plt.plot(t, N[i], colors[i]+'--', label=None)
62  plt.hold(False)
63  plt.legend(loc='best')
64  plt.xlabel(r"$t$ $[\Gamma_{2}^{-1}]$")
65  plt.ylabel("Fractional population")
66  plt.show()
67  save("quantum.npy", out.expect)
68  save("rate.npy", N)
69
70  # Higher intensity quantum evolution
71  R01, R21 = 1*G1, 1*G1
72  H = 0.5*hbar*(R01*gs*dag(es) + R01*es*dag(gs) + \
73              -delta01*es*dag(es) + R21*es*dag(ms) + \
74              R21*ms*dag(es) + 2*(delta21 - delta01)*ms*dag(ms))
75  out = mesolve(H, psi0, t, C_op_list, exp_list)
76  plt.figure()
77  plt.hold(True)
78  for i in range(3):
79      plt.plot(t, out.expect[i], colors[i], label=labels[i])
80  plt.hold(False)
81  plt.legend(loc='best')
82  plt.xlabel(r"$t$ $[\Gamma_{2}^{-1}]$")
83  plt.ylabel("Fractional population")
84  plt.show()
85  save("quantum2.npy", out.expect)
```

B.4 Simple ion cooling model

```
1   """
2   simpcool.py
3
4   A crude model of laser cooling of a single ion in a linear Paul
5   trap. The equation of motion for the ion is given by
6
7   .. math::
8
9     m\ddot{\vec{x}} = \vec{F}_l + \vec{F}_t
10
11  where :math:`\vec{F}_l` is the force due to the laser and
12  :math:`\vec{F}_t` is the confining force of the Paul trap.
13  """
14
15  from numpy import *
16  from numpy.random import uniform, normal
17  from numpy.linalg import norm
18  import scipy.constants
```

```
19 import matplotlib.pyplot as plt
20
21 # Constants
22 hbar = scipy.constants.hbar
23 Ze = scipy.constants.e
24 kB = scipy.constants.k
25
26 # Simulation parameters
27 m = 138*scipy.constants.u
28 Gamma = 2*pi*15e6
29 delta = -2*Gamma
30 k = 2*pi/(493e-9)
31 khat = 1
32 s0 = 2.
33 r0 = 3.18e-3
34 z0 = 25.4e-3/2.
35 kappa = 5e-5
36 Omega = 2*pi*3.0e6
37 V, UEC = 250., 300.
38 A, B = kappa*UEC/z0**2, 2*Ze*V**2/(m*Omega**2*r0**4)
39 wz = sqrt(2*Ze*A/m)
40 fz = wz/2/pi
41 T = 1/fz
42 print 'fz =', fz/1e3, 'kHz'
43
44 # Forces
45 def F_t(x, t):
46     F = -2*Ze*A*x
47     return F
48
49 def F_l(v, t):
50     delta_ = delta - dot(k*khat, v)
51     F = hbar*k*khat*s0*Gamma/2./(1 + s0 + (2*delta_/Gamma)**2)
52     return F
53
54 # Simulation
55 dt, t_max = 1e-6, 10e-3
56 t = arange(0, t_max, dt)
57 T0 = 298
58 x, v = zeros(len(t)), zeros(len(t))
59 v0 = normal(0, sqrt(kB*T0/m/3.))
60 x0 = normal(0, z0)
61 v[0] = v0
62 x[0] = x0
63 for i in range(1,len(t)):
64     v[i] = v[i-1] + (F_t(x[i-1], t[i]) + F_l(v[i-1], t[i]))*dt/m
65     x[i] = x[i-1] + v[i]*dt
```

```
66 save("trajectory.npy", [x,v])
67 plt.figure()
68 plt.plot(t/1e-3, x/1e-3)
```

B.5 IonMD

The full code from the ion molecular dynamics simulation (IonMD) is available online at https://github.com/mivade/IonMD.

Appendix C

DATA TABLES

This Appendix contains a compilation of data used for estimates and calculations throughout this thesis as well as miscellaneous data which may occasionally prove useful.

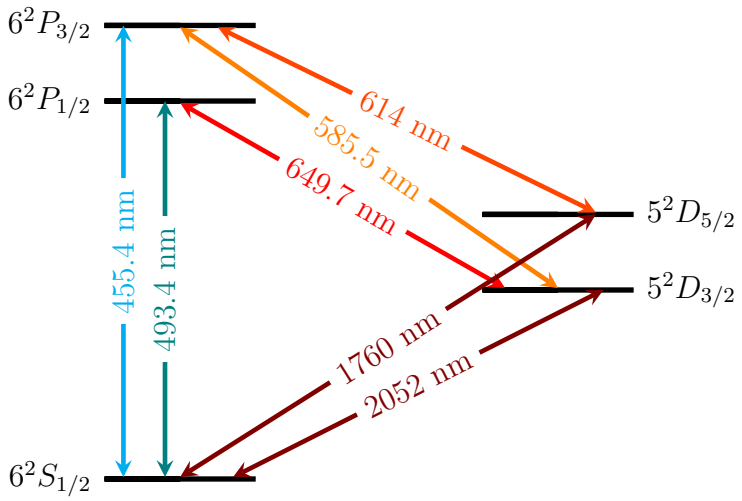

Figure C.1: Extended Ba^+ level structure and wavelengths [228].

Table C.1: Naturally occurring isotopes of barium and their properties. Natural abundances (NA) are given in percent, masses in amu, and half-lives in years [229, 230].

Isotope	Mass	NA	$\tau_{1/2}$
138	137.905	71.7	—
137	136.906	11.23	—
136	135.905	7.854	—
135	134.905	6.592	—
134	133.905	2.417	—
132	131.905	0.101	$> 3 \times 10^{20}$
130	129.906	0.106	$0.5–2.7 \times 10^{21}$

Table C.2: Isotope shifts in MHz for $S \leftrightarrow P$ cycling transitions of $^{13x}Ba^+$ relative to $^{138}Ba^+$ [231].

Isotope	$6^2S_{1/2} \leftrightarrow 6^2P_{1/2}$	$6^2S_{1/2} \leftrightarrow 6^2P_{3/2}$
137	271.1(1.7)	279.0(2.6)
136	179.4(1.8)	186.9(2.1)
135	348.6(2.1)	360.7(2.2)
134	222.6(3.0)	233.9(3.7)
132	278.9(4.0)	294.9(4.2)
130	353.3(4.4)	372.3(4.9)

Table C.3: Data on the naturally-occurring isotopes of thorium. ^{232}Th is the primary isotope of Th, with the rest listed existing in only trace amounts [229, 230]. Listed here are the nuclear spins (I), half-lives ($\tau_{1/2}$) in years (unless otherwise specified), primary decay modes (DM), decay energies (DE) in MeV, and decay products (DP). Note that the nuclear spin for ^{229}Th is 3/2 in the metastable isomer state rather than 5/2 listed here for the nuclear ground state.

Isotope	228	229	230	231	232	234
I	0	5/2	0	5/2	0	0
$\tau_{1/2}$	1.9116	7340	75380	25.5 h	1.405×10^{10}	24.1 d
DM	α	α	α	β^-	α	β^-
DE	5.520	5.168	4.770	0.39	4.083	0.27
DP	^{224}Ra	^{225}Ra	^{226}Ra	^{231}Pa	^{228}Ra	^{234}Pa

Table C.4: Approximate mass to charge ratios in amu of ions relevant to this work.

Ion	m/Z
CH_3^+	15
SF_5^+	127
Ba^+	138
BaH^+, BaH_2^+, BaH_3^+	139, 140, 141
SF_6^+	146
BaC^+	150
$BaCH^+$, $BaCH_2^+$, $BaCH_3^+$	151, 152, 153
BaO^+	154
BaF^+	157
BaS^+	170
$BaCl^+$	173 or 175
BaF_2^+	176
Th^+	232
Th^{2+}	116
Th^{3+}	77.3

Table C.5: Dissociation energies in eV relevant to this work with uncertainties listed where available [209].

Bond	D_0
Ba–H	1.8(2)
Ba–O	5.8(1)
Ba–F	6.08(7)
Ba–Cl	4.52(9)
Ba–Br	3.76(9)
Ba–I	3.32(7)
F–F	1.6
Cl–Cl	2.5
Br–Br	2.0
I–I	1.6
H–F	5.9
H–Cl	4.5
H–Br	3.8
H–I	3.1
S–F	3.55(5)
C–F	5.7
C–Cl	4.1(3)
O=O	5.165(2)

Table C.6: Ionization energies in eV for atoms and molecules of interest in this work using data from Refs. [93, 208, 218].

Atom/molecule	IE
F	17.4
F_2	15.7
Cl	13.0
Cl_2	11.5
Br	11.8
Br_2	10.5
I	10.5
I_2	9.3
SF_6	15.3
CH_3Cl	11.3
Ba	5.2
BaH	5.2
BaO	6.9
BaF	4.9
BaCl	5.0
BaBr	4.8
BaI	4.7

Appendix D

STANFORD SR560 REPLACEMENT CIRCUIT

Using techniques such as the Pound-Drever-Hall method to generate error signals for stabilizing lasers typically results in small signals which require amplification and filtering before being sent to a PID controller for feedback control. A good off the shelf solution for both filtering and amplification is the Stanford Research Systems SR560 low noise preamplifier which features switchable gain and filter cutoffs. The primary disadvantage to this is the unit cost. To address this issue, a similar circuit was designed and built to be used as a drop in replacement for the SR560. The preamp circuit was designed by following the block diagram layout provided by SRS in the SR560 manual [232]. The circuit consists of four op amps and two RC filtering stages to provide gain of up to 5000 and a rolloff of 12 dB/octave. Care should be taken with grounding the circuit in order to avoid introducing ground loops.

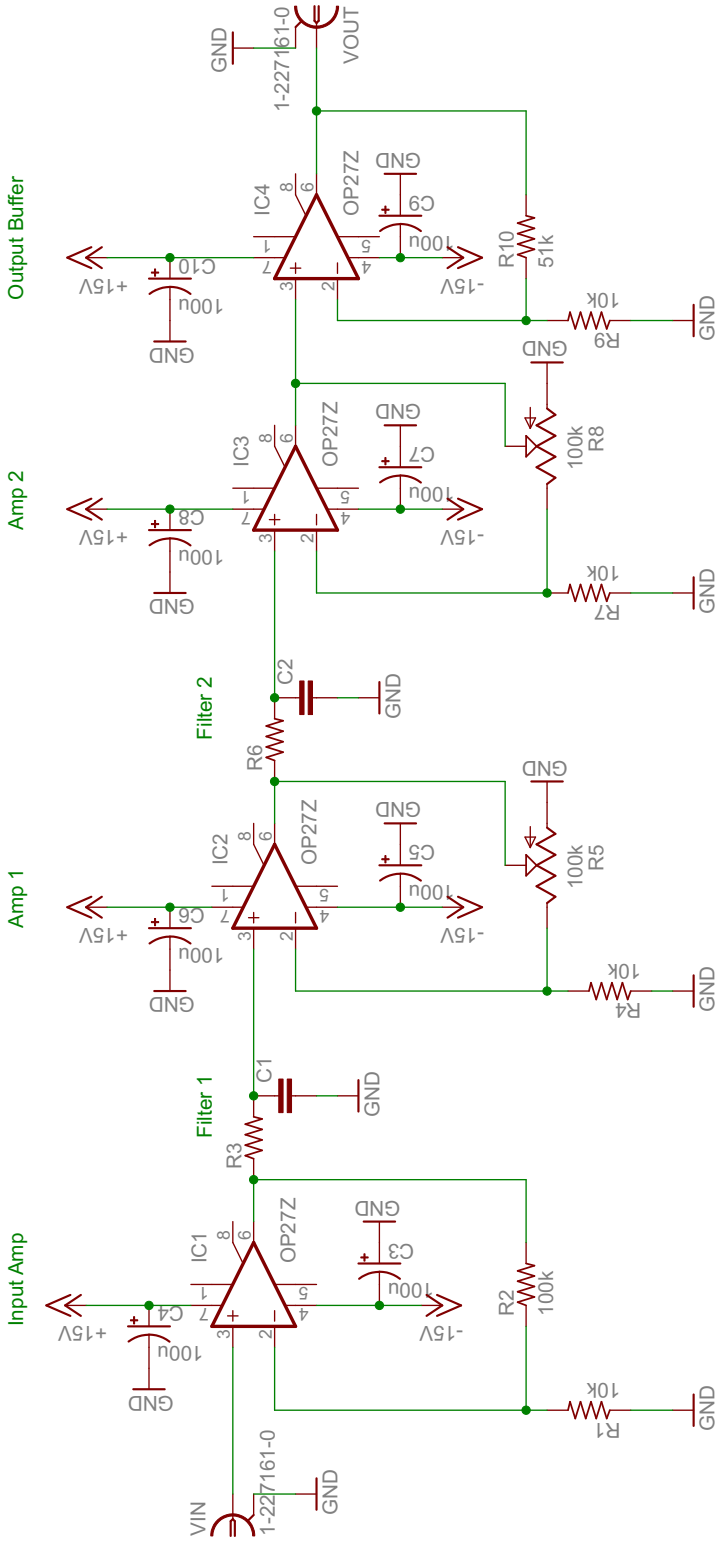

Figure D.1: Schematic of the SRS SR560 replacement circuit. This circuit follows a similar scheme to that described in the SR560 manual. The input stage (Input Amp) gives a fixed gain of 10, followed by the first RC filter. A variable gain amplification stage (Amp 1) is followed by a second RC filter to give 12 dB/octave rolloff (omitting this second RC filter would give 6 dB/octave rolloff if desired). The signal is then further amplified with a second variable gain amplifier (Amp 2) and a fixed output buffering stage (Output Buffer) of gain 5. As configured here, each variable gain stage can add up to a gain of 10 so that the total gain has a maximum value of 5000.

Table D.1: Part list for the preamp circuit. The filter resistors and capacitors (R3, C1, R6, and C2) are unspecified in the schematic since different applications may require different cutoffs. The values listed below for the RC filter stages result in a cutoff of about 3 kHz, which was chosen by optimizing error signals in a test setup first with the SR560.

Part	Value/Part Number	Comment
R1	10k	Input amp gain
R2	100k	Input amp gain
R3	56k	Filter 1 resistor
R4	10k	Amp 1 gain
R5	100k	Trimpot, Amp 1 gain
R6	56k	Filter 2 resistor
R7	10k	Amp 2 gain
R8	100k	Trimpot, Amp 2 gain
R9	10k	Output buffer gain
R10	51k	Output buffer gain
C1	1000 pF	Filter 1 capacitor, ceramic
C2	1000 pF	Filter 2 capacitor, ceramic
C3–C10	100 μF	Isolation capacitor, electrolytic
IC1	OP27E	Input amplifier
IC2	OP27E	Amplification stage 1
IC3	OP27E	Amplification stage 2
IC4	OP27E	Output buffer amplifier

Appendix E

BARIUM LASERS

Ba^+, being only singly ionized, is both easier to produce and easier to keep around for long enough to do interesting science with than Th^{3+}. Furthermore, the main transitions involved (Figure C.1) have large natural linewidths and are all visible, meaning detection is considerably easier and laser stabilization is less critical. The scheme chosen for laser cooling and detection relies on the $S_{1/2} \leftrightarrow P_{1/2}$ and $D_{3/2} \leftrightarrow P_{1/2}$ transitions at 493 nm and 650 nm, respectively. Unfortunately, generating light at each of these wavelengths presents its own unique set of complications. This appendix describes methods to address these challenges.

E.1 Cold laser housing

The Ba^+ $P_{1/2} \leftrightarrow D_{3/2}$ transition is conveniently located at about 650 nm, which is coincidentally the same wavelength as specified for reading DVDs[1] [233]. However, in practice, most commercially available diodes that are sold as 650 nm laser diodes are typically centered closer to 655 nm or even longer. In addition to tuning the wavelength in an extended cavity diode laser setup, it is usually necessary to significantly lower the temperature of the laser diode in order to reach the transition wavelength for Ba^+. As the relationship between temperature and wavelength for AlGaInP laser diodes is typically on the order of 0.1 nm per degree centigrade, significant cooling is required and so precautions must be taken against condensation.

To reach low temperatures and combat condensation, several generations of ECDL cold boxes were constructed. The final, most successful generation is described here. Design

[1] Unfortunately for Ba^+ ion trappers, with the advent of the Blu-ray standard, many 650 nm band laser diodes are being discontinued by manufacturers, making good, inexpensive 650 nm diodes harder find.

characteristics were inspired by Refs. [128, 234]. An independent design similar to the one described here can be found in Ref. [235]. The general scheme is as follows: A housing for the laser diode and its collimation optic are mounted on a ¼" thick aluminum plate. A grating is epoxied onto an aluminum block cut with a 45 degree angle which is itself epoxied onto a ½" mirror mount secured by a screw onto the aluminum cold plate. Strategic hole placement on the aluminum plate allow it to be screwed into a large aluminum heatsink with two thermoelectric coolers (TECs) sandwiched in between. The entire housing is then surrounded with clear acrylic walls which have holes drilled in them for access to the mirror mount adjustment knobs for coarse tuning of the wavelength and feedback optimization to the laser diode. A third hole sealed with an AR coated window allows for the beam to exit the cold box. Electrical connections are made with bulkhead BNC connectors screwed into the acrylic walls where convenient. Each wall seam is sealed either with electrical tape or with silicone to serve as a barrier to moisture. The mirror mount access holes are covered with electrical tape when not in use and the whole assembly is flushed with either nitrogen or argon gas whenever these holes are exposed[2]. Prior to sealing the cold box with a lid, some desiccant is added to absorb any residual moisture not flushed out by the inert gas.

The procedure for getting a 650 nm laser diode on transition is as follows. First, with the acrylic housing lid removed and the TECs set to near room temperature, the laser diode is collimated and feedback is optimized using a 2400 lines/mm grating. The wavelength can be adjusted by turning the horizontal knob of the grating mount, though with most 650 nm diodes, the edge of the gain profile will be several THz away from transition. With freshly baked desiccant placed in the laser housing, the acrylic lid is replaced and sealed with silicone adhesive sealant and a low flow of N_2 or Ar gas is purged through the housing for several minutes to flush out atmospheric moisture. The temperature is then lowered a few degrees and the feedback to the laser diode is adjusted. This step is repeated until the

[2]It was found that using argon instead of nitrogen prolonged the length of time before needing to open and clean out the cold box. This was presumably related to argon being heavier than air.

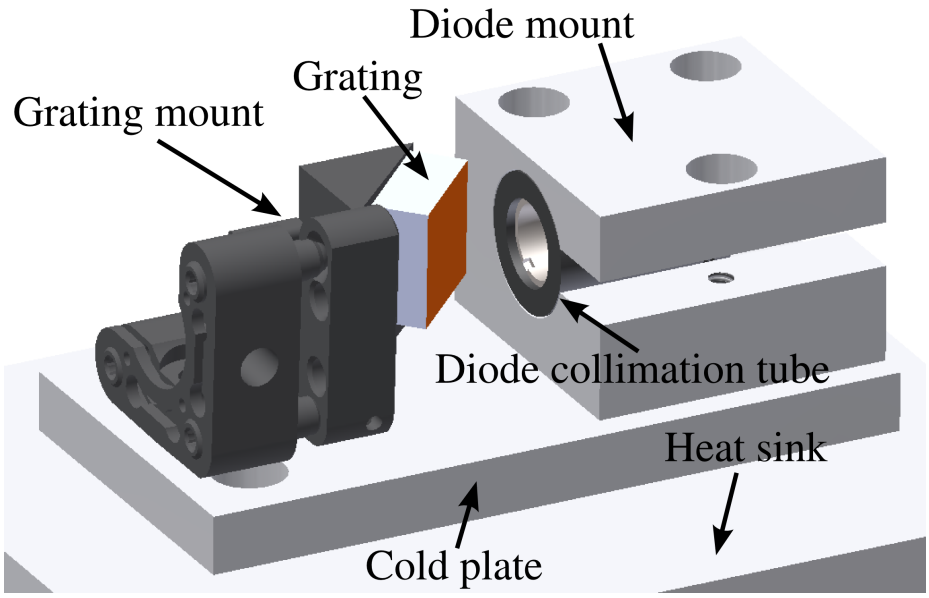

Figure E.1: An overview of the cold laser housing layout.

laser is near transition. At this point, it is a matter of adjusting the horizontal grating knob and the temperature until the correct wavelength can be reached with the PZT and current adjustments.

E.2 Toptica SHG 100 user's guide

At present, laser diodes which emit at the blue wavelength needed for laser cooling and fluorescence of Ba^+ ions are not readily available[3]. Instead, the most common technique for generating 493 nm light is to use a nonlinear optical crystal to double the frequency using SHG since high power laser diode sources at the fundamental wavelength of 986 nm are abundant and inexpensive. This section describes how to use and maintain the Toptica SHG 100 system[4]. The procedures outlined here have been developed through discussions with colleagues and Toptica service personnel.

[3] A few manufacturers are no producing laser diodes centered at 488 nm which could presumably be heated enough to reach 493 nm. However, these diodes are extremely expensive compared to near infrared laser diodes, and since heating a diode decreases its lifetime, a SHG setup remains much more financially practical.

[4] Toptica has long since upgraded their standard second harmonic generation system to the SHG 110. The principles of operation are mostly the same, the main differences between the two models being various system improvements in the SHG 110.

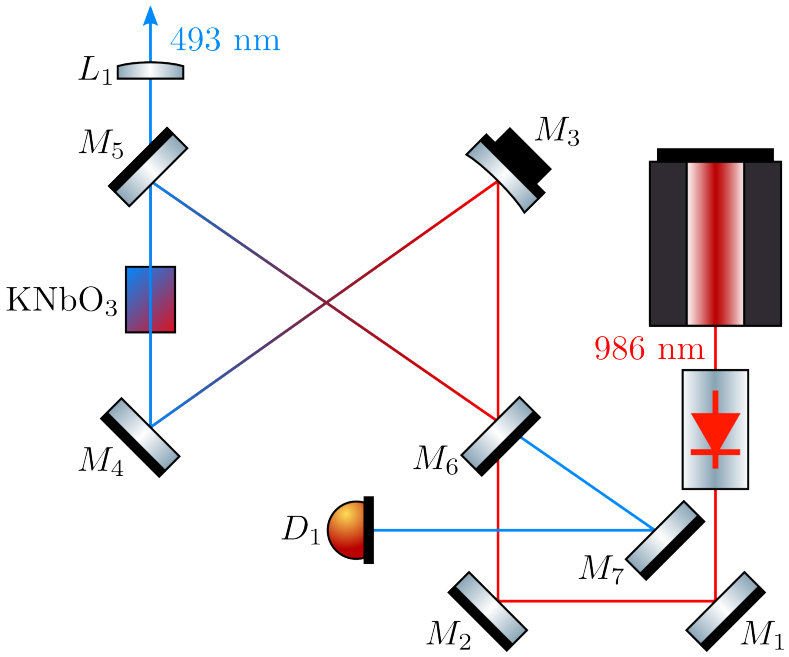

Figure E.2: The layout of the SHG cavity optics. Incoming light at 986 nm is injected into a bow tie cavity using the incoupling mirrors M_1 and M_2. Placed between cavity mirrors M_4 and M_5 is a KNbO3 crystal which doubles the frequency of the fundamental beam in order to generate the 493 nm light required for fluorescence and laser cooling of Ba^+.

E.2.1 Aligning the Cavity

See Figure E.2 for mirror labels. **Caution:** In order to prevent damage to the $KNbO_3$ crystal, its temperature must not change too rapidly. If the crystal is being removed or replaced, the temperature set point must be gradually adjusted to room temperature. The SHG-100 manual recommends temperature adjustments no more quickly than about 1°C per minute. In practice, a good rule of thumb is toadjust by 0.1° at a time and then wait for thermal equilibrium to be reached before making further adjustments.

E.2.1.1 Initial alignment

1. Make sure the crystal mount is secured near the left-most possible position when facing the direction of propagation through the $KNbO_3$ crystal.

2. With M_6 removed, use the incoupling mirrors (M_1 and M_2) to center the pump beam on the cavity mirror M_3.

3. Adjust M_3 to center the fundamental beam on M_4.

4. With M_5 removed, adjust M_4 and the crystal position such that the pump beam passes through the $KNbO_3$ crystal and is centered on the output lens L_1.

5. Replace M_5 and adjust it to center the pump beam on M_6.

6. Adjust M_6 so that the reflected beam overlaps with the incoming beam. Cavity modes should now be detected on the photodiode behind M_4.

7. Maximize the cavity signal with M_6.

E.2.1.2 Peaking up the alignment

Following initial cavity alignment, many higher order cavity modes will be present. These extraneous modes must be suppressed for maximum power at the doubled wavelength. The next step is fine tuning to maximize transmission of the TEM_{00} mode.

1. Pick an axis (horizontal or vertical).

2. Adjust the alignment of M_4 and M_5 on the chosen axis.

3. Adjust the alignment of M_5 and M_6 on the chosen axis.

4. Adjust the alignment of M_6 and M_3 on the chosen axis.

5. Adjust the alignment of M_3 and M_4 on the chosen axis.

6. Adjust the incoupling mirrors M_1 and M_2 until the mode suppression is optimized.

7. Switch to the other axis and repeat the procedure until higher order modes are suppressed.

E.2.2 Locking the cavity

Once the cavity signal is peaked up, adjust M_7 such that the beam hits the center of detector D_1. This is most easily done by first coarse tuning by loosening the bolt holding the mirror in place and then fine tuning with the adjustment knobs of M_7. Depending on the total amount of power, it may be necessary to slightly attenuate the light hitting D_1 with a piece of thin paper.

The error signal is adjusted with the Pound-Drever-Hall module (PDD-110). At the time of this writing, the settings are:

- Amplitude: 1
- Gain: 1.5
- Phase: 4

These settings, with a signal level of about 3 V, results in an error signal with peak to peak voltage of about 80 mV. To lock the cavity using the PID-110 module, first turn the `monitor` knob to `min int` (minimum intensity) and verify the cavity signal is above this level. Turn `monitor` back to `err` and center the error signal using the `set point` trimpot. Zero the P, I, and D trimpots and set the overall gain to the midpoint of its range. The sign should be adjusted appropriatley for the error signal you have (`pos` for a falling edge and `neg` for a rising edge). Attempt to lock the cavity by turning the `reg` switch on and the `mod in` switch off. The I, P, and D trimpots should then be adjusted respectively to get a good lock. While the cavity is locked, the set point should be tweaked to maximize output power (while still retaining a good lock signal).

E.2.3 Maximizing doubled power

The first step in maximizing the blue power is phase matching the crystal. This is done by *slowly* adjusting the temperature. With the cavity locked, place a power meter after the

cavity output[5]. Slowly adjust the temperature until the power is maximized. To maintain output power, the procedure of Section E.2.1.2 should be repeated, but with using a power meter on the doubled light instead of monitoring the signal from the photodiode behind M_4. Oftentimes, it is only necessary to tweak cavity mirrors M_5 and M_6 and the incoupling mirrors M_1 and M_2 to peak up the power. From time to time, the cavity mirrors should be cleaned with acetone to maintain good coupling of the fundamental light into the cavity.

[5] Although the peaks detected on the detector behind M_4 could in principle be used for maximizing power, the detector surface area is too small to use as a reliable power meter.

Appendix F

APD QUANTUM EFFICIENCY

Silicon APDs with single photon resolution can exhibit very low noise and high quantum efficiency. For the APD used for the measurements in Chapter 5, the manufacturer quotes a photon detection efficiency of between 55 and 70% for 650 nm light. In order to measure the actual efficiency at a given wavelength, the following procedure is used for fiber coupled APDs. This procedure assumes general familiarity in using APDs and getting them setup properly.

1. Set up a half-wave plate and a polarizing beamsplitter cube (PBS) where convenient along the optical path of a laser at the wavelength of interest.

2. Picking either the *s*- or *p*-polarized beam after the PBS and orienting the half-wave plate such that the power in the chosen polarization is maximized, fiber couple light into a single mode fiber and measure the transmitted power using a well-calibrated optical power meter.

3. Fix a neutral density filter of OD4 or greater to the fiber coupler input and measure the attenuated power. The precise attenuation of the ND filter is now known.

4. Removing the ND filter, decrease the amount of light reaching the power meter until it reads just above background.

5. Replace the ND filter. Remove the fiber from the power meter and connect it to the APD.

6. Power the APD and measure the number of counts per some unit time Δt.

With knowledge of the precise attenuation, the optical power incident on the detector is well known and related to the number of photons N_γ by

$$P = \frac{E}{\Delta t} = \frac{N_\gamma hc}{\lambda \Delta t}. \tag{F.1}$$

The expected N_γ can then be compared to the measured number of photons in order to determine the actual quantum efficiency at the wavelength λ.

REFERENCES

[1] S. Robertson and R. Younger, "Coulomb crystals of oil droplets," *Am. J. Phys.* **67**, 310 (1999).

[2] S. V. Kulkarni and A. Sen, "Interfacial Instability Triggered Coulomb Crystallization of Charged Water Droplets," *Phys. Rev. Lett.* **93**, 014501 (2004).

[3] D. Offenberg, C. Wellers, C. B. Zhang, B. Roth, and S. Schiller, "Measurement of small photodestruction rates of cold, charged biomolecules in an ion trap," *J. Phys. B: At., Mol. Opt. Phys.* **42**, 035101 (2009).

[4] S. Joseph, W. Guan, M. A. Reed, and P. S. Krstic, "A long DNA segment in a linear nanoscale Paul trap," *Nanotechnology* **21**, 015103 (2010).

[5] W. Neuhauser, M. Hohenstatt, P. E. Toschek, and H. Dehmelt, "Localized visible Ba^+ mono-ion oscillator," *Phys. Rev. A* **22**, 1137 (1980).

[6] G. Janik, W. Nagourney, and H. Dehmelt, "Doppler-free optical spectroscopy on the Ba^+ mono-ion oscillator," *Journal of the Optical Society of America B* **2**, 1251 (1985).

[7] R. S. Van Dyck, P. B. Schwinberg, and H. G. Dehmelt, "New high-precision comparison of electron and positron g factors," *Phys. Rev. Lett.* **59**, 26 (1987).

[8] D. J. Douglas, A. J. Frank, and D. Mao, "Linear ion traps in mass spectrometry," *Mass Spectrom. Rev.* **24**, 1–29 (2005).

[9] C. W. Chou, D. B. Hume, J. C. J. Koelemeij, D. J. Wineland, and T. Rosenband, "Frequency Comparison of Two High-Accuracy Al^+ Optical Clocks," *Phys. Rev. Lett.* **104**, 070802 (2010).

[10] C. W. Chou, D. B. Hume, T. Rosenband, and D. J. Wineland, "Optical Clocks and Relativity," *Science* **329**, 1630 (2010).

[11] E. R. Meyer, J. L. Bohn, and M. P. Deskevich, "Candidate molecular ions for an electron electric dipole moment experiment," *Phys. Rev. A* **73**, 062108 (2006).

[12] M. N. Portela, J. E. v. d. Berg, H. Bekker, O. Böll, E. A. Dijck, G. S. Giri, S. Hoekstra, K. Jungmann, A. Mohanty, C. J. G. Onderwater, B. Santra, S. Schlesser, R. G. E. Timmermans, O. O. Versolato, L. W. Wansbeek, L. Willmann, and H. W. Wilschut, "Towards a precise measurement of atomic parity violation in a single Ra^+ ion," *Hyperfine Interact.* **214**, 157 (2013).

[13] D. Kielpinski, C. Monroe, and D. J. Wineland, "Architecture for a large-scale ion-trap quantum computer," *Nature* **417**, 709 (2002).

[14] H. Häffner, C. F. Roos, and R. Blatt, "Quantum computing with trapped ions," *Phys. Rep.* **469**, 155 (2008).

[15] R. Blatt and C. F. Roos, "Quantum simulations with trapped ions," *Nat. Phys.* **8**, 277 (2012).

[16] R. Islam, C. Senko, W. C. Campbell, S. Korenblit, J. Smith, A. Lee, E. E. Edwards, C.-C. J. Wang, J. K. Freericks, and C. Monroe, "Emergence and Frustration of Magnetism with Variable-Range Interactions in a Quantum Simulator," *Science* **340**, 583 (2013).

[17] B. Roth, P. Blythe, H. Wenz, H. Daerr, and S. Schiller, "Ion-neutral chemical reactions between ultracold localized ions and neutral molecules with single-particle resolution," *Phys. Rev. A* **73**, 042712 (2006).

[18] M. T. Bell, A. D. Gingell, J. M. Oldham, T. P. Softley, and S. Willitsch, "Ion-molecule chemistry at very low temperatures: cold chemical reactions between Coulomb-crystallized ions and velocity-selected neutral molecules," *Faraday Discuss.* **142**, 73 (2009).

[19] A. D. Gingell, M. T. Bell, J. M. Oldham, T. P. Softley, and J. N. Harvey, "Cold chemistry with electronically excited Ca^+ Coulomb crystals," *J. Chem. Phys.* **133**, 194302 (2010).

[20] F. H. Hall, P. Eberle, G. Hegi, M. Raoult, M. Aymar, O. Dulieu, and S. Willitsch, "Ion-neutral chemistry at ultralow energies: dynamics of reactive collisions between laser-cooled Ca+ ions and Rb atoms in an ion-atom hybrid trap," *Mol. Phys.* , 1 (2013).

[21] E. Peik, G. Hollemann, and H. Walther, "Laser cooling and quantum jumps of a single indium ion," *Phys. Rev. A* **49**, 402–408 (1994).

[22] T. Rosenband, P. O. Schmidt, D. B. Hume, W. M. Itano, T. M. Fortier, J. E. Stalnaker, K. Kim, S. A. Diddams, J. C. J. Koelemeij, J. C. Bergquist, and D. J. Wineland, "Observation of the $^1S_0 \rightarrow ^3P_0$ Clock Transition in $^{27}Al^+$," *Phys. Rev. Lett.* **98**, 220801 (2007).

[23] Wikimedia Commons, "File:Periodic Table Armtuk3.svg," 2007.

[24] M. S. Wickleder, B. Fourest, and P. K. Dorhout, "Thorium,", in *The Chemistry of the Actinide and Transactinide Elements*, edited by L. R. Morss, N. M. Edelstein, and J. Fuger pp. 52–160 Springer Netherlands 2011.

[25] J. Allen, R. Benz, R. Förthmann, A. Naoumidis, D. Pemberton, and H. Vietzke, "Technology, Uses, Irradiated Fuel, Reprocessing,", in *Gmelin Handbook of Inorganic Chemistry*, edited by R. Keim and C. Keller volume A3 of *Gmelin Handbook of Inorganic Chemistry* Springer Verlag Berlin , 8 ed. 1988.

[26] J. J. McKetta, editor, *Encyclopedia of Chemical Processing and Design* (CRC Press, 1996).

[27] T. Kamei and S. Hakami, "Evaluation of implementation of thorium fuel cycle with LWR and MSR," *Progress in Nuclear Energy* **53**, 820 (2011).

[28] S. F. Ashley, G. T. Parks, W. J. Nuttall, C. Boxall, and R. W. Grimes, "Nuclear energy: Thorium fuel has risks," *Nature* **492**, 31 (2012).

[29] E. Peik and C. Tamm, "Nuclear laser spectroscopy of the 3.5 eV transition in Th-229," *Europhys. Lett.* **61**, 181 (2003).

[30] C. J. Campbell, A. G. Radnaev, A. Kuzmich, V. A. Dzuba, V. V. Flambaum, and A. Derevianko, "Single-Ion Nuclear Clock for Metrology at the 19th Decimal Place," *Phys. Rev. Lett.* **108**, 120802 (2012).

[31] V. V. Flambaum, "Enhanced Effect of Temporal Variation of the Fine Structure Constant and the Strong Interaction in ^{229}Th," *Phys. Rev. Lett.* **97**, 092502 (2006).

[32] J. C. Berengut, V. A. Dzuba, V. V. Flambaum, and S. G. Porsev, "Proposed Experimental Method to Determine alpha Sensitivity of Splitting between Ground and 7.6 eV Isomeric States in ^{229}Th," *Phys. Rev. Lett.* **102**, 210801 (2009).

[33] A. Hayes and J. Friar, "Sensitivity of nuclear transition frequencies to temporal variation of the fine structure constant or the strong interaction," *Phys. Lett. B* **650**, 229 (2007).

[34] X.-t. He and Z.-z. Ren, "Enhanced sensitivity to variation of fundamental constants in the transitions of ^{229}Th and ^{249}Bk," *J. Phys. G: Nucl. Part. Phys.* **34**, 1611 (2007).

[35] X.-t. He and Z.-z. Ren, "Temporal variation of the fine structure constant and the strong interaction parameter in the ^{229}Th transition," *Nucl. Phys. A* **806**, 117 (2008).

[36] L. Kroger and C. Reich, "Features of the low-energy level scheme of ^{229}Th as observed in the α-decay of ^{233}U," *Nucl. Phys. A* **259**, 29 (1976).

[37] D. G. Burke, P. E. Garrett, T. Qu, and R. A. Naumann, "Additional evidence for the proposed excited state at $\leq$5 eV in ^{229}Th," *Phys. Rev. C* **42**, R499 (1990).

[38] R. G. Helmer and C. W. Reich, "An excited state of ^{229}Th at 3.5 eV," *Phys. Rev. C* **49**, 1845–1858 (1994).

[39] E. Browne, E. B. Norman, R. D. Canaan, D. C. Glasgow, J. M. Keller, and J. P. Young, "Search for decay of the 3.5-eV level in ^{229}Th," *Phys. Rev. C* **64**, 014311 (2001).

[40] B. R. Beck, J. A. Becker, P. Beiersdorfer, G. V. Brown, K. J. Moody, J. B. Wilhelmy, F. S. Porter, C. A. Kilbourne, and R. L. Kelley, "Energy Splitting of the Ground-State Doublet in the Nucleus ^{229}Th," *Phys. Rev. Lett.* **98**, 142501 (2007).

[41] X. Zhao, Y. N. Martinez de Escobar, R. Rundberg, E. M. Bond, A. Moody, and D. J. Vieira, "Observation of the Deexcitation of the ^{229m}Th Nuclear Isomer," *Phys. Rev. Lett.* **109**, 160801 (2012).

[42] E. Peik and K. Zimmermann, "Comment on 'Observation of the Deexcitation of the ^{229m}Th Nuclear Isomer'," *Phys. Rev. Lett.* **111**, 018901 (2013).

[43] S. G. Porsev, V. V. Flambaum, E. Peik, and C. Tamm, "Excitation of the Isomeric ^{229m}Th Nuclear State via an Electronic Bridge Process in ^{229}Th^{+}," *Phys. Rev. Lett.* **105**, 182501 (2010).

[44] O. A. Herrera-Sancho, M. V. Okhapkin, K. Zimmermann, C. Tamm, E. Peik, A. V. Taichenachev, V. I. Yudin, and P. Głowacki, "Two-photon laser excitation of trapped ^{232}Th^{+} ions via the 402-nm resonance line," *Phys. Rev. A* **85**, 033402 (2012).

[45] W. G. Rellergert, D. DeMille, R. R. Greco, M. P. Hehlen, J. R. Torgerson, and E. R. Hudson, "Constraining the Evolution of the Fundamental Constants with a Solid-State Optical Frequency Reference Based on the ^{229}Th Nucleus," *Phys. Rev. Lett.* **104**, 200802 (2010).

[46] W.-T. Liao, S. Das, C. H. Keitel, and A. Pálffy, "Coherence-Enhanced Optical Determination of the ^{229}Th Isomeric Transition," *Phys. Rev. Lett.* **109**, 262502 (2012).

[47] G. A. Kazakov, A. N. Litvinov, V. I. Romanenko, L. P. Yatsenko, A. V. Romanenko, M. Schreitl, G. Winkler, and T. Schumm, "Performance of a ^{229}Th solid-state nuclear clock," *New J. Phys.* **14**, 083019 (2012).

[48] M. P. Hehlen, R. R. Greco, W. G. Rellergert, S. T. Sullivan, D. DeMille, R. A. Jackson, E. R. Hudson, and J. R. Torgerson, "Optical spectroscopy of an atomic nucleus: Progress toward direct observation of the ^{229}Th isomer transition," *J. Lumin.* **133**, 91 (2013).

[49] C. J. Campbell, A. V. Steele, L. R. Churchill, M. V. DePalatis, D. E. Naylor, D. N. Matsukevich, A. Kuzmich, and M. S. Chapman, "Multiply Charged Thorium Crystals for Nuclear Laser Spectroscopy," *Phys. Rev. Lett.* **102**, 233004 (2009).

[50] C. J. Campbell, A. G. Radnaev, and A. Kuzmich, "Wigner Crystals of ^{229}Th for Optical Excitation of the Nuclear Isomer," *Phys. Rev. Lett.* **106**, 223001 (2011).

[51] C. J. Campbell, *Trapping, Laser Cooling, and Spectroscopy of Thorium IV*, PhD thesis Georgia Institute of Technology 2011.

[52] P. F. A. Klinkenberg, "Spectral structure of trebly ionized thorium, Th IV," *Physica B+C* **151**, 552 (1988).

[53] M. S. Safronova and U. I. Safronova, "Relativistic many-body calculation of energies, oscillator strengths, transition rates, lifetimes, polarizabilities, and quadrupole moment of Fr-like Th IV ion," *arXiv:1304.0158* (2013).

[54] D. J. Wineland, R. E. Drullinger, and F. L. Walls, "Radiation-Pressure Cooling of Bound Resonant Absorbers," *Phys. Rev. Lett.* **40**, 1639 (1978).

[55] W. Neuhauser, M. Hohenstatt, P. Toschek, and H. Dehmelt, "Optical-Sideband Cooling of Visible Atom Cloud Confined in Parabolic Well," *Phys. Rev. Lett.* **41**, 233 (1978).

[56] W. Neuhauser, M. Hohenstatt, P. Toschek, and H. Dehmelt, "Optical-Sideband Cooling of Visible Atom Cloud Confined in Parabolic Well," *Phys. Rev. Lett.* **41**, 233 (1978).

[57] J. J. Bollinger, J. D. Prestage, W. M. Itano, and D. J. Wineland, "Laser-Cooled-Atomic Frequency Standard," *Phys. Rev. Lett.* **54**, 1000–1003 (1985).

[58] A. A. Madej and J. D. Sankey, "Single, trapped Sr^+ atom: laser cooling and quantum jumps by means of the $4d^2D_{5/2}$–$5s^2S_{1/2}$ transition," *Opt. Lett.* **15**, 634 (1990).

[59] S. Urabe, H. Imajo, K. Hayasaka, and M. Watanabe, "Trapping of Ca^+ Ions and Optical Detection," *Japanese Journal of Applied Physics* **30**, L1532 (1991).

[60] G. S. Giri, O. O. Versolato, J. E. van den Berg, O. Böll, U. Dammalapati, D. J. van der Hoek, K. Jungmann, W. L. Kruithof, S. Müller, M. Nuñez Portela, C. J. G. Onderwater, B. Santra, R. G. E. Timmermans, L. W. Wansbeek, L. Willmann, and H. W. Wilschut, "Isotope shifts of the $6d^2D_{3/2} - 7p^2P_{1/2}$ transition in trapped short-lived $^{209-214}Ra^+$," *Phys. Rev. A* **84**, 020503 (2011).

[61] O. O. Versolato, L. W. Wansbeek, G. S. Giri, J. E. v. d. Berg, D. J. v. d. Hoek, K. Jungmann, W. L. Kruithof, C. J. G. Onderwater, B. K. Sahoo, B. Santra, P. D. Shidling, R. G. E. Timmermans, L. Willmann, and H. W. Wilschut, "Atomic parity violation in a single trapped radium ion," *Hyperfine Interact.* **199**, 9 (2011).

[62] B. E. A. Saleh and M. C. Teich, *Fundamentals of Photonics* (Wiley-Interscience, New York, 1991).

[63] J. B. Wübbena, S. Amairi, O. Mandel, and P. O. Schmidt, "Sympathetic cooling of mixed-species two-ion crystals for precision spectroscopy," *Phys. Rev. A* **85**, 043412 (2012).

[64] E. S. Shuman, J. F. Barry, and D. DeMille, "Laser cooling of a diatomic molecule," *Nature* **467**, 820 (2010).

[65] J. F. Barry, E. S. Shuman, E. B. Norrgard, and D. DeMille, "Laser Radiation Pressure Slowing of a Molecular Beam," *Phys. Rev. Lett.* **108**, 103002 (2012).

[66] J. H. V. Nguyen, C. R. Viteri, E. G. Hohenstein, C. D. Sherrill, K. R. Brown, and B. Odom, "Challenges of laser-cooling molecular ions," *New J. Phys.* **13**, 063023 (2011).

[67] J. H. V. Nguyen and B. Odom, "Prospects for Doppler cooling of three-electronic-level molecules," *Phys. Rev. A* **83**, 053404 (2011).

[68] J. C. J. Koelemeij, B. Roth, A. Wicht, I. Ernsting, and S. Schiller, "Vibrational Spectroscopy of HD^+ with 2-ppb Accuracy," *Phys. Rev. Lett.* **98**, 173002 (2007).

[69] T. Schneider, B. Roth, H. Duncker, I. Ernsting, and S. Schiller, "All-optical preparation of molecular ions in the rovibrational ground state," *Nat. Phys.* **6**, 275 (2010).

[70] U. Bressel, A. Borodin, J. Shen, M. Hansen, I. Ernsting, and S. Schiller, "Manipulation of Individual Hyperfine States in Cold Trapped Molecular Ions and Application to HD^+ Frequency Metrology," *Phys. Rev. Lett.* **108**, 183003 (2012).

[71] P. F. Staanum, K. Højbjerre, P. S. Skyt, A. K. Hansen, and M. Drewsen, "Rotational laser cooling of vibrationally and translationally cold molecular ions," *Nature Physics* **6**, 271 (2010).

[72] X. Tong, A. H. Winney, and S. Willitsch, "Sympathetic Cooling of Molecular Ions in Selected Rotational and Vibrational States Produced by Threshold Photoionization," *Phys. Rev. Lett.* **105**, 143001 (2010).

[73] X. Tong, D. Wild, and S. Willitsch, "Collisional and radiative effects in the state-selective preparation of translationally cold molecular ions in ion traps," *Phys. Rev. A* **83**, 023415 (2011).

[74] E. R. Meyer and J. L. Bohn, "Prospects for an electron electric-dipole moment search in metastable ThO and ThF^+," *Phys. Rev. A* **78**, 010502 (2008).

[75] D. Smith, "The ion chemistry of interstellar clouds," *Chem. Rev.* **92**, 1473 (1992).

[76] B. Roth, P. Blythe, H. Daerr, L. Patacchini, and S. Schiller, "Production of ultracold diatomic and triatomic molecular ions of spectroscopic and astrophysical interest," *J. Phys. B: At., Mol. Opt. Phys.* **39**, S1241 (2006).

[77] V. S. Reddy, S. Ghanta, and S. Mahapatra, "First Principles Quantum Dynamical Investigation Provides Evidence for the Role of Polycyclic Aromatic Hydrocarbon Radical Cations in Interstellar Physics," *Phys. Rev. Lett.* **104**, 111102 (2010).

[78] D. Gerlich, E. Herbst, and E. Roueff, "H^{3+} +HD $\leftrightarrow$ H_2D^+ + H_2: low-temperature laboratory measurements and interstellar implications," *Planetary and Space Science* **50**, 1275 (2002).

[79] P. F. Staanum, K. Højbjerre, R. Wester, and M. Drewsen, "Probing Isotope Effects in Chemical Reactions Using Single Ions," *Phys. Rev. Lett.* **100**, 243003 (2008).

[80] K. Mølhave and M. Drewsen, "Formation of translationally cold MgH^+ and MgD^+ molecules in an ion trap," *Phys. Rev. A* **62**, 011401 (2000).

[81] T. Baba and I. Waki, "Chemical reaction of sympathetically laser-cooled molecular ions," *J. Chem. Phys.* **116**, 1858 (2002).

[82] B. Roth, D. Offenberg, C. B. Zhang, and S. Schiller, "Chemical reactions between cold trapped Ba^+ ions and neutral molecules in the gas phase," *Phys. Rev. A* **78**, 042709 (2008).

[83] L. R. Churchill, M. V. DePalatis, and M. S. Chapman, "Charge exchange and chemical reactions with trapped Th^{3+}," *Phys. Rev. A* **83**, 012710 (2011).

[84] N. Kimura, K. Okada, T. Takayanagi, M. Wada, S. Ohtani, and H. A. Schuessler, "Sympathetic crystallization of CaH^+ produced by a laser-induced reaction," *Phys. Rev. A* **83**, 033422 (2011).

[85] A. K. Hansen, M. A. Sørensen, P. F. Staanum, and M. Drewsen, "Single-Ion Recycling Reactions," *Angew. Chem.* **124**, 8084–8086 (2012).

[86] S. Willitsch, M. T. Bell, A. D. Gingell, S. R. Procter, and T. P. Softley, "Cold Reactive Collisions between Laser-Cooled Ions and Velocity-Selected Neutral Molecules," *Phys. Rev. Lett.* **100**, 043203 (2008).

[87] A. T. Grier, M. Cetina, F. Oručević, and V. Vuletić, "Observation of Cold Collisions between Trapped Ions and Trapped Atoms," *Phys. Rev. Lett.* **102**, 223201 (2009).

[88] F. H. J. Hall, M. Aymar, N. Bouloufa-Maafa, O. Dulieu, and S. Willitsch, "Light-Assisted Ion-Neutral Reactive Processes in the Cold Regime: Radiative Molecule Formation versus Charge Exchange," *Phys. Rev. Lett.* **107**, 243202 (2011).

[89] W. G. Rellergert, S. T. Sullivan, S. Kotochigova, A. Petrov, K. Chen, S. J. Schowalter, and E. R. Hudson, "Measurement of a Large Chemical Reaction Rate between Ultracold Closed-Shell ^{40}Ca Atoms and Open-Shell $^{174}Yb^+$ Ions Held in a Hybrid Atom-Ion Trap," *Phys. Rev. Lett.* **107**, 243201 (2011).

[90] S. Schmid, A. Härter, and J. H. Denschlag, "Dynamics of a Cold Trapped Ion in a Bose-Einstein Condensate," *Phys. Rev. Lett.* **105**, 133202 (2010).

[91] C. Zipkes, S. Palzer, C. Sias, and M. Kohl, "A trapped single ion inside a Bose-Einstein condensate," *Nature* **464**, 388–391 (2010).

[92] K. Chen, S. J. Schowalter, S. Kotochigova, A. Petrov, W. G. Rellergert, S. T. Sullivan, and E. R. Hudson, "Molecular-ion trap-depletion spectroscopy of $BaCl^+$," *Phys. Rev. A* **83**, 030501 (2011).

[93] E. R. Hudson, "Method for producing ultracold molecular ions," *Phys. Rev. A* **79**, 032716 (2009).

[94] W. G. Rellergert, S. T. Sullivan, S. J. Schowalter, S. Kotochigova, K. Chen, and E. R. Hudson, "Evidence for sympathetic vibrational cooling of translationally cold molecules," *Nature* **495**, 490 (2013).

[95] D. I. Schuster, L. S. Bishop, I. L. Chuang, D. DeMille, and R. J. Schoelkopf, "Cavity QED in a molecular ion trap," *Phys. Rev. A* **83**, 012311 (2011).

[96] W. Paul, "Electromagnetic traps for charged and neutral particles," *Rev. Mod. Phys.* **62**, 531 (1990).

[97] H. Dehmelt, "Experiments with an isolated subatomic particle at rest," *Rev. Mod. Phys.* **62**, 525 (1990).

[98] M. A. Levine, R. E. Marrs, J. R. Henderson, D. A. Knapp, and M. B. Schneider, "The Electron Beam Ion Trap: A New Instrument for Atomic Physics Measurements," *Phys. Scr.* **1988**, 157 (1988).

[99] K. H. Kingdon, "A Method for the Neutralization of Electron Space Charge by Positive Ionization at Very Low Gas Pressures," *Phys. Rev.* **21**, 408 (1923).

[100] R. Blümel, "Dynamic Kingdon trap," *Phys. Rev. A* **51**, R30 (1995).

[101] P. Beiersdorfer, "A 'brief' history of spectroscopy on EBIT," *Can. J. Phys.* **86**, 1 (2008).

[102] M. H. Prior, "Radiative decay rates of metastable Ar III and Cu II ions," *Phys. Rev. A* **30**, 3051 (1984).

[103] P. K. Ghosh, *Ion Traps*The International Series of Monographs on Physics (Oxford University Press, Oxford, 1995).

[104] D. Leibfried, R. Blatt, C. Monroe, and D. Wineland, "Quantum dynamics of single trapped ions," *Rev. Mod. Phys.* **75**, 281 (2003).

[105] G. B. Arfken and H. J. Weber, *Mathematical Methods for Physicists*, 6 ed. (Elsevier Academic Press, 2005).

[106] T. M. Hoang, C. S. Gerving, B. J. Land, M. Anquez, C. D. Hamley, and M. S. Chapman, Report No. 1209.4363, 2012 (unpublished).

[107] National Institute of Standards and Technology, "Digital Library of Mathematical Functions," 2011.

[108] M. Abramowitz and I. A. Stegun, editors, *Handbook of Mathematical Functions With Formulas, Graphs, And Mathematical Tables*, 10 ed. (U.S. Department of Commerce, 1964).

[109] N. Konenkov, M. Sudakov, and D. Douglas, "Matrix methods for the calculation of stability diagrams in quadrupole mass spectrometry," *J. Am. Soc. Mass Spectrom.* **13**, 597 (2002).

[110] L. R. Churchill, *Trapping Triply Ionized Thorium Isotopes*, PhD thesis Georgia Institute of Technology 2010.

[111] K. Blaum, "High-accuracy mass spectrometry with stored ions," *Phys. Rep.* **425**, 1 (2006).

[112] F. G. Major and H. G. Dehmelt, "Exchange-Collision Technique for the rf Spectroscopy of Stored Ions," *Phys. Rev.* **170**, 91 (1968).

[113] R. Grimm, M. Weidemüller, and Y. B. Ovchinnikov, "Optical Dipole Traps for Neutral Atoms,", in *Advances In Atomic, Molecular, and Optical Physics*, edited by Benjamin Bederson and Herbert Walther volume 42 pp. 95–170 Academic Press 2000.

[114] S. Amoruso, R. Bruzzese, N. Spinelli, and R. Velotta, "Characterization of laser-ablation plasmas," *Journal of Physics B: Atomic, Molecular and Optical Physics* **32**, R131 (1999).

[115] M. Drewsen and A. Brøner, "Harmonic linear Paul trap: Stability diagram and effective potentials," *Phys. Rev. A* **62**, 045401 (2000).

[116] Scientific Instrument Services, Inc., "SIMION 8.0," 2006.

[117] T. Hänsch and A. Schawlow, "Cooling of gases by laser radiation," *Opt. Commun.* **13**, 68 (1975).

[118] D. J. Wineland and H. Dehmelt, "Proposed 10^{14} $\Delta\nu/\nu$ laser fluorescence spectroscopy on Tl^+ mono-ion oscillator," *Bull. Am. Phys. Soc.* **20**, 637 (1975).

[119] L. Ballentine, *Quantum Mechanics: A Modern Development* (World Scientific, Singapore, 2006).

[120] H. J. Metcalf and P. van der Straten, *Laser Cooling and Trapping*Graduate Texts in Contemporary Physics (Springer-Verlag, New York, 1999).

[121] K. Mølmer, Y. Castin, and J. Dalibard, "Monte Carlo wave-function method in quantum optics," *J. Opt. Soc. Am. B* **10**, 524–538 (1993).

[122] V. Gorini, A. Kossakowski, and E. C. G. Sudarshan, "Completely positive dynamical semigroups of N-level systems," *J. Math. Phys.* **17**, 821 (1976).

[123] G. Lindblad, "On the generators of quantum dynamical semigroups," *Commun. Math. Phys.* **48**, 119 (1976).

[124] D. Budker, D. F. Kimball, and D. P. DeMille, *Atomic Physics: An Exploration Through Problems and Solutions* (Oxford University Press, New York, 2004).

[125] B. Sanchez and T. Brandes, "Matrix perturbation theory for driven three-level systems with damping," *Annalen der Physik* **13**, 569–594 (2004).

[126] R. Loudon, *The Quantum Theory of Light*, Third ed. (Oxford University Press, New York, 2007).

[127] E. Peik, J. Abel, T. Becker, J. von Zanthier, and H. Walther, "Sideband cooling of ions in radio-frequency traps," *Phys. Rev. A* **60**, 439–449 (1999).

[128] D. Kielpinski, M. Cetina, J. A. Cox, and F. X. Kärtner, "Laser cooling of trapped ytterbium ions with an ultraviolet diode laser," *Opt. Lett.* **31**, 757 (2006).

[129] M. Herrmann, V. Batteiger, S. Knünz, G. Saathoff, T. Udem, and T. W. Hänsch, "Frequency Metrology on Single Trapped Ions in the Weak Binding Limit: The $3s_{1/2} - 3p_{3/2}$ Transition in $^{24}Mg^{+}$," *Phys. Rev. Lett.* **102**, 013006 (2009).

[130] I. S. Vogelius, L. B. Madsen, and M. Drewsen, "Blackbody-Radiation–Assisted Laser Cooling of Molecular Ions," *Phys. Rev. Lett.* **89**, 173003 (2002).

[131] D. J. Berkeland, J. D. Miller, J. C. Bergquist, W. M. Itano, and D. J. Wineland, "Laser-Cooled Mercury Ion Frequency Standard," *Phys. Rev. Lett.* **80**, 2089–2092 (1998).

[132] P. B. Antohi, D. Schuster, G. M. Akselrod, J. Labaziewicz, Y. Ge, Z. Lin, W. S. Bakr, and I. L. Chuang, "Cryogenic ion trapping systems with surface-electrode traps," *Rev. Sci. Instrum.* **80**, 013103 (2009).

[133] J. C. J. Koelemeij, B. Roth, and S. Schiller, "Blackbody thermometry with cold molecular ions and application to ion-based frequency standards," *Phys. Rev. A* **76**, 023413 (2007).

[134] H. Thomas, G. E. Morfill, V. Demmel, J. Goree, B. Feuerbacher, and D. Möhlmann, "Plasma Crystal: Coulomb Crystallization in a Dusty Plasma," *Physical Review Letters* **73**, 652 (1994).

[135] A. Dantan, M. Albert, J. P. Marler, P. F. Herskind, and M. Drewsen, "Large ion Coulomb crystals: A near-ideal medium for coupling optical cavity modes to matter," *Phys. Rev. A* **80**, 041802 (2009).

[136] M. A. van Eijkelenborg, M. E. M. Storkey, D. M. Segal, and R. C. Thompson, "Sympathetic cooling and detection of molecular ions in a Penning trap," *Phys. Rev. A* **60**, 3903 (1999).

[137] J. P. Hansen, "Statistical Mechanics of Dense Ionized Matter. I. Equilibrium Properties of the Classical One-Component Plasma," *Phys. Rev. A* **8**, 3096 (1973).

[138] E. L. Pollock and J. P. Hansen, "Statistical Mechanics of Dense Ionized Matter. II. Equilibrium Properties and Melting Transition of the Crystallized One-Component Plasma," *Phys. Rev. A* **8**, 3110 (1973).

[139] L. Hornekær and M. Drewsen, "Formation process of large ion Coulomb crystals in linear Paul traps," *Phys. Rev. A* **66**, 013412 (2002).

[140] S. G. Brush, H. L. Sahlin, and E. Teller, "Monte Carlo Study of a One-Component Plasma. I," *The Journal of Chemical Physics* **45**, 2102 (1966).

[141] D. J. Larson, J. C. Bergquist, J. J. Bollinger, W. M. Itano, and D. J. Wineland, "Sympathetic cooling of trapped ions: A laser-cooled two-species nonneutral ion plasma," *Phys. Rev. Lett.* **57**, 70 (1986).

[142] D. Kielpinski, B. E. King, C. J. Myatt, C. A. Sackett, Q. A. Turchette, W. M. Itano, C. Monroe, D. J. Wineland, and W. H. Zurek, "Sympathetic cooling of trapped ions for quantum logic," *Phys. Rev. A* **61**, 032310 (2000).

[143] M. D. Barrett, B. DeMarco, T. Schaetz, V. Meyer, D. Leibfried, J. Britton, J. Chiaverini, W. M. Itano, B. Jelenković, J. D. Jost, C. Langer, T. Rosenband, and D. J. Wineland, "Sympathetic cooling of $^{9}Be^{+}$ and $^{24}Mg^{+}$ for quantum logic," *Phys. Rev. A* **68**, 042302 (2003).

[144] P. O. Schmidt, T. Rosenband, C. Langer, W. M. Itano, J. C. Bergquist, and D. J. Wineland, "Spectroscopy Using Quantum Logic," *Science* **309**, 749 (2005).

[145] C. B. Zhang, D. Offenberg, B. Roth, M. A. Wilson, and S. Schiller, "Molecular-dynamics simulations of cold single-species and multispecies ion ensembles in a linear Paul trap," *Phys. Rev. A* **76**, 012719 (2007).

[146] C. Zhang, *Production and sympathetic cooling of complex molecular ions*, PhD Heinrich-Heine-University Düsseldorf Düsseldorf, Germany 2008.

[147] A. Troisi, V. Wong, and M. A. Ratner, "An agent-based approach for modeling molecular self-organization," *Proc. Natl. Acad. Sci. U.S.A.* **102**, 255 (2005).

[148] L. Perera and M. L. Berkowitz, "Many-body effects in molecular dynamics simulations of $Na^{+}(H_2O)_n$ and $Cl^{-}(H_2O)_n$ clusters," *J. Chem. Phys.* **95**, 1954 (1991).

[149] M. Levitt and A. Warshel, "Computer simulation of protein folding," *Nature* **253**, 694 (1975).

[150] M. P. Allen and D. J. Tildesley, *Computer simulation of liquids* (Oxford University Press, Oxford, 1987).

[151] R. Averback and T. D. de La Rubia, "Displacement damage in irradiated metals and semiconductors," *Solid State Physics* **51**, 281 (1997).

[152] B. J. Alder and T. E. Wainwright, "Phase transition for a hard sphere system," *J. Chem. Phys.* **27**, 1208 (1957).

[153] B. J. Alder and T. E. Wainwright, "Studies in molecular dynamics. I. General method," *J. Chem. Phys.* **31**, 459 (1959).

[154] A. Rahman and F. H. Stillinger, "Molecular dynamics study of liquid water," *J. Chem. Phys.* **55**, 3336 (1971).

[155] Q. A. Turchette, Kielpinski, B. E. King, D. Leibfried, D. M. Meekhof, C. J. Myatt, M. A. Rowe, C. A. Sackett, C. S. Wood, W. M. Itano, C. Monroe, and D. J. Wineland, "Heating of trapped ions from the quantum ground state," *Phys. Rev. A* **61**, 063418 (2000).

[156] V. L. Ryjkov, X. Zhao, and H. A. Schuessler, "Simulations of the rf heating rates in a linear quadrupole ion trap," *Phys. Rev. A* **71**, 033414 (2005).

[157] P. Hut and J. Makino, "Moving Stars Around,", in *The Art of Computational Science* volume 2 2003.

[158] T. Matthey, T. Cickovski, S. Hampton, A. Ko, Q. Ma, M. Nyerges, T. Raeder, T. Slabach, and J. A. Izaguirre, "ProtoMol, an object-oriented framework for prototyping novel algorithms for molecular dynamics," *ACM Trans. Math. Softw.* **30**, 237–265 (2004).

[159] C. K. Birdsall and A. B. Langdon, *Plasma Physics via Computer Simulations* (McGraw-Hill, 1985).

[160] R. D. Skeel, *The Graduate Student's Guide to Numerical Analysis '98* (Springer, 1999), chap. Integration Schemes for Molecular Dynamics and Related Applications, pp. 119–176.

[161] R. Rafac, J. P. Schiffer, J. S. Hangst, D. H. Dubin, and D. J. Wales, "Stable configurations of confined cold ionic systems," *Proc. Natl. Acad. Sci. USA* **88**, 483 (1991).

[162] D. H. E. Dubin, "Minimum energy state of the one-dimensional Coulomb chain," *Phys. Rev. E* **55**, 4017 (1997).

[163] S. G. Johnson, "The NLopt nonlinear-optimization package," 2008.

[164] T. Darden, D. York, and L. Pedersen, "Particle mesh Ewald: An $N\log(N)$ method for Ewald sums in large systems," *J. Chem. Phys.* **98**, 10089 (1993).

[165] A. Brandt and A. Lubrecht, "Multilevel matrix multiplication and fast solution of integral equations," *J. Comput. Phys.* **90**, 348 (1990).

[166] A. Y. Toukmaji and J. A. Board Jr., "Ewald summation techniques in perspective: a survey," *Comput. Phys. Commun.* **95**, 73 (1996).

[167] M. Drewsen, T. Matthey, A. Mortensen, and J. P. Hansen, Report No. 1202.2544, 2012 (unpublished).

[168] P. Horak, A. Dantan, and M. Drewsen, "Optically induced structural phase transitions in ion Coulomb crystals," *Phys. Rev. A* **86**, 043435 (2012).

[169] D. J. Berkeland, J. D. Miller, J. C. Bergquist, W. M. Itano, and D. J. Wineland, "Minimization of ion micromotion in a Paul trap," *J. Appl. Phys.* **83**, 5025 (1998).

[170] D. J. Berkeland, "Linear Paul trap for strontium ions," *Rev. Sci. Instrum.* **73**, 2856 (2002).

[171] J. C. Owens, "Optical Refractive Index of Air: Dependence on Pressure, Temperature and Composition," *Appl. Opt.* **6**, 51 (1967).

[172] J. A. Stone and J. H. Zimmerman, "Index of Refraction of Air,", Online 2011.

[173] A. Franzen, "ComponentLibrary: a vector graphics library for illustrations of optics experiments,", Online 2006.

[174] F. Rohde, M. Almendros, C. Schuck, J. Huwer, M. Hennrich, and J. Eschner, "A diode laser stabilization scheme for $^{40}Ca^{+}$ single-ion spectroscopy," *J. Phys. B: At., Mol. Opt. Phys.* **43**, 115401 (2010).

[175] J. C. Bergquist, D. J. Wineland, W. M. Itano, H. Hemmati, H. U. Daniel, and G. Leuchs, "Energy and Radiative Lifetime of the $5d^9 6s^2 D_{5/2}$ State in Hg II by Doppler-Free Two-Photon Laser Spectroscopy," *Phys. Rev. Lett.* **55**, 1567 (1985).

[176] J. Desesquelles, M. Dufay, and M. Poulizac, "Lifetime measurement of molecular states with an accelerated ion beam," *Phys. Lett. A* **27**, 96 (1968).

[177] W. Ansbacher, Y. Li, and E. H. Pinnington, "Precision lifetime measurement for the 3p levels of Mg II using frequency-doubled laser radiation to excite a fast ion beam," *Phys. Lett. A* **139**, 165 (1989).

[178] C. Gerz, T. Hilberath, and G. Werth, "Lifetime of the $4D_{3/2}$ and $4D_{5/2}$ metastable states in Sr II," *Z. Phys. D* **5**, 97 (1987).

[179] M. Knoop, M. Vedel, and F. Vedel, "Lifetime, collisional-quenching, and j-mixing measurements of the metastable 3D levels of Ca^{+}," *Phys. Rev. A* **52**, 3763–3769 (1995).

[180] P. A. Barton, C. J. S. Donald, D. M. Lucas, D. A. Stevens, A. M. Steane, and D. N. Stacey, "Measurement of the lifetime of the $3d^2 D_{5/2}$ state in $^{40}Ca^{+}$," *Phys. Rev. A* **62**, 032503 (2000).

[181] D. L. Moehring, B. B. Blinov, D. W. Gidley, R. N. Kohn, M. J. Madsen, T. D. Sanderson, R. S. Vallery, and C. Monroe, "Precision lifetime measurements of a single trapped ion with ultrafast laser pulses," *Phys. Rev. A* **73**, 023413 (2006).

[182] S. Olmschenk, D. Hayes, D. N. Matsukevich, P. Maunz, D. L. Moehring, K. C. Younge, and C. Monroe, "Measurement of the lifetime of the $6p\,^2P^o_{1/2}$ level of Yb^{+}," *Phys. Rev. A* **80**, 022502 (2009).

[183] A. V. Steele, *Barium ion cavity QED and triply ionized thorium ion trapping*, PhD thesis Georgia Institute of Technology 2008.

[184] U. I. Safronova, W. R. Johnson, and M. S. Safronova, "Excitation energies, polarizabilities, multipole transition rates, and lifetimes in Th IV," *Phys. Rev. A* **74**, 042511 (2006).

[185] N. Yu, W. Nagourney, and H. Dehmelt, "Radiative Lifetime Measurement of the Ba^{+} Metastable $D_{3/2}$ State," *Phys. Rev. Lett.* **78**, 4898–4901 (1997).

[186] V. Letchumanan, M. A. Wilson, P. Gill, and A. G. Sinclair, "Lifetime measurement of the metastable $4d^2 D_{5/2}$state in $^{88}Sr^{+}$ using a single trapped ion," *Phys. Rev. A* **72**, 012509 (2005).

[187] S. Willitsch, M. T. Bell, A. D. Gingell, and T. P. Softley, "Chemical applications of laser- and sympathetically-cooled ions in ion traps," *Phys. Chem. Chem. Phys.* **10**, 7200 (2008).

[188] J. D. Weinstein, R. deCarvalho, T. Guillet, B. Friedrich, and J. M. Doyle, "Magnetic trapping of calcium monohydride molecules at millikelvin temperatures," *Nature* **395**, 148 (1998).

[189] H. L. Bethlem, G. Berden, F. M. H. Crompvoets, R. T. Jongma, A. J. A. van Roij, and G. Meijer, "Electrostatic trapping of ammonia molecules," *Nature* **406**, 491 (2000).

[190] M. T. Hummon, M. Yeo, B. K. Stuhl, A. L. Collopy, Y. Xia, and J. Ye, "2D Magneto-Optical Trapping of Diatomic Molecules," *Phys. Rev. Lett.* **110**, 143001 (2013).

[191] K. Okada, T. Suganuma, T. Furukawa, T. Takayanagi, M. Wada, and H. A. Schuessler, "Cold ion–polar-molecule reactions studied with a combined Stark-velocity-filter–ion-trap apparatus," *Phys. Rev. A* **87**, 043427 (2013).

[192] S. J. Schowalter, K. Chen, W. G. Rellergert, S. T. Sullivan, and E. R. Hudson, "An integrated ion trap and time-of-flight mass spectrometer for chemical and photo-reaction dynamics studies," *Rev. Sci. Instrum.* **83**, 043103 (2012).

[193] P. L. Houston, *Chemical Kinetics and Reaction Dynamics* (McGraw-Hill, New York, 2001).

[194] G. Gioumousis and D. P. Stevenson, "Reactions of Gaseous Molecule Ions with Gaseous Molecules. V. Theory," *J. Chem. Phys.* **29**, 294 (1958).

[195] P. Langevin, *Ann. Chim. Phys.* **28**, 433 (1903).

[196] J. Troe, "Statistical adiabatic channel model of ion-neutral dipole capture rate constants," *Chem. Phys. Lett.* **122**, 425 (1985).

[197] T. Su and M. T. Bowers, "Theory of ion-polar molecule collisions. Comparison with experimental charge transfer reactions of rare gas ions to geometric isomers of difluorobenzene and dichloroethylene," *J. Chem. Phys.* **58**, 3027 (1973).

[198] T. Su, E. C. F. Su, and M. T. Bowers, "Ion-polar molecule collisions. Conservation of angular momentum in the average dipole orientation theory. The AADO theory," *J. Chem. Phys.* **69**, 2243 (1978).

[199] W. J. Chesnavich, T. Su, and M. T. Bowers, "Collisions in a noncentral field: A variational and trajectory investigation of ion-dipole capture," *The Journal of Chemical Physics* **72**, 2641 (1980).

[200] D. Clary, "Calculations of rate constants for ion-molecule reactions using a combined capture and centrifugal sudden approximation," *Mol. Phys.* **54**, 605 (1985).

[201] D. Clary, D. Smith, and N. Adams, "Temperature dependence of rate coefficients for reactions of ions with dipolar molecules," *Chem. Phys. Lett.* **119**, 320 (1985).

[202] T. Baba and I. Waki, "Spectral shape of in situ mass spectra of sympathetically cooled molecular ions," *J. Appl. Phys.* **92**, 4109 (2002).

[203] M. Drewsen, A. Mortensen, R. Martinussen, P. Staanum, and J. L. Sørensen, "Nondestructive Identification of Cold and Extremely Localized Single Molecular Ions," *Phys. Rev. Lett.* **93**, 243201 (2004).

[204] B. Roth, P. Blythe, and S. Schiller, "Motional resonance coupling in cold multispecies Coulomb crystals," *Phys. Rev. A* **75**, 023402 (2007).

[205] K. Sheridan and M. Keller, "Weighing of trapped ion crystals and its applications," *New J. Phys.* **13**, 123002 (2011).

[206] J. E. Goeders, C. R. Clark, G. Vittorini, K. Wright, C. R. Viteri, and K. R. Brown, "Identifying Single Molecular Ions by Resolved Sideband Measurements," *J. Phys. Chem. A* (2013).

[207] R. E. March, "An Introduction to Quadrupole Ion Trap Mass Spectrometry," *J. Mass Spectrom.* **32**, 351 (1997).

[208] E. Murad, "The reactions of Ba^+ ions with O_2 and H_2O," *J. Chem. Phys.* **77**, 2057 (1982).

[209] D. R. Lide, *CRC Handbook of Chemistry and Physics*, 88 ed. (CRC Press, Boca Raton, FL, 2007).

[210] Agilent Technologies, *UHV-24/UHV-24p Ionization Gauge Instruction Manual* , Rev. E ed. 2004.

[211] S. G. Lias, *NIST Chemistry WebBook, NIST Standard Reference Database Number 69* (National Institute of Standards and Technology, Gaithersburg MD, 20899, 2011), chap. Ionization Energy Evaluation.

[212] H. Karlsson and U. Litzén, "Revised Ba I and Ba II Wavelengths and Energy Levels Derived by Fourier Transform Spectroscopy," *Phys. Scr.* **60**, 321 (1999).

[213] H. Tachikawa, "The ionization dynamics of SF6: a full dimensional direct ab initio dynamics study," *J. Phys. B: At., Mol. Opt. Phys.* **33**, 1725 (2000).

[214] Z. Karpas and Z. Berant, "Effect of drift gas on mobility of ions," *The Journal of Physical Chemistry* **93**, 3021 (1989).

[215] T. N. Olney, N. Cann, G. Cooper, and C. Brion, "Absolute scale determination for photoabsorption spectra and the calculation of molecular properties using dipole sum-rules," *Chem. Phys.* **223**, 59 (1997).

[216] G. Maroulis, C. Makris, U. Hohm, and D. Goebel, "Electrooptical Properties and Molecular Polarization of Iodine, I_2," *J. Phys. Chem. A* **101**, 953 (1997).

[217] G. Maroulis and C. Makris, "On the electric properties of Br_2," *Mol. Phys.* **91**, 333 (1997).

[218] R. D. Johnson, ed., "NIST Computational Chemistry Comparison and Benchmark Database," 2011, Release 15b.

[219] K. Zimmermann, M. Okhapkin, O. Herrera-Sancho, and E. Peik, "Laser ablation loading of a radiofrequency ion trap," *Appl. Phys. B: Lasers Opt.* **107**, 883 (2012).

[220] T. Gudjons, B. Hilbert, P. Seibert, and G. Werth, "Precise lifetime determination of the metastable $3d^2D_{5/2}$ level in Ca^+ by "electron shelving"," *Europhys. Lett.* **33**, 595 (1996).

[221] M. Knoop, C. Champenois, G. Hagel, M. Houssin, C. Lisowski, M. Vedel, and F. Vedel, "Metastable level lifetimes from electron-shelving measurements with ion clouds and single ions," *Eur. Phys. J. D* **29**, 163 (2004).

[222] C. Chin, R. Grimm, P. Julienne, and E. Tiesinga, "Feshbach resonances in ultracold gases," *Rev. Mod. Phys.* **82**, 1225 (2010).

[223] H. S. Gutowsky, "Silicon Tetrafluoride,", in *Inorganic Syntheses*, edited by C. J. Hoffman volume 4 pp. 145–6 McGraw-Hill 1953.

[224] H. L. Bethlem, A. J. A. van Roij, R. T. Jongma, and G. Meijer, "Alternate Gradient Focusing and Deceleration of a Molecular Beam," *Phys. Rev. Lett.* **88**, 133003 (2002).

[225] N. Vanhaecke, U. Meier, M. Andrist, B. H. Meier, and F. Merkt, "Multistage Zeeman deceleration of hydrogen atoms," *Phys. Rev. A* **75**, 031402 (2007).

[226] E. Narevicius and M. G. Raizen, "Toward Cold Chemistry with Magnetically Decelerated Supersonic Beams," *Chem. Rev.* **112**, 4879 (2012).

[227] S. Merz, N. Vanhaecke, W. Jäger, M. Schnell, and G. Meijer, "Decelerating molecules with microwave fields," *Phys. Rev. A* **85**, 063411 (2012).

[228] J. J. Curry, "Compilation of Wavelengths, Energy Levels, and Transition Probabilities for Ba I and Ba II," *J. Phys. Chem. Ref. Data* **33**, 725 (2004).

[229] J. S. Coursey, D. J. Schwab, J. J. Tsai, and R. A. Dragoset, "Atomic Weights and Isotopic Compositions," 2010.

[230] National Nuclear Data Center, "NuDat 2 database,," 2011.

[231] K. Wendt, S. A. Ahmad, F. Buchinger, A. C. Mueller, R. Neugart, and E.-W. Otten, "Relativistic J-dependence of the isotope shift in the $6s$-$6p$ doublet of Ba II," *Z. Phys. A* **318**, 125 (1984).

[232] Stanford Research Systems Sunnyvale, CA, *Model SR560 Low-Noise Preamplifier* , 2.9 ed. 2011.

[233] Panasonic, "DVD-R Authoring vs. General Media: What's the Difference?," 2004.

[234] B. DeMarco, *Quantum Behavior of an Atomic Fermi Gas*, PhD thesis University of Colorado 2001.

[235] H. Ball, M. W. Lee, S. D. Gensemer, and M. J. Biercuk, "A high-power 626 nm diode laser system for Beryllium ion trapping," *Rev. Sci. Instrum.* **84**, 063107 (2013).

VITA

Michael V. DePalatis was born in Midland, Michigan.